6-9-2010

# Functional Nanomaterials with an Electrochemistry-Based Approach to Sensing and Energy Applications

Jessica Eileen Weber
*University of South Florida*

# Functional Nanomaterials with an Electrochemistry-Based Approach to Sensing and Energy Applications

by

Jessica Eileen Weber

A dissertation submitted in partial fulfillment
of the requirements for the degree of
Doctor of Philosophy
Department of Mechanical Engineering
College of Engineering
University of South Florida

Major Professor: Ashok Kumar, Ph.D.
Rajiv Dubey, Ph.D.
Muhammad Rahman, Ph.D.
Ryan Toomey, Ph.D.
Garrett Matthews, Ph.D.

Date of Approval:
June 9, 2010

Keywords: Biosensor, DNA, Nanocrystalline diamond, Carbon nanotube, Thermoelectric

## DEDICATION

For Cailin. May you reach further and soar higher than I can even dream. For Justin for walking beside me. For my parents and family for supporting my academic adventures.

**ACKNOWLEDGEMENTS**

I would like to extend my deepest thanks to my major professor, Dr. Ashok Kumar, for his guidance and support during my dissertation research. I would also like to thank my committee members, Dr. Rajiv Dubey, Dr. Muhammad Rahman, Dr. Ryan Toomey, and Dr. Garrett Mathews for providing their professional feedback regarding my dissertation and advice on my career path after graduate school. Thank you to Dr. Shyam Mohapatra for serving as the Chair of my doctoral defense.

There are several people who have helped and supported me during my graduate career. A special thank you to Mr. Bernard Batson, who always was available to provide advice and support on any issue throughout grad school. Thank you to Ms. Susan Britten and Ms. Shirley Tervort of the Mechanical Engineering office for all their administrative help. I would like to acknowledge Mr. Graham Yelton of Sandia National Labs for his guidance during my internship and continued support on any topic relating to electrochemistry. Finally, I would like to thank Mr. Humberto Gomez and the rest of my lab-mates for all of their support of my research efforts.

I am thankful for being supported by the NSF IGERT Fellowship and the NSF GK-12 Fellowship during my graduate career. Several grants made my dissertation research possible. This work was financially supported by the following National Science Foundation grants: NIRT #0404137, CREST #0734232, IGERT #0221681 and GK12 #0638709.

**TABLE OF CONTENTS**

## LIST OF TABLES

## LIST OF FIGURES

Functional Nanomaterials with an Electrochemistry-Based Approach to Sensing and Energy Applications

Jessica Eileen Weber

## ABSTRACT

In the past decade, the use of nanotechnology as a tool to develop and fabricate new structures and devices for biological sensing and energy applications has become increasingly widespread. In this work, a systematic study has been performed on one-dimensional nanomaterials, with a focus on the development of miniaturized devices with a "bottom up" approach. First, members of the nano – carbon family are utilized for biosensing applications; in particular, carbon nanotubes as well as nitrogen – doped and boron – doped nanocrystalline diamond (NCD) films. These carbon – based materials possess several unique electrochemical properties over other conductive materials which make them suitable for biosensing applications. Single walled carbon nanotubes were deposited on a glass carbon electrode and modified for the detection of *Salmonella* DNA hybridization. Electrochemical impedance spectroscopy (EIS) was used as the method of detection and a detection limit of $10^{-9}$ M was achieved. Nanocrystalline diamond was grown using a microwave enhanced plasma chemical vapor deposition method. The diamond electrodes were doped with either boron or nitrogen to provide substrates and characterization was performed using scanning electron microscopy, atomic force

microscopy, Raman spectroscopy, Fourier transform infrared spectroscopy, UV-vis spectroscopy, as well as by electrochemical methods. Modified boron – doped NCD was able to detect *Salmonella* DNA hybridization via EIS and fluorescent microscopy. The detection limit for these genosensors was found to be 0.4 μM complementary DNA. Boron – doped and nitrogen – incorporated nanocrystalline diamond also served as functionalized electrodes for lactic acid detection. It was found that the boron – doped electrodes could detect 0.5 mM lactic acid in a phosphate buffer solution.

Second, bismuth antimony nanowires were grown in an anodized alumina template for the fabrication of a thermoelectric cooling device. Bismuth antimony nanowires were chosen due to their high thermoelectric efficiency compared to their bulk material counterpart. The development of a successful anodized template was achieved and EIS was used to diagnose the optimal etch parameters of the barrier oxide layer for nanowire growth. Bismuth antimony nanowires were grown directly on a silicon substrate and a thermoelectric cooling device was fabricated. The nanowires exhibited a thermoelectric efficiency of 0.18 at room temperature.

# CHAPTER 1: INTRODUCTION

Over the past two decades since the discovery of carbon nanotubes[2], one dimensional nanostructures have received growing interest. In this manuscript, the term "one dimensional" shall be used to refer to structures, including nano – rods, belts, tubes, and wires, which have at least one dimension between 1 and 100 nm, with significantly large length to diameter aspect ratios. Due to their unique electrical, thermal, mechanical, and optical properties that vary from their respective bulk counterparts, fundamental understanding of 1D nanostructures is vital for technological progression. The potential application of these structures has a broad impact in the research fields of medical sensing, drug delivery, microelectronics, bioMEMS, communications, energy storage, and computation technology. While Moore's Law continues to push the miniaturization limit of the atomic level, integration of nanowires into electronic devices is still advancing. Furthermore, the "bottom up" synthesis method is a promising technique for addressing such challenges related to nanotechnology production and application. Unlike the traditional photolithography and etching techniques, the bottom up approach involves direct, controlled growth of nanostructures directly onto the substrate. Publications relating to 1D nanostructures has increased dramatically in the past several years. This growth of research has led to the development of new methods for simple production, growth with precise control over structural properties and chemical composition, a growing number of novel 1D materials with unique properties,

improved characterization techniques, as well as a dramatic increase in potential applications relating to biotechnology.

### 1.1. Introduction to Nano – Carbon

Until the discovery of fullerenes in 1985, the science and chemistry of the carbon atom was thought to be well known. Previous to this discovery, carbon was known to form graphite and diamond, as well as amorphous materials like charcoal. Perhaps the most important consequence of the discovery of the fullerene is that it opened the door for matter to be studied at the nanoscale. Six years later, in 1991, another big surprise was found – the carbon nanotube. These two forms of carbon have led to a burst of research in nanomaterials. Today, the nano – carbon family includes many recently discovered "wonder materials", including $C_{60}$ (a.k.a. "buckyballs"), carbon nanotubes, nanocrystalline diamond thin films and most recently, graphene. Depending on the lattice structure of each of these carbon – based materials, different material properties are observed at the nanoscale. Here, we focus on carbon nanotubes and nanocrystalline diamond (Table 1.1.). [3-6]

Table 1.1. Material properties of nano – carbon

| MATERIAL PROPERTY | Single Walled Carbon Nanotube | Single Crystal Diamond |
|---|---|---|
| Density | 2.1 $gcm^{-3}$ | 3.52 $gcm^{-3}$ |
| Young's Modulus | ~1-5TPa | 1050 GPa |

Table 1.1. (Continued)

| | | |
|---|---|---|
| Resistivity | ~$10^{-4}$ Ω-cm | $10^{13}$ - $10^{14}$ Ω-cm |
| Thermal Conductivity | 1750-5800 W/m-K | 2500 W/m-K |

### 1.1.1. Carbon Nanotubes

A single – walled carbon nanotube (SWNT) is based on a two-dimensional graphene sheet and can be characterized by a chiral vector **C**. The chiral vector is defined on the hexagonal lattice as $\mathbf{C} = n\mathbf{a}_1 + m\mathbf{a}_2$, where $\mathbf{a}_1$ and $\mathbf{a}_2$ are unit vectors, and $n$ and $m$ are integers. The chiral angle, θ, is measured relative to the direction defined by $\mathbf{a}_1$ (Figure 1.1). When a graphene sheet is rolled up to form the cylinder, the ends of the chiral vector meet each other and connect two crystallographically equivalent sites[7]. Thus, the length of the chiral vector is equal to the circumference of the nanotube. The values of (n,m), which govern the diameter and the chirality of the tube, will determine whether the carbon nanotube will behave as a metallic or semiconductor material. The chiral vector one of three possible nanotube structures: armchair, zigzag and chiral. All armchair nanotubes are metallic, as well as one-third of all zigzag nanotubes.

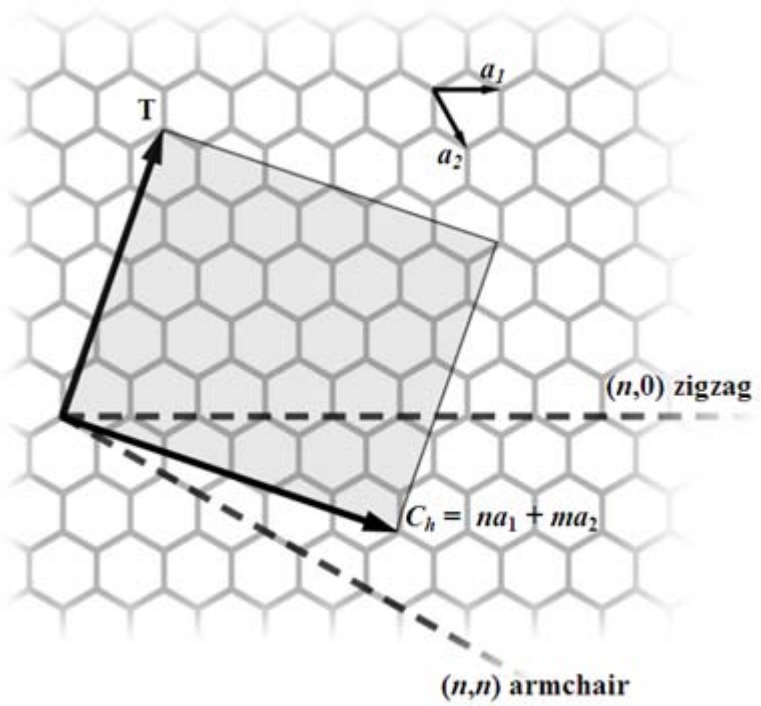


Figure 1.1. The (n,m) nanotube naming scheme can be thought of as a vector (Ch) in an infinite graphene sheet that describes how to 'roll up' the graphene sheet to make the nanotube. T denotes the tube axis, and $a_1$ and $a_2$ are the unit vectors of graphene in real space.

Carbon nanotubes are a unique class of one dimensional nanostructures and their mechanical properties are of considerable interest. In 1991 Beck *et al.*[8] reported that when fullerene molecules were collided against graphite and silicon over a wide range of energies that the events were highly inelastic and non – fragmenting. This same property of resilience becomes magnified with a carbon nanotube. Due to its extremely small structure, direct experimental measurements of mechanical properties of carbon nanotubes such as Young's modulus and tensile strength have been a challenge. Treacy and coworkers[9] performed the first experimental data of the Young's modulus by isolating a carbon nanotube and measuring the amplitude of its intrinsic thermal vibration in a transmission electron microscope. The thermal vibration at the free ends of the

nanotubes was a function of temperature and Young's modulus. Assuming the nanotube behaved as a straight cantilever rod with one end fixed and the other vibrating, an average value of 1.8 TPa for the Young's modulus was obtained.

Carbon nanotubes, in particular, are the quintessential electrode material due to their excellent mechanical strength, high electrical and thermal conductivity. Additionally, their large length to diameter aspect ratio along with a high surface area to weight ratio is an ideal combination for providing surface functionalization of biomolecules. However, due to the lack of solubility of CNTs in many solutions, integration of CNTs in biosensor design remains a difficult challenge. While covalent modification on the nanotube surface was originally used to solve solubility issues, this technique is now used extensively for biological functionalization such as enzyme attachment to the tip of the CNT[10, 11]. For example, treatment of CNTs with sulfuric and nitric acid under sonication will shorten and open the ends of the nanotubes while introducing carboxylic acid functional groups[12]. This technique is not only beneficial for nanotube solubility, but for functional group surface attachment as well. It has been shown previously that proteins will covalently attach to the ends of shortened SWNTs, which behave as molecular wires to allow electrical communication between the underlying electrode and the redox protein[13].

Modification of electrode surfaces with carbon nanotubes has shown to greatly enhance the performance of the sensor for analytes such as lactic acid[14], cinnarizine[15], antibodies[16], and DNA[17]. In particular, carbon nanotube – modified electrodes exhibit

superior electrochemical properties, such as a wide working potential window, and also demonstrate catalytic activity towards many chemical reactions.

### 1.1.2. Nanocrystalline Diamond

Diamond follows the face – centered cubic bravais lattice, with eight carbon atoms per unit cell. The carbon atoms are covalently bonded to the four nearest neighboring atoms. With a lattice constant ($a_0$) of 3.567 Å, a bond length of 1.54 Å, and an atomic density of $1.7 \times 10^{23}$ $cm^3$, diamond exhibits several exceptional material properties.

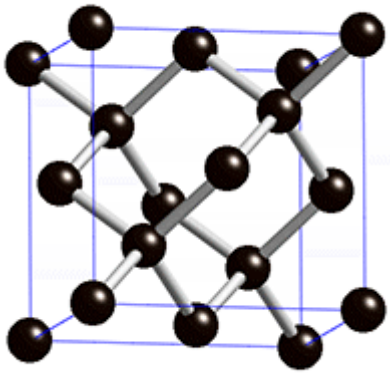

Figure 1.2. Unit cell of the diamond cubic structure

Boron – doped microcrystalline and nanocrystalline diamond thin films in particular display a number of electrochemical properties which distinguish them from other carbon-based electrodes, such as a low background current, a wide working potential in both aqueous and non-aqueous media[18], and good responsiveness for several redox analytes[19]. The importance of the wide working window in diamond is that

electrochemical reactions may be analyzed over a much larger potential window than for other electrode materials in the carbon family.

### 1.2. Introduction to Nanomaterials for Thermoelectrics

Due to their small size and high surface area, an in – depth understanding of thermal stability and conductivity in nanowires is vital before these structures can be implemented into microelectronic or thermoelectronic devices. It is known that thermal conduction is expected to be reduced with decreasing nanowire diameters. The decrease in thermal conductivity of small diameter nanowires is a distinguished advantage for thermoelectronic applications. Nanowires that possess both poor thermal conductivity and high electrical conductivity are candidates for devices which require highly effective thermal management. Materials are often evaluated by their dimensionless thermoelectric figure of merit, *ZT*, given by:

$$ZT = \frac{\sigma S^2 T}{\kappa} \tag{1}$$

where $\sigma$ is the electric conductivity, $S$ is the Seeback coefficient, T is the absolute temperature, and $\kappa$ is the thermal conductivity. Dresselhaus and coworkers[20] developed a theoretical model for Bi nanowires which predicted that under careful selection of nanowire diameter and carrier concentration the thermoelectric efficiency is drastically enhanced. The *ZT* value increases due to quantum effects as well as phonon scattering at the boundaries. Based on the semiclassical transport model and the band structure model, the *ZT* of a properly doped Bi nanowire oriented along the trigonal crystallographic direction, is expected to reach a value $\geq$ 1 at 77 K as wire diameter decreases below 15

nm[21]. However, it is difficult to study the thermoelectronic properties of Bi nanowires due to the difficulty in producing uniform nanowires at such small diameters and they are usually randomly dispersed either in solution or on a substrate. Furthermore, it has been known that the *ZT* values of both bismuth telluride and bismuth antimony alloys are much higher than bismuth alone[22]. Of particular interest is the $Bi_{(1-x)}Sb_{(x)}$ alloy, which in bulk form displays a diversity of electronic behavior[23]. Theoretical predictions indicate that the figure of merit is increased for both *n*-type and *p*-type $Bi_{(1-x)}Sb_{(x)}$ nanowires at higher diameters at 77 K[24] (Figure 1.3.). Table 1.2. summarizes the thermoelectric figure of merit for several material alloys of interest at both the bulk and nanoscale.

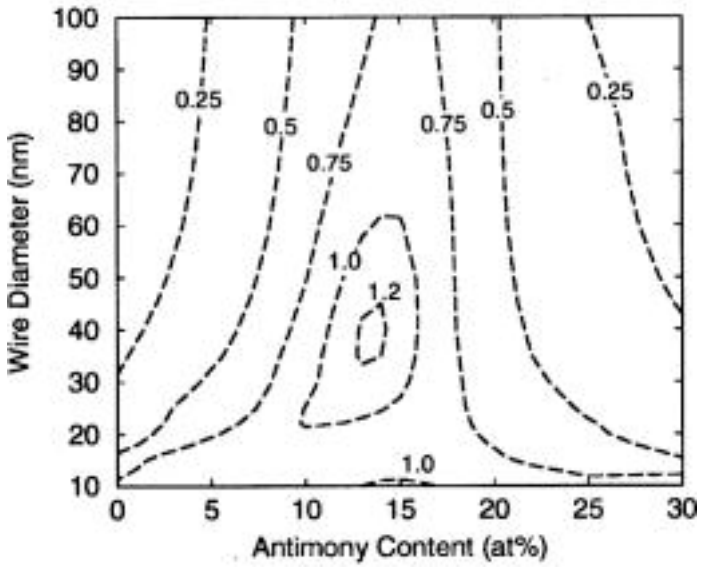


Figure 1.3. Contour plot of the optimal *ZT* values for *p*-type $Bi_{(1-x)}Sb_{(x)}$ nanowires versus wire diameter and antimony concentration[1]

Table 1.2. *ZT* Values of Materials

| Material | Thermoelectric Figure of Merit (*ZT*) |
|---|---|
| NANO<br>PbTe – PbSeTe | 1.3 |
| BULK<br>PbTe – PbSe | 0.34 |
| NANO<br>$Bi_2Te_3 – Sb_2Te_3$ | 2.4 |
| BULK<br>$Bi_2Te_3 – Sb_2Te_3$ | 1.0 |
| NANO<br>BiSb | 1.25 – 1.5 |
| BULK<br>BiSb | 0.88 |

### 1.3. Motivation and Research Objective

The potential of ideal electrical properties of 1D nanostructures has created a growth in research with the aim of electronic miniaturization. The implementation of the "bottom-up" approach in manufacturing electronic devices is presumed to surpass the limitations imposed by more traditional "top-down" methods. Miniaturization is one ongoing important development in both biosensor and thermoelectric technology. It has already been reported that nanostructures can enhance the sensitivity of a biosensor by one to two orders of magnitude, due to the large surface area per unit volume ratio, which

allows the immobilization of a larger amount of enzyme or other functional surface layer. The first objective of this research is to develop nanoelectrodes for the detection of lactic acid or *Salmonella* DNA. Due to the miniaturization of these biosensors, the goal is to push the sensitivity detection limits to be able to lower levels of analyte than what has currently been achieved in research. The second objective addressed in this dissertation is the development of small, on – chip, solid – state, active cooling devices for electronic systems that are needed in National Security missions. Current systems are bulky and do not integrate well into miniature electronic systems. The goal of this section of research is to develop a technique to produce $Bi_{(1-x)}Sb_{(x)}$ nanowires for thermoelectric cooling at room temperature with high efficiencies, which can be grown directly on a silicon substrate.

### 1.4. Scope of the Dissertation

This dissertation discusses various aspects of electrochemical treatment of one – dimensional nanomaterials and their applications for biological sensors as well as thermoelectric cooling devices. In particular, a comparative study of two members of the nano – carbon family, carbon nanotubes and nanocrystalline diamond thin films, were selected as the electrode materials of choice for fabrication of biological sensors for the detection of lactic acid and *Salmonella* DNA. For on – chip cooling, bismuth antimony nanowires were selected, due to their theoretically high thermoelectric figure of merit at nano dimensions.

Chapter 1 begins with a brief overview of the selected nanomaterials: carbon nanotubes, nanocrystalline diamond thin films, and bismuth antimony nanowires. The

mechanical, electrical, and thermal properties of the aforementioned materials are discussed, as well as why each is an ideal candidate for the particular chosen application.

Chapter 2 presents an extensive literature review on the history and synthesis of one – dimensional nanomaterials, with special attention to the methods used to fabricate the nanomaterials used in this research. A review of nanoscale biosensors as well as thermoelectric devices are included as background for the reader.

Chapter 3 discusses the basic theory of the science of electrochemistry. Electrode kinetics as well as the Helmholtz diffusion layer are reviewed as well as a detailed examination of Electrochemical Impedance Spectroscopy (EIS) and Cyclic Voltammetry (CV). Data interpretation, the equivalent circuit model, oxidation and reduction, and electrochemical – based sensing are all topics highlighted in this chapter.

Chapter 4 presents the materials, methods, and results of the functionalized carbon – based materials for biological sensing. An approach towards the development of nanoscale electrodes is discussed, as well as electrochemical and fluorescence – based detection methods. Several characterization methods are also presented for each electrode.

Chapter 5 presents the materials, methods, and results of the development of bismuth antimony nanowires for nanoscale thermoelectric devices. The $Bi_{(1-x)}Sb_{(x)}$ nanowires were patterned in an anodized aluminum oxide template, and an overview of the fabrication process of the template used for the nanowire growth is also presented.

This section concludes with some preliminary data on the thermoelectric figure of merit for the nanowires.

Finally, Chapter 6 concludes the dissertation with a summary of current investigations regarding this research. Some proposed suggestions for future work in this area are also stated.

# CHAPTER 2: BACKGROUND AND LITERATURE REVIEW

In agreement with the "bottom up" approach, the control of nano "building blocks" is central for the realization of future electronic nanodevices. Several methodologies exist, including solution – based and gas – based growth. Size and shape control can be achieved with a template, which can be employed in quite a few different synthetic routes. In this section, we will discuss the primary growth techniques of 1D nanostructures as well as a few unique approaches and examine trends in the research and technology.

## 2.1. Template – Directed Nanowire Synthesis

A simple method for one-dimension nanostructure synthesis employs the use of a template such as anodic aluminum oxide (AAO), nanochannel glass or porous polymer films. In this technique, the generated nanostructure has complimentary morphologies to that of the template in which the template contains very small holes within the host material and these empty spaces are filled with a chosen material to form nanowires.

### 2.1.1. Template Synthesis

The material properties of the template as well as characteristics such as pore diameter, uniformity and pore density are important considerations for template-directed synthesis. While difficult to achieve by photolithographic techniques, templates offer a high channel aspect ratio. O'Sullivan and Woods[25] presented a model describing the

anodization of aluminum films in acid. Under carefully chosen anodization conditions, the resulting oxide film possesses a close-packed array of columnar cells, each containing a central pore of which the size and interval can be controlled by changing the forming conditions. The main driving force in the formation of the channel in the anodic alumina is the electric field, which allows the continuous growth of the ordered channels regardless of crystal orientation. It is believed that the formation of a self-ordered hexagonal pore array is due to the mechanical stress associated with the expansion of the aluminum during oxide formation.[26] Masuda *et al.*[27] reported a growth procedure which enabled long-range ordered channel-array architecture on the millimeter scale. Here, a nanoindentation technique was utilized to pretexture the aluminum by a mold of shallow concaves to initialize pore growth with high aspect ratios at the beginning stage of anodization. It has been found that obtaining anodic porous alumina via a two step molding process versus the conventional one step embedding process presents distinct advantages such as chemical and thermal stability and higher mechanical strength.[28] In Masuda and Fukuda's process, fabrication of the negative type of anodic porous alumina and subsequent formation of the positive type structure led to the formation of a porous material with a geometrical structure identical to that of anodic porous alumina. Other groups have modified this process to remove the oxide layer during the first anodization in an acidic solution followed by a second anodization under the same conditions.[29] In this last step the aluminum film becomes the template for growing ordered pores.

Two other materials that have received attention in this field are nanochannel glass and porous polymer films. Nanochannel glass (NCG), a matrix characterized by small, high density uniform channel arrays, has also been widely investigated as

templates for nanowire growth.[30, 31] NCG replica membranes are metal thin films which possess the same channel geometry as the underlying matrix. Tonucci *et al.*[32] initially confirmed that it is possible to use these membranes with channel diameters between 500 nm to 8 μm to obtain a 50 Å GaAs/AlGaAs quantum well by molecular beam epitaxy (MBE). Polymer templates offer good control over nanowire diameter and interwire spacing.[33] The templates can be constructed on any conducting surface and eliminate the need for removal of a barrier oxide layer. Thurn-Albrecht *et al.*[34] created an array template from diblock copolymers of polystyrene and polymethylmethacrylate P(S-b-MMA). The diblock copolymer films were annealed above the glass transition temperature between two electrodes, which caused the formation of a hexagonal array of channels perpendicular to the film surface. After removal of the PMMA, the resulting polystyrene film possessed pores with 14 nm diameter and densities in excess of $1.9 \times 10^{11}$ pores/cm$^2$.

### 2.1.2. Electrochemical Deposition

Electroplating is an ancient science used to deposit a layer of metal on an object and recently has lent itself to the fabrication of nanostructured materials. The use of a template-assisted method to deposit metal nanostructures has significantly increased in recent years. Structures that can be realized through this technique include nanowires [Bi[35], Ag[36] and ZnO[37]], tubes [carbon[38] and Cu[39]], dots [Co[40] and Au[41]], rods [$Ga_2O_3$-$Al_2O_3$[42]], composite [polyaniline/$Bi_2Te_3$[43] and Fe-Ga alloys[44]] and superconducting materials [Sn[45]]. During electrochemical deposition, the template is attached to the cathode for electroplating. When an electric field is applied between the cathode and

anode the cations are attracted to and reduce at the cathode, which results in nanowire growth in the pores of the template. The length of the nanowires depends on the length of the porous channels, which can be controlled during the electroplating process.

In 1996 Routkevitch *et al.*[46] first produced semiconducting nanowires by electrochemical deposition in AAO templates. In this study, CdS nanowires were synthesized with diameters in the range of 9 – 35 nm and lengths up to 1 μm. Single step ac electrolysis was used to deposit CdS nanowires directly in the pores of AAO without the removal of the barrier oxide layer in an electrolyte containing $Cd^{2+}$ and S in dimethylsulfoxide. Since rectification only occurs inside the pores and not at defects, no material is deposited in any cracks in the template. The CdS nanowires were found to have a preferential *c*-axis crystal orientation along the length of the pores of the AAO template.

### 2.1.3. Pressure – Injection

In certain applications it is desirable to produce high crystalline nanowires with a preferred crystal orientation along the wire axis. In these instances, a high-pressure injection (HPI) method is used to fabricate such nanowires from low melting point materials or templates with exceptionally high mechanical strength. In the HPI method, the nanowires are formed by pressure injecting the desired material in liquid form into the evacuated pores of the template. Due to the heating and the pressurization processes, the templates used for the pressure injection method must be chemically stable and be able to maintain their structural integrity at high temperatures and at high pressures. Huber *et al.*[47] reported on the growth of 200 nm Bi-Sb allow wire arrays by HPI of the metal into

the pores of alumina templates. An external pressure is used to overcome the interfacial energy and to impregnate a nanochannel that does not usually wet with the molten metal. This pressure is given by the Washburn[48] equation:

$$P = -4\gamma \cos\theta / d \qquad (2)$$

where $P$ is the external pressure needed to fill a channel of diameter $d$, $\gamma$ is the surface tension of liquid, and $\theta$ is the contact angle between the liquid and the channel walls of the anodic alumina template. In this work it was assumed that $\theta$ = 180° so that for an applied pressure of 4 kbar all channels larger than 3.8 nm would be filled with liquid Bi.

### 2.1.4. Sol – Gel Deposition

Traditionally, the sol-gel process has allowed the fabrication of a large variety of materials including ultra-fine powders, monolithic ceramics and glasses, inorganic membranes, thin films and coatings of metal oxides and recently has evolved into a useful approach for synthesizing one-dimensional nanostructure arrays with good crystalline properties. The sol-gel process involves the transition of a system of colloidal particles (the sol) into a solid phase (the gel). The foundation of this technique is the hydrolysis of a solution of precursor molecules to obtain a suspension of colloidal particles and then condensation of such particles to yield a new gel phase. The main advantages of sol-gel techniques over conventional synthesis procedures include low temperature of processing, versatility, and easy chemical doping.

Several metal oxide nanowires including $LiCoO_2$[49], $LiMnO_2$[50], $LiNiO_3$[51], and $TiO_2$[52] have been successfully synthesized via the sol-gel process. Precursors for metal

oxide nanostructures are molecules already processing metal-oxide bonds such as alkoxides or oxoalkoxides. Cheng and Samulski[53] were the first to use the sol-gel alumina templating method for the fabrication of $In_2O_3$ and $Ga_2O_3$ nanotubes. A porous alumina membrane was used as a template by immersing it in a sol of $In^{3+}$ or $Ga^{3+}$ and then it was dried in air before annealing. The resulting length of the tubes was 50 μm, approximately the same as the thickness of the template and the outer diameter was 200 nm, the template pore size. Here, the tubes appear to be coagulated due to the solvent surface tension in the template dissolution step. Cubic zirconia nanowire arrays have also been produced using the sol-gel template method with a zirconyl chloride precursor[54]. The formation mechanism was caused by the positively charged sol particles being attracted to the negatively charged pore walls of the template.

### 2.2. Vapor Phase Growth

Vapor phase growth is a considerably popular and extensively used mechanism for the synthesis of one dimensional nanostructures such as nanowires, belts and whiskers. Control of the supersaturation level determines the structural growth morphology. Among the vapor phase growth methods which will be discussed in detail include vapor-liquid-solid (VLS) and vapor-solid (VS) growth.

#### 2.2.1. Vapor – Liquid – Solid Mechanism

The VLS method for nanowire growth has been widely successful. In 1964, Wagner and Ellis described this mechanism for the growth of silicon whiskers.[55] In this case, a liquid gold particle is deposited on the surface of a Si wafer and heated, forming

an Au-Si alloy. This liquid alloy/solid interface promotes the anisotropic crystal growth. The liquid becomes supersaturated with Si and as it precipitates out the whiskers are formed. Generally, 1D growth is induced by the dissolution of gaseous reactants into liquid droplets of a catalyst material, followed by nucleation and growth of single-crystalline nanostructures. The primary steps in a typical VLS growth process (metal alloying, crystal nucleation and axial growth) are shown schematically (Figure 2.1.). It is shown that the metal liquid alloy forms at the eutectoid temperature. Wu and Yang[56] reported the first real time *in situ* TEM growth studies of Ge and Si nanowires. Nanowire nucleation begins once the liquid droplet is supersaturated with Ge, usually at about 50 – 60 wt% Ge. Once nucleation begins, further dissolution of Ge vapor increases the amount of Ge precipitation from the alloy. These experiments also determined that there is a direct linear relationship with respect to the initial catalyst particle size and the final nanowire diameter. Gudiksen and Lieber confirmed the correlation by showing that selective size diameter GaP nanowires can be synthesized by controlling the diameter of gold catalyst nanoparticles.[57]

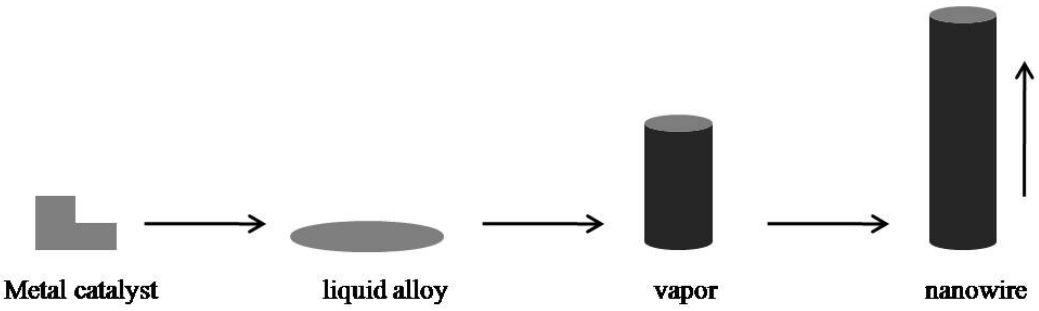


Figure 2.1. The VLS growth process (adapted)[56]

In the past 5 years, the VLS method has become widely used for the generation of 1D inorganic nanostructures, including oxides [ZnO, $SnO_2$, ITO, MgO][58-61], III-V semiconductors [GaN, GaAs, InAs, InP][62-65], II-VI semiconductors [ZnS, ZnSe, CdS, CdSe][66-69] and recently CdS/Si coaxial nanowires.[70] These new CdS/Si nanowires possessed a crystalline CdS core and a Si sheath. They were prepared with an Au catalyst and had average diameters of 100 nm and lengths up to a few hundred microns. In 2004 Wu *et al.*[71] reported on molecular size silicon nanowires grown by VLS mechanism. The silicon nanowires were grown with silane and hydrogen as a carrier gas and exhibited little or no amorphous oxide layer down to 3 nm diameter due to passivation of the growth surface with $H_2$. The authors also report that the SiNWs demonstrate a clear preference for growth along the <110> direction in the smallest (3 – 10 nm) nanowires and along the <111> direction in larger (20 – 30 nm) nanowires. Further study indicates that surface energy plays an important role in the VLS growth mechanism of these SiNWs.

Other vapor-liquid-solid mechanisms include pulsed laser deposition (PLD), chemical vapor deposition (CVD), metal-organic chemical vapor deposition (MOCVD) and physical vapor deposition (PVD). In general, PLD includes a laser beam which strikes a target while inside a vacuum chamber. A bit of the target material is vaporized and sub sequentially deposited on a substrate that is facing the target. Morales and Lieber[72]have reported an approach to the synthesis of single-crystal nanowires that exploits laser ablation to prepare nanometer-diameter catalyst clusters that subsequently define the size of wires produced by a VLS mechanism. The catalysts were prepared by a pulsed, frequency-doubled Nd-yttrium-aluminum-garnet laser that was used to ablate

the targets that contain the element desired in the nanowire and the metal catalyst component. Chemical vapor deposition (CVD) is a form of VLS with nanoscale metal catalysts. In the simplest form, this type of system involves a catalyst which is heated to high temperatures in a vacuum furnace while chemical precursors in gaseous form flow through the tube reactor for a period of time. Materials grown over the catalyst are collected upon cooling the system down to room temperature (Figure 2.2.). Recently, MOCVD has been utilized to grow catalyst-free ZnO nanowires directly on a Si substrate[73, 74]. A typical ZnO nanostructure growth process occurs in a low-pressure chamber with high-purity diethyl zinc (DEZn) and $N_2O$ as the zinc and oxygen sources, respectively, and nitrogen as the carrier gas. ZnO nanostructures can be grown via a two-step process, wherein the first step produces a thin nucleation layer of ZnO which is then annealed and the nanostructures are grown on this nucleation site. The PVD process can be used to deposit nanowires and other structures onto a substrate by physical means, unlike a chemical deposition process. Wu and Tao[75] have reported on cubic and hexagonal CdS nanowires grown by PVD of CdS powders. These powders were placed in an alumina boat and heated in a horizontal furnace with Ar gas flow. The nanowires were about 100 nm in diameter and up to 10 microns long.

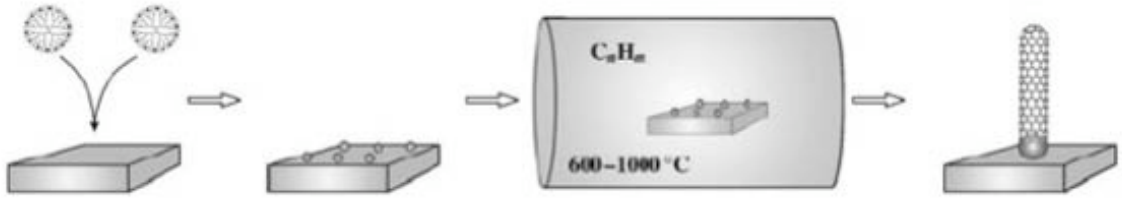


Figure 2.2. Schematic of a CVD process[76]

### 2.2.2. Carbothermal Growth

Nanowires of metal oxides in particular have been shown to grow favorably with the use of carbon during synthesis. This technique details the heating of a metal oxide in the presence of carbon to produce a metal suboxide nanowire. $Al_2O_3$ nanowires and nanotubes were synthesized via such a procedure involving the use of a mixture of Al and graphite or active carbon powders[77]. In this method a finely ground mixture of Al with (a) graphite powder or (b) activated carbon were placed in a zirconia boat and heated under argon gas flow. The result produced white wood like structures from (a) and fine gray structures from (b). The procedure that produced the $Al_2O_3$ nanostructures can be understood based on the following vapor-solid mechanism reactions:

$$Al(s) + C(s) + O_2(g) \rightarrow AlO_x(v) + CO(g) \quad (3)$$

$$AlO_x(v) + O_2(g) \rightarrow Al_2O_3(s) \quad (4)$$

Lin and Lin[78] have recently shown that the growth of SiONWs via the carbothermal reduction of metal oxides is a viable production mechanism. Here powders of CuO and graphite were mixed and placed in an alumina boat and the oxide was removed. The substrates were then placed 2 mm above the CuO/C mixed powders in the furnace. The SiONWs grew without the presence of a catalyst under Ar gas flow and at elevated temperatures of 1000 – 1100 °C. TEM analysis proved the nanowires were amorphous and free from Cu. The reactions for this case are as follows:

$$2CuO + C \rightarrow 2C + CO_2(g) \quad (5)$$

$$CO_2(g) + Si(s) \rightarrow SiO(g) + CO(g) \quad (6)$$

$$SiO(g) + \tfrac{1}{2}O_2 \rightarrow SiO_2(s) \quad (7)$$

### 2.2.3. Vapor – Solid Growth

Vapor-solid growth has been used extensively to produce nanostructures, including oxide nanowires in particular. In a typical VS process, the vapor species is generated by evaporation, reduction, or other gaseous reactions. These species are then condensed onto the surface of a solid substrate in a temperature zone lower than that of the source material. 1D growth will proceed without the need of a metal nanoparticle catalyst if the supersaturation is kept at a controlled, low level.

### 2.2.4. Oxide – Assisted Growth

Lee *et al.*[79] presented an oxide-assisted growth mechanism for the synthesis of silica nanowires. Silica nanoparticles acted as nucleation catalysts as well as provided oxygen and silicon for the SiO NW growth. A graphitic carbon layer formed around the catalytic nanoparticles and the silica nanowires nucleated from this site, indicative of the VS growth mechanism. The Fe films act as a catalyst decomposing $CH_4$ gas into carbon and hydrogen atoms.

## 2.3. Solution Based Growth

An alternative to chemical based methods is solution based growth of 1D nanostructures. The primary advantage of solution based methods as opposed to the

vapor phase option is the ability to perform the growth at lower temperatures on a wide variety of substrates. Another advantage is the ability to control the size and shape of the nanostructure, which can often be controlled by solution-liquid-solid (SLS), solvothermal, and hydrothermal growth mechanisms.

### 2.3.1. Solution – Liquid – Solid Methods

Buhro and coworkers[80, 81] developed a SLS growth process that is similar to the VLS process for production of crystalline III-V semiconductors (InP, InAs, GaAs). They determined that the distinguishing features of SLS growth are a solution dispersion of small liquid flux droplets, a solution phase that feeds the elements of the crystal phase into the flux droplets, and pseudo-one-dimensional growth of the crystal phase from the flux droplets after supersaturation is achieved. During SLS the precursors are delivered and react in the solution rather than the vapor phase. A simple method for crystallizing the III-V compounds utilizes metal catalysts (i.e. Bi, Sn, In) with the desired nanomaterial produced by organometallic reactions at low temperatures in hydrocarbon solvents. The products had small crystal dimensions with whisker morphologies. The organometallic reactions are similar to those that take place during typical organic metal chemical vapor deposition (OMPVD) at higher temperatures.

The SLS method was modified by Holmes and coworkers[82] to a supercritical fluid liquid-solid (SFLS) approach for Si nanowires growth. The ability to precisely self-assemble Si nanowires in solution was achieved by using solvent-dispersed, size-monodispersed, alkanethiol-capped gold (Au) nanocrystals to direct the nanowire growth with narrow wire diameter distributions. In this procedure, the sterically stabilized Au

nanocrystals and a Si precursor, diphenylsilane, were co-dispersed in hexane that was heated at high temperatures where the diphenylsilane was able to decompose to form Si atoms. The Si-Au phase diagram indicates that Si and Au can form an alloy phase in equilibrium with pure solid Si when the Si concentration with respect to Au is greater than 18.6 mol% and the temperature is above 363 °C. Under these reaction conditions, the Si atoms dissolved into sterically stabilized Au nanocrystals until supersaturation, at which point they were then expelled from the particle as a thin Si nanowire. The produced nanowires had highly crystalline cores, aspect ratios greater than 100, and tunable crystallographic orientation.

### 2.3.2. Hydrothermal and Solvothermal Methods

Hydrothermal and solvothermal synthesis mechanisms can provide precise control over nanoscale morphologies by varying the parameters of the system. Both methods produce nanowires at low temperatures when compared to vapor-phase methods. One of the primary advantages of hydrothermal methods is that it simply uses water as the solvent. ZnO nanowires grown on nanostructured thin film via a hydrothermal route was first demonstrated by Vayssieres[83]. The synthesis was conducted on a nanostructured ZnO film by the thermal decomposition of a $Zn^{II}$ anime complex in an aqueous solution of zinc nitrate and methenamine (HMT) heated at 95 °C for several hours. The resulting single crystalline hexagonal nanorods were about 10 – 20 nm in diameter and up to 10 microns long. Sun *et al.*[84] has since demonstrated growth of high density arrays of ZnO nanowires on a PLD ZnO coated thin film. Gao *et al.*[85] demonstrated a facile route to synthesize $\alpha$-$MnO_2$ nanowires by hydrothermal treatment of $KMnO_4$ and $NH_4Cl$. A

typical procedure involved mixing 1 mmol each of the previously mentioned compounds in distilled water and placing the solution in an autoclave maintained at 140 °C for 24 hr. In this procedure $K^+$ and $Cl^-$ existed in the solution the entire time while $NH_4^+$ and $MnO_4^-$ were consumed completely by the end of the reaction. More research is still needed to completely understand the role $Cl^-$ plays in the structure formation. The $\alpha$-$MnO_2$ nanowires had diameters of 10 – 30 nm and lengths up to 6 – 10 microns. Considerable progress has been made in the area of hydrothermal synthesis of other one dimensional nanostructures, including ZnS[86] and TiO[87].

Similar to the hydrothermal mechanism, the solvothermal method utilizes organic solvents instead of water. This solvent is maintained at relatively high pressures and temperatures above its critical point in order to increase the solubility of the solid and to speed up reactions between solids. In a typical solvothermal process, such a solvent is mixed with metal precursors and crystal growth regulating or templating agents, such as amines. This solution mixture is placed in an autoclave kept at high temperatures and pressures to allow the reaction to proceed and to carry out the nanowire growth. The solvothermal mechanism is appropriate for most types of solid materials due to the advantage that most materials can be made soluble in a specific solvent under proper heating and pressurizing of the solution. Heath and LeGoues[88] first used this method to synthesize germanium nanowires with high aspect ratios by reducing a mixture of $GeCl_4$ and phenyl-$GeCl_3$ at high temperature and high pressure. Qingqing and coworkers[89] have reported a simple, reproducible, nontoxic solvothermal method to produce CeS nanowires which does not require any solid templates or complicated surfactants and can be used to synthesize other sulfide nanostructures. In this process $CdCl_2$ and S were mixed in an

organic solvent and placed in an autoclave at 200 °C for 12 hr. After cooling the resulting nanostructures were filtered off and characterized. The CdS nanowires grew along the c-axis because the <001> faces have the fasted growing rate due to the closed-packing factor. X-ray diffraction (XRD) and TEM verified that the CdS nanowires are hexagonal in structure and have diameters of 40 nm and lengths up to 10 microns.

The solvothermal process can also be used to produce a variety of non-oxides. Solvothermal-based growth for III-V semiconducting nanostructures provides the advantage of a simple growth process that does not require extreme environment conditions without the use of organometallic or toxic precursors nor the need for post-treatment at elevated temperatures for crystallization to occur. Qian and coworkers[90-92] have demonstrated the solvothermal method for the preparation of nanocrystalline III-V semiconductors InP, GaN, and InAs. The following liquid-solid reactions take place in the autoclave for each respective III-V semiconducting nanostructure:

$$InCl_3 + Na_3P \rightarrow InP + 3NaCl \quad (8)$$

$$GaCl_3 + Li_3N \rightarrow GaN + 3LiCl \quad (9)$$

$$InCl_3 + AsCl_3 + 3Zn \rightarrow InAs + 3ZnCl_2 \quad (10)$$

The solvent used in a typical solvothermal growth mechanism is chosen due to its specific ability to dissolve the desired compound. In the case of nanocrystalline InP, 1,2-dimethoxyethane (DME) was used as the solvent to dissolve $InCl_3$ in an autoclave at 180 °C for 12 hr. The resulting InP nanostructures were about 12 nm in diameter and spherical in shape. Benzene was selected as the solvent for $GaCl_3$ and $Li_3N$ and the

solution was autoclaved at 280 °C for 12 hr. From reaction (9) above, hexagonal GaN nanocrystallites were formed. Last, $InCl_3$, $AsCl_3$ and Zn powders were dissolved in xylene and positioned in an autoclave at 150 °C for 48 hr. InAs nanostructures with particle size about 15 nm were produced via this simultaneous co-reduction route. XRD verified that there was no presence of indium oxide nor arsenic oxide.

Recently, Wang *et al.*[93] reported that the size and shape of CdSe and CdTe nanocrystals posses a direct relationship with the initial precursor concentration during solvothermal-based growth. It was found that at lower initial monomer concentrations, dot-shaped nanocrystals were only obtained with relatively narrow size distribution, while higher initial monomer concentrations could give rise to elongated nanocrystals and their increase resulted in the increase in quantity of the multi-armed rods. The simplicity and convenience of the solvothermal route lends the procedure to generate a wide variety of one-dimensional nanostructures while the low-cost involved is promising for practical industry production.

### 2.3.3. Anisotropic 1D Nanostructures

Shape control of nanostructures can be achieved by manipulation of the growth kinetics. Peng and coworkers[94] demonstrated that the growth of CdSe nanocrystals with the wurtzite structure is highly anisotropic when the system is kinetically overdriven by an extremely high monomer concentration. The intrinsically anisotropic structure of wurtzite CdSe, with a unique *c*-axis is enhanced when the overall growth rate is fast and is generally faster along this preferred axis. Furthermore, Gates and coworkers[95, 96] displayed that trigonal nanowires of Se (*t*-Se) were synthesized based on anisotropic

growth of single crystalline Se seeds in solution. The seeds were generated in situ through the solution-solid phase reaction:

$$H_2SeO_3(aq) + N_2H_4(aq) \rightarrow Se(\downarrow) + N_2(\uparrow) + 3H_2O \qquad (11)$$

After the addition of selenious acid, a brick color formed in the solution indicative of *a*-Se spherical colloids. Upon cooling, small amounts of Se dissolved in the solution precipitated out, forming nanocrystallite *t*-Se. In the new mixture of colloids of *a*-Se and nanocrystallites of *t*-Se, the colloids of *a*-Se would slowly dissolve into the solution due to their higher free energies as compared to the seeds of *t*-Se. This dissolved selenium subsequently grew as crystalline nanowires on the seeds. The produced pure Se nanowires possessed uniform diameters as small as 10 nm and lengths up to hundreds of microns.

### 2.4. Other Useful Growth Approaches

There are several potentially useful approaches to one dimensional nanostructure synthesis that need to be further investigated before becoming an economical tool for large scale growth. These mechanisms are promising methods for precise control of a wide range of morphologies of crystalline nanomaterials. Several demonstrations of the novel template method has been shown to produce 1D nanowires and will be discussed further. A positive template method has the advantage that nanowire diameters are not restricted by the size of the template; rather, the diameters are controlled by the amount of metal deposited. By removing the templates after deposition nanostructures can be revealed. Braun and coworkers[97] first constructed a DNA-based positive template to

serve as a scaffold for the growth of a silver nanowire. The first step in their procedure was the self-assembly of DNA between two gold electrodes microns apart. Oligonucleotides with different sequences were attached to each electrode and λ-DNA bridged the electrode pair. After DNA hybridization silver metal was deposited along the DNA molecule. The formation of complexes between the silver and the DNA bases as well as the $Ag^+$ / $Na^+$ ion exchange contributed to selective localization of $Ag^+$ ions along the DNA. The resulting silver nanowire was 100 nm in diameter and 12 μm long. This pinnacle study provided a step towards the development of a DNA template based on a self-assembly process that can be exploited for metal nanowire synthesis to be utilized in electronic device applications. Following this approach, Richter and coworkers[98] were able to develop a DNA template for metallic nanowires which displayed ohmic transport behavior. The metallization of DNA templates also presents new opportunities for applications that require high temperatures that untreated DNA could not withstand.

Instead of using anodic aluminum oxide or polymeric templates for nanowire growth, carbon nano –tube or –fiber based templates are also feasible. CNT and CNF templates have been used for the synthesis of metal[99, 100], metal oxide[101, 102], -nitride[103], -phosphide[104], and carbide[105] nanostructures. Wu and coworkers[106] have filled the hollow cores of CNTs with ZnO nanowires with diameters 20 – 40 nm and lengths 250 – 1000 nm. The CNT templates were first treated with acid and then stirred in a saturated zinc nitrate solution for 48 hrs. Once filtered and dried the as-prepared samples were underwent calcination in argon at 500 °C for 6 hr. The final step was a heat treatment in air to remove the CNT template. Unlike the previous technique, metal nanotubes can be patterned around the outer diameter of carbon nanofibers. Recently, Xie and

coworkers[107] have shown metal nanowire growth on carbon nanofiber templates via electroless deposition. The CNFs were prepared by a typical CVD route, treated, and the suspended in a solution of sodium dodecyl sulfate (SDS). They were then sensitized and activated before deposition. For Ni-P electroless deposition, the CNFs were placed in a solution containing nickel sulfate, sodium hypophosphite as reducing agent, sodium acetate and lactic acid as a stabilizer. The coated nanofibers were annealed to remove the template and then heated under hydrogen flow to remove any oxide layer, resulting in hollow Ni-P nanotubules. The advantage of this method is nanoscale size manipulation: inner diameter of the nanotubes can be precisely controlled by the diameter of the nanowire template while the outer diameters can be controlled by the deposition time.

One novel approach to the development of 1D nanostructures is the use of a virus-based template. Mao *et al.*[108] designed such a scaffold for a diversity of single-crystalline nanomaterials. The incorporation of substrate-specific peptides that exhibited control of size, composition, and phase during nanoparticle nucleation on a bacteriophage template promoted directional growth of semiconducting and magnetic materials. The workers introduced a wide variety of materials (II-VI semiconductors as well as ferromagnetic alloys) to demonstrate the universality of the virus template as opposed to more classical growth mechanisms.

### 2.5. Chemical and Biological Sensing Applications

One dimensional nanostructured chemical and biological sensors are an attractive, versatile application for several reasons. Nanowire sensing probes possess extremely sensitive electrical properties due to their high surface-to-volume ratio. Nanoscale

sensors are also smaller, require less power and detect analytes faster than their macroscale counterparts. Sensors based on one dimensional nanostructures are being developed for lab-on-a-chip devices, for the detection of analytes ranging from those used for biological warfare to indicators of human diseases.

Nanowire chemical sensors operate based on the absorption of analyte molecules, which consequently affects the conductance of the nano-sensor. One major fallback that remains is in making nanoscale sensors more selective so that they can differentiate between analytes in complex solutions. Besteman *et al.*[109] opened the door for biomolecular diagnostics via 1D nanostructure sensors by demonstrating the first biosensor based on single-walled carbon nanotubes. Controlled immobilization of the enzyme glucose oxidase (GOX) on the SWNTs indicated a clear decrease in the conductance of the tube, which can be attributed to a change in the total capacitance of the tube. A typical experiment involves the immobilization of GOX via a linking molecule which binds through van der Waals coupling with a pyrene group on one side and on the other side covalently binds the enzyme through an amide bond. Changes of conductance of the GOX-coated semiconducting SWNTs upon addition of glucose indicated that an enzyme-activity sensor can be constructed at the single molecule level of an individual SWNT. Cui *et al.*[110] modified Si nanowires with amine and oxide groups to create highly sensitive chemical and biological sensors. For the construction of a pH sensor, a Si NW was functionalized by modification of the silicon oxide NW surface with 3-aminopropyltriethoxysilane (APTES). Variations in the pH of the solution into which the nanowire was immersed caused protonation and deprotonation of the $-NH_2$ and –SiOH groups on the surface of the nanowire, where changes of the surface

charge would chemically gate the nanowire. At low pH, the $–NH_2$ is protonated to $–NH_3^+$ and behaves as a positive gate which decreases the conductance, while at high pH the –SiOH is deprotonated to $–SiO^-$, which would correspond to an increase in conductance. The SiNWs displayed a linear response for pH 2 – 9, which suggests that they are capable as nanoscale sensors. Similarly, biotin-modified nanowires demonstrated high sensitivity (down to 10 pM) towards streptavidin. The concept of using nanowires as FETs can be extended in many directions; for example, monitoring several protein expressions for medical diagnostics with an array of nanowires each functionalized separately to detect a specific analyte.

**2.6. Conclusions**

Table 2.1. summarizes different methods to grow nanostructures and the diameter obtained. Due to their small size and high surface area, these structures can be implemented into microelectronic, thermoelectronic or biosensing devices. Finally, in spite of the significant amount of research being carried in the area of one dimension nanostructures, there is still a long way to the commercial use of ODNS because of scaling up the production and retaining the properties during mass production. Especially in biological applications, toxicity and biocompatibility are major issues. To date there is no practical device available using 1-D nanostructures but hopes are still high for the development of significant practical devices from the integration of these structures with conventional micro- and nano- electronics.

Table 2.1. Various growth techniques and corresponding nanowire diameter

| Nanowire/ Nanorods | Growth Process | Source | Diameter (nm) | Application |
|---|---|---|---|---|
| CdS | Electrochemical deposition in AAO templates | $CdCl_2$, elemental sulfur | 9-35 | - |
| $In_2O_3$ and $Ga_2O_3$ | Sol-gel deposition in AAO templates | Indium nitrate, gallium nitratehydrate | 200 | Gas sensor, Opto-electonics |
| Si | CVD | $SiH_4$ | 3-10 | Nano-devices |
| $Zn_2SnO_4$ | VLS | ZnO, $SnO_2$ | 100 | Opto-electronics |
| $MoO_3$ | Hydrothermal synthesis | $MoO_3 \cdot 2H_2O$, tetradecylamine | 50-150 | Gas sensor |
| GaN | Magnatron sputtering | Ti, $Ga_2O_3$ | 50-100 | - |
| ZnO | Thermal evaporation | Zn Powder | 50 | Opto-electronic devices |
| ZnO | Solution route | $Zn[CH_3COOH]_2.2H_2O$, DBS | 95 | Gas sensor |
| $MnO_2$ | Sol-gel | $KMnO_4$, Fumaric acid | 100 | Li ion battery |
| $LiV_3O_8$ | Hydrothermal method | $CH_3COOLi.2H_2O$, $NH_4VO_3$ | 150 | Li ion battery |

Table 2.1. (Continued)

| | | | | |
|---|---|---|---|---|
| $MnV_2O_6$ | Hydrothermal method | $Mn[CH_3COO]_2 .4H_2O$, $H_2O_2$, $V_2O_5$ | 20-30 | Li ion battery |
| $SnO_2$ | Hydrothermal method | $SnCl_4$, NaOH | 4-15 | Gas sensor |

# CHAPTER 3: ELECTROCHEMISTRY THEORY

## 3.1. Introduction

A branch of chemistry, electrochemistry studies chemical reactions which take place in a solution. These reactions take place at the interface between an electrode and an electrolyte and involve the electron transfer between the two. The history of this branch of science dates back to the late 1700's when the Italian physician Luigi Galvani proposed a nervo – electrical substance in animal tissue which is responsible for the contraction on muscles when exposed to an electrical current. From these experiments, the study of electrochemistry took birth and the electrolysis of water atoms as well as the electroplating of metals were discovered soon afterwards. Electrochemistry is responsible for batteries, photovoltaics, metal plating, chemical and biological sensors, and corrosion technology.

## 3.2. Reduction – Oxidation Reactions

Reduction – oxidation (redox) reactions are chemical reactions where atoms have their oxidation number changed. In short, oxidation refers to the loss of electrons or an increase in oxidation state and reduction refers to the gain of electrons, or a decrease in oxidation state. Each reaction by itself is called a "half reaction" because two half reactions are needed to form a complete reaction. The oxidation number is typically defined as an effective charge of an atom in a compound. Chemists use a set of rules to

determine the oxidation number of compounds: (1) For atoms in their elemental form, the oxidation number is 0, (2) For ions, the oxidation number is equal to their charge, (3) For single hydrogen, the number is usually +1 but in some cases it is -1 (4) For oxygen, the number is usually -2 and (5) The sum of the oxidation number of all the atoms in the molecule or ion is equal to its total charge. For example, consider the case of anodization of aluminum metal to form aluminum oxide. The two half reactions are as follows:

$$Al(s) \rightarrow Al^{3+}(s) + 3e^{-} \tag{12}$$

$$O_2(g) + 4e^{-} \rightarrow 2O^{2-}(s) \tag{13}$$

Combining these two half reactions and balancing the electrons on both sides, the final redox reaction is:

$$4Al(s) + 3O_2(g) \rightarrow 2Al_2O_3(s) \tag{14}$$

### 3.3. Electrochemistry Impedance Spectroscopy

The theory of Electrochemical Impedance Spectroscopy (EIS) and its data interpretation through Nyquist and Bode plots is discussed in this section. EIS is a non – destructive material characterization technique and is advantageous over other characterization techniques due to it being economically favorable, simplistic, portable, automated, provides time – dependent data and can operate in harsh environments. Impedance spectroscopy is useful in providing data relating to real world individual components in the system of question. Equivalent circuits are used to model impedance data and are constructed from simple circuit elements such as resistors, capacitors, and inductors to understand the electrochemical behavior of a particular system.

During an impedimetric measurement, a frequency response analyzer is used to impose an alternating current (AC) sinusoidal signal across a sample and the resulting current and voltage response is measured. When this method is applied over a broad range of frequencies, the impedance spectrum is obtained and can be used to identify and quantify processes occurring within the electrochemical system.

Impedance is typically defined as the opposition to AC flow in a complex system. If a system is purely resistive, then this value is simply resistance, represented by an ideal resistor. However, very few real world systems are ideal and most exhibit complex behavior. Ohm's law, as follows:

$$R = \frac{V}{I} \tag{15}$$

where $V$ = voltage (V), $R$ = resistance (Ω), and $I$ = current (A) only applies for non – complex systems. A modified version of Ohm's law is used to determine the impedance of a complex system:

$$Z = \frac{V(t)}{I(t)} = \frac{V_0 \cos(\omega t)}{I_0 \cos(\omega t - \phi)} = Z_0 \frac{\cos(\omega t)}{\cos(\omega t - \phi)} \tag{16}$$

where $Z$ = impedance, $t$ = time (s), ω = radial frequency (radians/s), and ϕ = phase shift. The impedance can be represented as a complex number:

$$Z = \frac{V}{I} = Z_0 \exp(j\phi) = Z_0(\cos\phi + j\sin\phi) \tag{17}$$

This equation can be expressed with a Nyquist plot, where the real part of the impedance can be plotted on the $x$-axis and the imaginary part on the $y$-axis. Each point on the Nyquist plot is the impedance at a particular frequency, with low frequency data

occurring on the right side and high frequency data occurring on the left side. Note that the impedance can be represented as a vector of length |Z| and the angle between the impedance vector and the *x*-axis is the phase shift (Figure 3.1.).

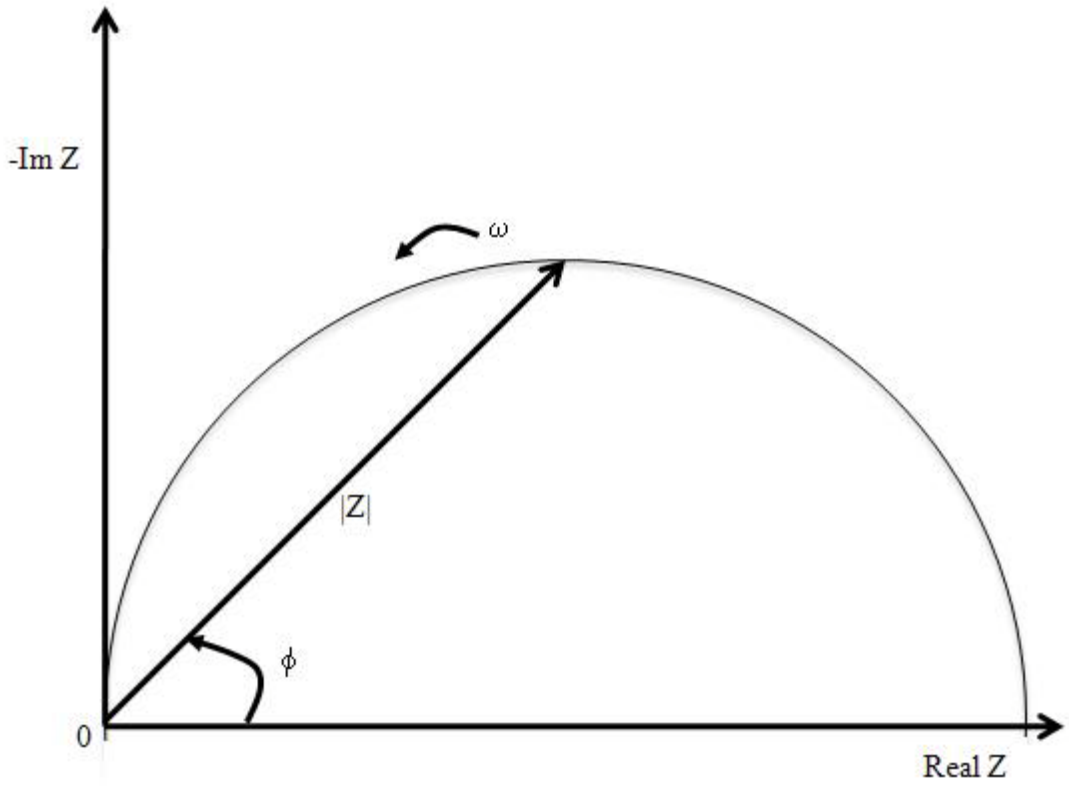


Figure 3.1. Typical Nyquist plot

### 3.3.1. Electrode Kinetics

The different rates of electron transfer can give rise to different electrochemical impedance behavior. Electrical energy can be supplied to a system by the application of a voltage to the electrode. This applied voltage may alter the Fermi level of a metal, making it favorable to reduce or oxidize a species in a solution. In an electrochemical reaction, there are various ways in which a material may move within the solution. This

type of kinetics is called mass transport and is typically divided into three subjects: diffusion, convection, and migration. Movement of ionic species in and out of the electrode/solution interface is also limited by the above mentioned mass transport issues.

Diffusion, driven by a concentration gradient, arises from uneven concentrations of species. Diffusion is particularly important in an electrochemical reaction because the reaction only takes place at the electrode surface. The concentration of the reactant will be lower at the electrode surface than in the bulk solution. Similarly, a higher concentration of the product will be found near the electrode surface than in the bulk solution. In practice diffusion is usually the most significant mass transport issue for most electrochemical reactions.

Convection is the movement of molecules within fluids and is the result of a force on the solution. This force may exist in the form of gravity, a pump, gas flow, etc. Natural convection occurs in all liquids and is the result of very small thermal or density differences within the solution. Forced convection may be introduced into a liquid in order to surpass any effects of natural convection. In electrochemistry, techniques exist such as the use of a rotating disk electrode to introduce forced convection in a systematic manner. A rotating disk electrode will create a laminar flow profile. More details on rotating disk electrode studies are discussed in Chapter 5.

Finally, the third mass transport issue is migration. Migration occurs from the application of a voltage on electrode surfaces and creates a charged interface. Most electrochemical measurements are performed in a background electrolyte (typically a salt solution such as KCl) in order to help protect a species from being attracted or repelled

by electrostatic forces. The background electrolyte also increases the conduction of the solution.

### 3.3.2. The Electrical Double Layer

Figure 3.2. illustrates the electrical double layer of a charged surface when placed in a liquid. The solution is composed of the Inner Helmholtz Plane, Outer Helmholtz plane, and diffuse layer.

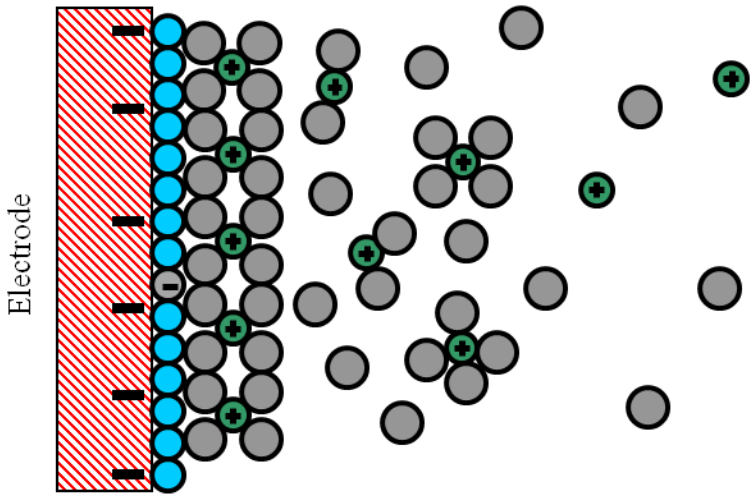


Figure 3.2. The electrical double layer

As seen in the figure, the Inner Helmholtz Plane is the layer closest to the electrode that may molecules specifically absorbed onto the electrode surface. The Outer Helmholtz Plane contains solvated ions, which are nonspecifically absorbed. The diffuse layer constitutes solvent molecules as well as solvated ions in distribution. The characteristic thickness of the double layer is the Debye length, which is reciprocally proportional to the square root of the ion concentration:

$$\kappa^{-1} = \sqrt{\frac{\varepsilon_0 \varepsilon_r kT}{2N_A e^2 I}} \quad (18)$$

where $I$ = ionic strength of the electrolyte (mole/m$^3$), $\varepsilon_0$ = permittivity of free space, $\varepsilon_r$ = dielectric constant, $\kappa$ = Boltzman constant, $T$ = temperature (K), $N_A$ = Avogadro number, and $e$ = elementary charge. Most of the voltage drop across the electrode – electrolyte interface occurs in the electrical double layer.

### 3.3.3. The Equivalent Circuit

Equivalent circuit modeling of electrochemical impedance spectroscopy data is very useful because this technique allows scientists to extract physically meaningful information from modeling the data in terms of ideal electrical circuits composed of resistors (R), capacitors, (C), and inductors, (L). For example, most equivalent circuit models contain a resistor that represents the electrochemical cell's solution resistance. Resistors are also used to represent the resistance to charge – transfer at the electrode surface. The electrical double layer is characterized by capacitors and inductors which represent space – charge polarization regions. In certain instances real – world systems do not behave ideally, so we also use specialized circuit components such as the constant phase element (CPE) and the Warburg element ($Z_w$). The Warburg element is used to represent the diffusion or mass transport impedance of the cell. Table 3.1. lists common circuit elements, their current versus voltage relationship, and their impedance.

Table 3.1. Simple electrical circuit elements

| COMPONENT | RELATIONSHIP | IMPEDANCE |
|---|---|---|
| Resistor | $V = IR$ | $Z_R = R$ |
| Capacitor | $I = C\frac{dV}{dt}$ | $Z_C = \frac{1}{j\omega C} = -\frac{j}{\omega C}$ |
| Inductor | $V = L\frac{dI}{dt}$ | $Z_L = j\omega L$ |

Often, when a capacitor does not behave ideally in an EIS experiment, it acts as a constant phase element. This is usually the case for the electrical double layer capacitance. It is seen in the previous table that an ideal capacitance has an impedance represented by $Z_C = \frac{1}{j\omega C}$, where ω = 2π*f* is the angular frequency, *f* = frequency (Hertz), and *C* = capacitance. The impedance of a constant phase element takes a form of this equation:

$$CPE = Y_0 \frac{1}{j\omega^n} \tag{19}$$

where $Y_0$ is a constant equal to the ideal capacitance, *n* is a parameter ($0 < n < 1$, $n = 1$ for ideal behavior) , and ω is the angular frequency.

Sometimes, it is more convenient to characterize an electrochemical cell in terms of admittance rather than in terms of impedance. Admittance is the measure of how

easily a circuit will allow current to flow and is mathematically represented as the inverse of impedance. For a constant phase element, the admittance is as follows:

$$Y_{CPE} = Y_0(jw)^n \tag{20}$$

where $Y_0$ is the magnitude of the real part of the CPE and $n$ is a parameter ($n$ = 1 for ideal behavior).

Other than the constant phase element, there are several physical properties that can be represented by equivalent circuit elements. The solution resistance of the electrolyte is a function of ionic concentration and the geometry of the electrode area. This value is calculated from the experimental data. In general, solution resistance is defined as:

$$\mathrm{R_s} = \rho \frac{l}{\mathrm{A}} \tag{21}$$

where ρ is the solution resistivity, $l$ is the length carrying a uniform current, and A is the electrode area. The double layer capacitance is a function of electrode potential, ionic concentration, oxide layers, surface roughness, impurities on the electrode surface, temperature, and other factors. As ions stick to the electrode surface, the double layer is formed. Polarization resistance is formed with an electrode is polarized. This happens when a potential is applied to an electrode that is different than its open circuit potential. Polarization resistance is modeled using a simple resistor. In many electrochemical reactions, a current density must be supplied that is large enough to overcome the charge transfer resistance. The equation for charge transfer resistance is:

$$R_{ct} = \frac{RT}{nFi_0} \quad (22)$$

where $i_0$ = current density, $R$ is the gas constant, $T$ = temperature (K), $n$ = number of electrons, and $F$ = Faraday's constant. The Warburg impedance is related to impedance caused by diffusion and is frequency – dependent. The equation for infinite Warburg impedance is:

$$Z_W = \sigma(\omega)^{-\frac{1}{2}}(1 - j) \quad (23)$$

### 3.3.4. Impedance Data Interpretation

Nyquist and Bode plots are used to represent EIS data. Nyquist plots are drawn in the complex plane and show the imaginary impedance versus the real impedance of the electrochemical cell. Nyquist plots often contain one or more semicircles and it is the shape of this arc that provides information into the physical characteristics of the analyzed system. The primary disadvantage to the Nyquist plot is that the frequency – dependence is implicit. On the other hand, Bode plots explicitly illustrate the frequency – dependence of the impedance. Bode plots demonstrate the magnitude of the impedance and the phase angle as a function of frequency. Figure 3.3. is an example of a Nyquist and Bode plot for a typical Randles circuit, which is one of the simplest cell models. It contains a solution resistance, a double layer capacitor, and a charge transfer resistance. The solution resistance is determined by the *x*-axis intercept at the left – hand side (high frequency side) of the semicircle. The diameter of the semicircle is the polarization resistance. The equivalent circuit model for the Randles cell is shown in Figure 3.4.

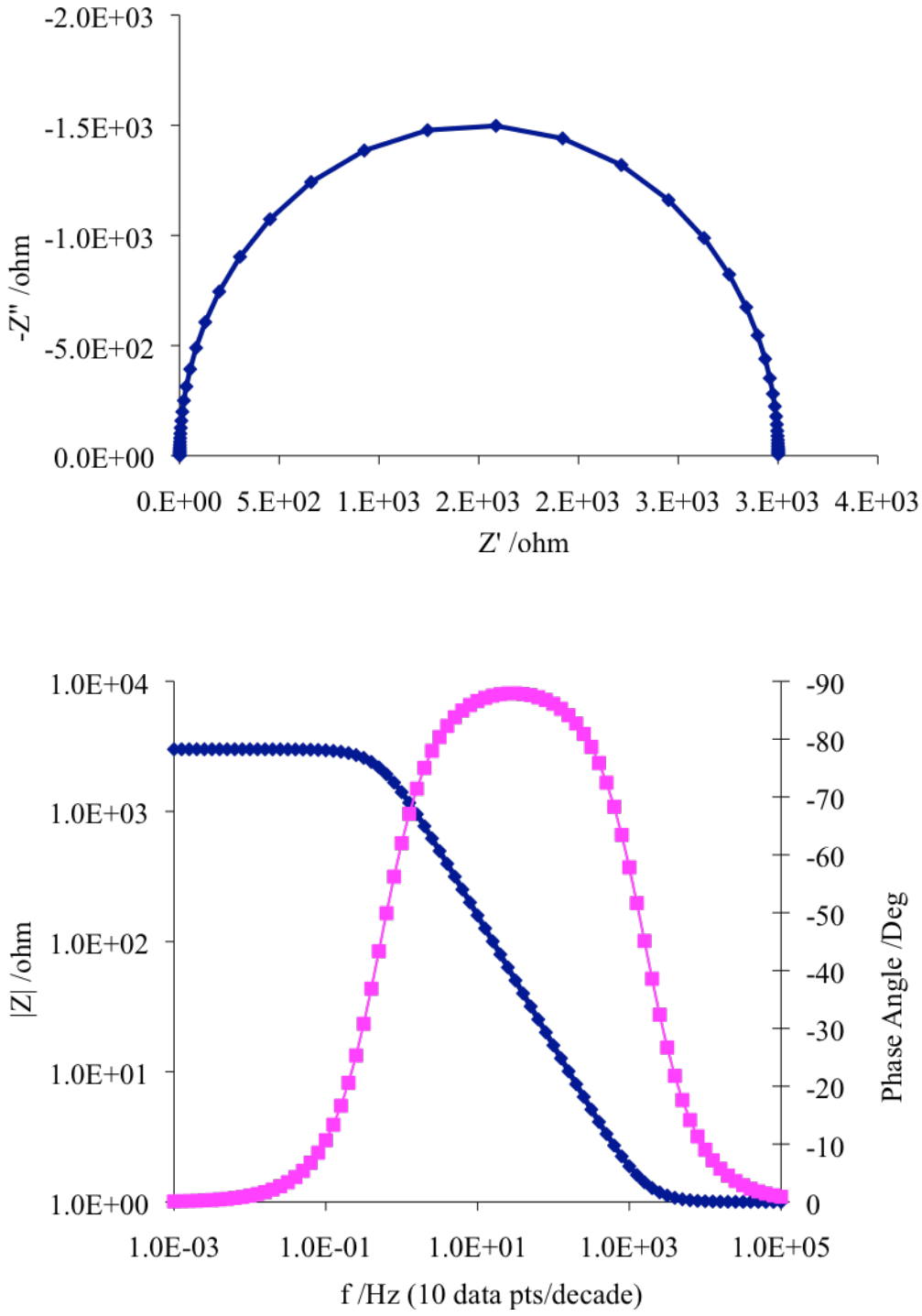


Figure 3.3. Nyquist and Bode plots for a typical Randles cell

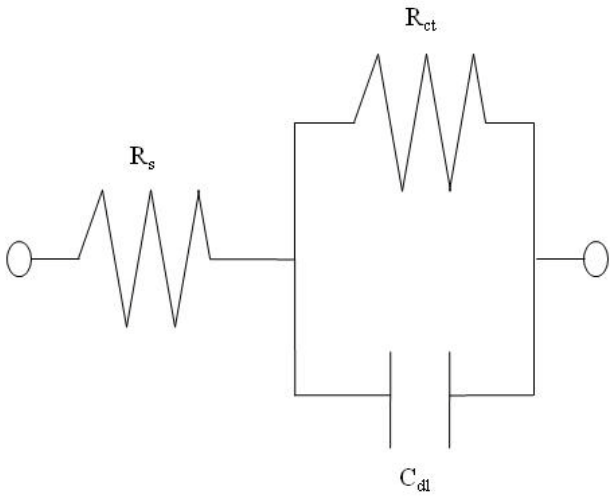


Figure 3.4. Equivalent circuit for a typical Randles cell

### 3.4. Cyclic Voltammetry

Cyclic voltammetry (CV) is a type of electrochemical measurement where the potential of the working electrode is ramped in a linear fashion versus time. After the end potential is reached, the potential is inverted. In a cyclic voltammogram, the current at the working electrode is plotted versus the applied potential. Depending on the analysis needed, one full cycle or a series of cycles is performed. The reduction or oxidation at the surface of the working electrode at a particular applied potential, results in mass transport of material to the electrode surface. The analytical advantages of cyclic voltammetry include a wide dynamic range, extreme sensitivity to low concentrations of ionic species, ease of use, and is a nondestructive method for characterizing electron – transfer mechanisms. Figure 3.5. is an example of a cyclic voltammogram of 0.5 mM potassium ferricyanide in 0.5 M KCl supporting electrolyte with a polished glassy carbon working electrode at a scan rate of 100 mV/sec. Notice that the current increases as the

potential reaches the reduction potential and then decreases as the concentration of ions is depleted close to the electrode surface. Also, the oxidation peak ($E_{pc}$) and reduction peak ($E_{pa}$) have a similar shape and current density magnitude, indicating that the reaction is nearly ideally reversible, meaning that the product is reoxidized from the first reduction reaction. Reversible redox couples will display a ratio of peak currents at oxidation and reduction that is nearly unity ($i_{pa}/i_{pc} = 1$).

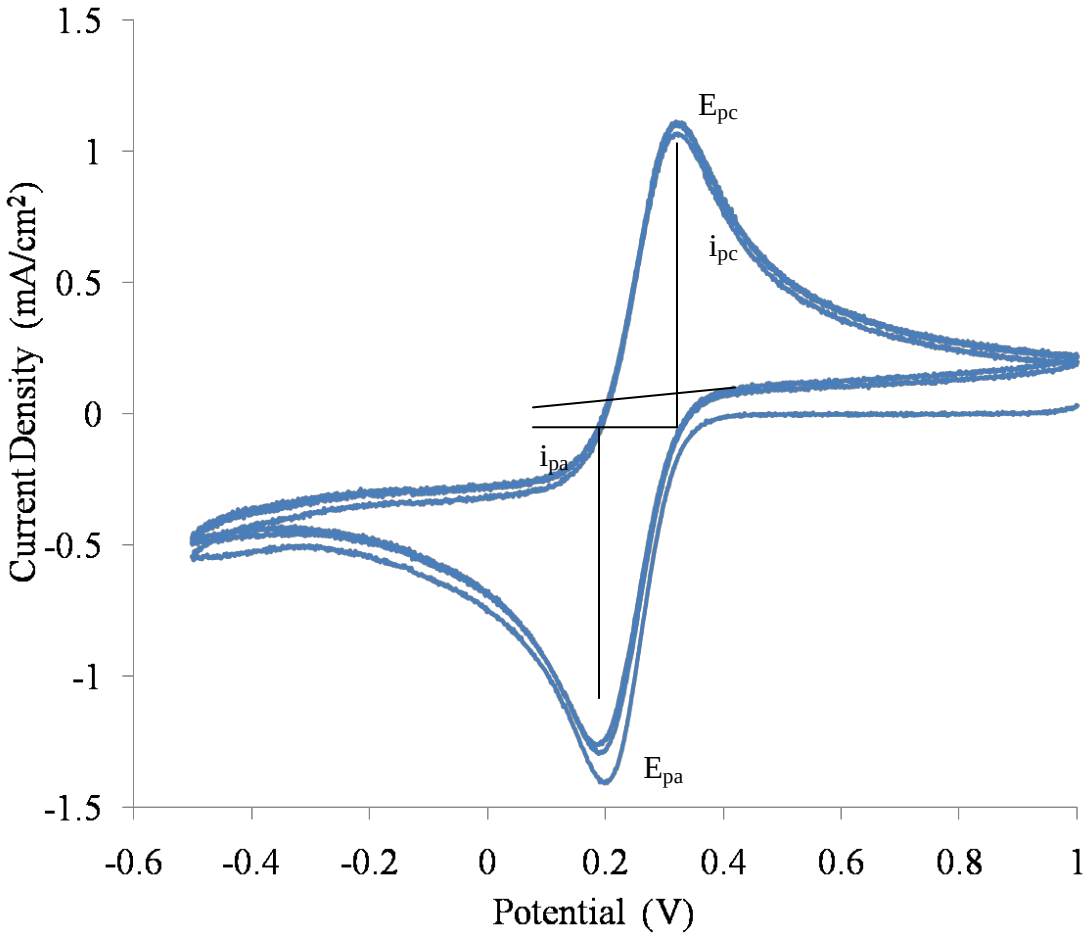


Figure 3.5. CV of 0.5 mM $[Fe(CN)_6]^{3-/4-}$

### 3.4.1. The Electrochemical Cell

The experimental setup for electrochemical measurements takes place in what is referred to as the electrochemical cell. A three – electrode system is usually used and is composed of (1) the working electrode, (2) the auxiliary (counter) electrode, and (3) the reference electrode. The working electrode is where the process to be studied occurs and the auxiliary electrode is needed to complete the circuit in which one electrode emits electrons and the other receives them. The reference electrode acts a reference in measuring the working electrode potential and does not pass any current. The three – electrode system must be arranged so that the impedance measured is primarily from the working electrode and is negligible from the counter electrode. In order to achieve this, the counter electrode must have a significantly larger surface area than the working electrode. With a large surface area, the auxiliary electrode will possess a smaller resistance and a larger capacitance. In practice, auxiliary electrodes are usually platinum mesh. Working electrodes include glassy carbon, gold, and platinum. In the case of the following research the working electrode was either a modified carbon nanotube or nanocrystalline diamond based electrode. Reference electrode materials are typically chosen depending on the analyte measured and for the case of this research is a silver chloride electrode (E = 0.197 V). All of these electrodes are arranged equidistance from one another in a solution with a background electrolyte.

# CHAPTER 4: NANO-CARBON RESULTS AND DISCUSSION

## 4.1. Introduction

The development of a highly sensitive device for the detection of specific biological analytes (i.e. proteins and DNA) remains the foremost challenge in biosensor production. In particular, the advancement of miniaturized DNA and protein sensors remains the subject of intense research today.

*Salmonella* - induced enterocolitis, an inflammation of the colon and small intestine, is the single most common cause of death from food – borne illness in the United States. According to the CDC, the estimated human *Salmonella* infections range from 800,000 to 4 million cases every year, with 800 – 4000 deaths. The cost estimates including lost income and medical costs average from 726 million to 3.7 billion US dollars annually. Rapid detection biosensors will enable the early detection of *S.* Typhimurium from food and water which can prevent food – borne illnesses, losses to the food industry, and reduce the threat of bioterrorism. The most promising materials for realizing next generation nanotechnology are carbon based materials. CNTs and nanocrystalline diamond can amplify DNA or protein recognition and transduction events, which may be used as an ultrasensitive method for electrical biosensing of such molecules.

Lactic acid is an important molecule in several biological processes. Sweat lactate is a function of sweat gland energy metabolism. Because lactate is a product of the sweat gland itself, a decrease in oxygen supply induces a rise in sweat lactate concentration and a decrease in sweat gland activity. For example, pressure applied to soft tissue will cause a rise in sweat lactate concentration with respect to the rest of the body's sweat lactate concentration. The development of pressure sores, or bedsores, has implications on the health of a bedridden individual as well as requirements for health care professionals. Previous studies have evaluated the reduction in oxygen delivery in the tissue of patients with peripheral arterial occlusive disease[111]. This research concluded that lactate in calf sweat is a good indicator in the evaluation of the severity of peripheral occlusive arterial disease and in assessing the efficiency of vasoactive drug treatment. Lactate oxidase is a readily available enzyme that is sensitive only to lactic acid and was applied to boron – doped and nitrogen – incorporated NCD films in order to study their electrochemical activity. Lactic acid was chosen due to its versatility. The blood level of lactic acid exceeding 8 mM can be an indication of several conditions.

Electrochemical impedance spectroscopy (EIS) enables the complex electrical resistance of a system to be analyzed. This analytical method is very sensitive to changes on the electrode surface as well as in the bulk solution and therefore is an appropriate application method in biosensor design[112]. The EIS technique is inherently a label – free detection method, which is especially beneficial due to the fact there is no need to additionally modify the biomolecules of interest with markers, such as fluorescent dyes, enzymes, or other redox labels.

### 4.2. Carbon Nanotube Electrodes

When taking measurements with surface-modified electrodes, such as DNA attached to modified CNT electrodes, redox-active compounds are usually added to the electrolyte solution, resulting in a well-defined charge transfer resistance ($R_{ct}$). If such a redox-active compound is blocked by adding a blocking layer to the electrode, the $R_{ct}$ value will become larger and a more capacitive impedance behavior will be observed. In this section, the use of single-walled carbon nanotubes with a diameter of 20-30 nm as the platform for DNA attachment and hybridization is demonstrated. The carbon nanotubes were modified with carboxyl groups and the oligonucleotide probes with amino groups on the 3' end were covalently bonded to the functionalized nanotubes via *N*-Ethyl-*N*′-(3-dimethylaminopropyl) carbodiimide hydrochloride (EDAC) chemistry. Once hybridization was achieved, electrochemical impedance spectroscopy was used to measure the change in capacitance and charge transfer resistance of the electrode to the redox-active compound $Fe(CN)_6^{-3/-4}$. If the ssDNA probe does not hybridize to its complimentary strand, then the electrode will continue to behave as though it has been blocked and there will not be a noticeable shift in the $R_{ct}$. This is due to the inherent nature that ssDNA is more negatively charged with respect to dsDNA and will consequently repel more of the redox-active compound. In this study, we chose to use *Salmonella* specific probes, because Salmonella infections remain one of the most common foodborne illnesses in the United States and perhaps even globally[113]. This method of genosensing is a quick, facile approach to detecting DNA without the use of additional labels.

### 4.2.1. Materials and Methods

Single walled carbon nanotubes (SWNTs) were obtained from Cheap Tubes, USA. The electrolyte used in all electrochemical measurements was 0.5 m$MK_3Fe(CN)_6$ in 0.5 M KCl (Sigma-Aldrich). DNA probe attachment took place in an acetate buffer of 0.3 M sodium acetate (Sigma-Aldrich) and 0.3 M acetic acid (purity , Fisher Scientific). DNA hybridization took place in a 0.1 M phosphate buffer solution (PBS), which was made in deionized water with $K_2HPO_4$ (purity 98%) and $KH_2PO_4$ (purity 99%), both from Sigma-Aldrich. The label-free impedance based detection method for DNA hybridization is illustrated in Figure 4.1.

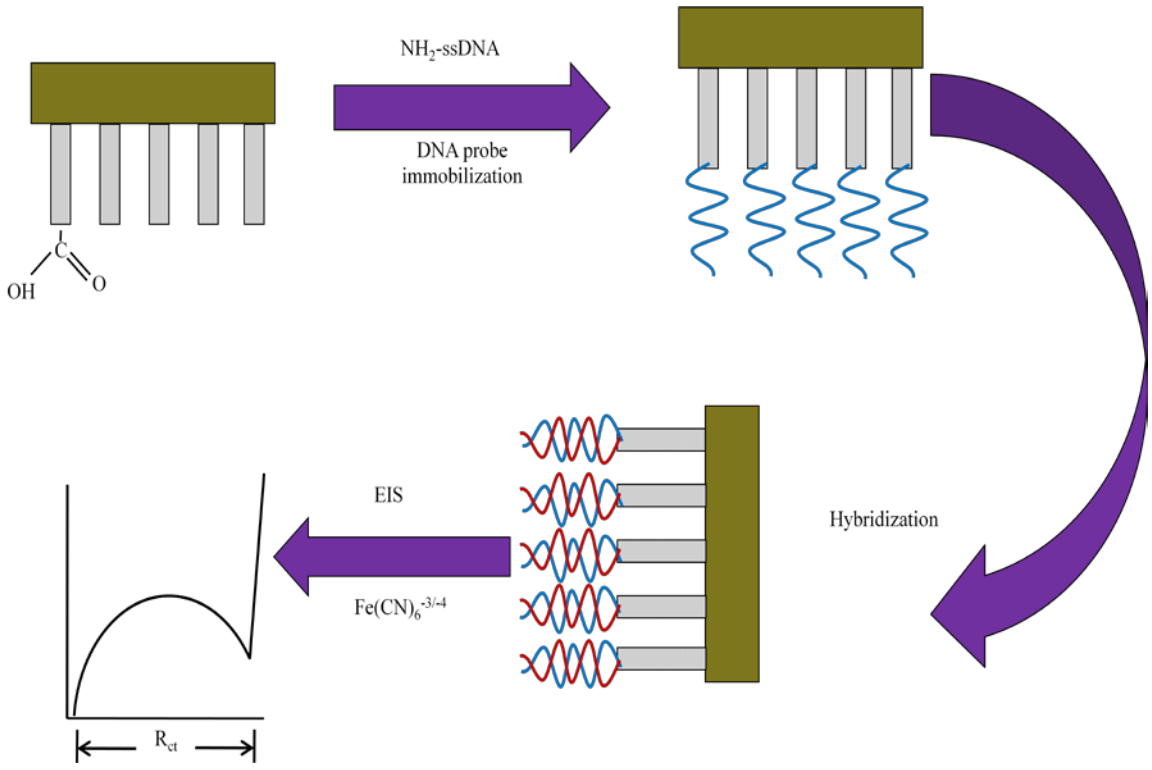


Figure 4.1. Schematic of CNT and DNA attachment chemistry process and DNA hybridization measurement in 5.0 mM $K_3Fe(CN)_6$

Single walled carbon nanotubes were chemically shortened and oxidized in a solution of 3:1 sulfuric and nitric acids under ultrasonication for 8 hrs. This treatment causes carboxylic acid groups to form on the ends of the CNTs. The functionalized nanotubes were then filtered under vacuum and rinsed to clear any excess acid (Figure 4.2.). The CNTs were collected from the filter paper and sonicated in dimethylformamide (DMF) for an additional 4 hrs. The new CNT/DMF solution had a concentration of approximately 0.1 g CNT in 3.0 mL DMF. A 3-mm diameter glassy carbon electrode was polished with 1.0 μm alpha alumina powder, rinsed with deionized water and dried in a $N_2$ stream. The same electrode was polished again with 0.3 μm alpha alumina powder, rinsed, and dried. A certain amount of the functionalized CNT suspension (1 - 20 μl) was applied onto the surface of the polished glassy carbon electrode and allowed to dry overnight at room temperature.

Electrochemical impedance and cyclic voltammetry were measured on the modified glassy carbon electrode with the carboxylated carbon nanotubes (CNT-COOH) in 0.5 m$MK_3Fe(CN)_6$ in 0.5 M KCl before and after modification. Next, the $NH_2$-ssDNA probe was attached to the CNT-COOH electrode using *N*-Ethyl-*N*′-(3-dimethylaminopropyl) carbodiimide hydrochloride (EDAC) chemistry. The electrode was incubated in the $NH_2$-ssDNA probe solution for 2 hours at room temperature under gentle agitation. The DNA hybridization took place in complimentary probe phosphate buffer solution for 20 min. at room temperature under gentle stirring. Nyquist plots and cyclic voltammograms were obtained before and after each modification step.

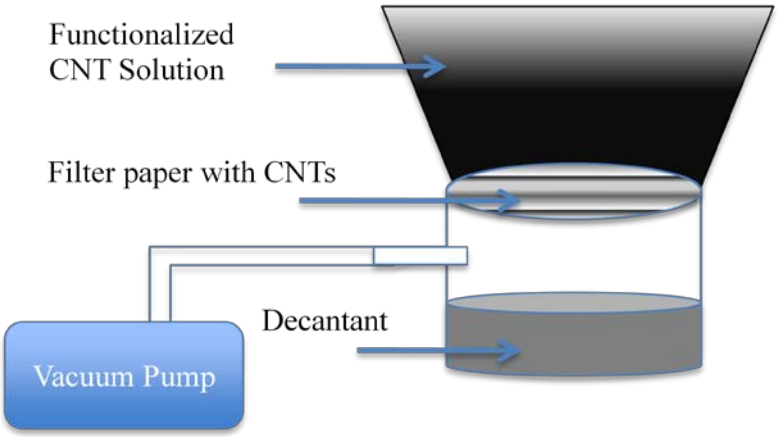


Figure 4.2. CNT functionalization setup

The *Salmonella* specific probe based on the *wecE* gene was selected from a previous report on detection of *Salmonella* from water[114]. The ssDNA probe, complimentary and mismatched ssDNA were purchased from Life Technologies Corporation (Carlsbad, CA). The sequences of the various analytes are provided in Table 4.1.

Table 4.1. ssDNA probe and complementary strand sequence information

| Sequence | Function |
|---|---|
| 5’ TACCGCAGCTAATTGACGTTAC 3’ NH | *Salmonella* specific ssDNA probe |
| 5’ GTAACGTCAATTAGCTGCGGTA 3’ | Complementary ssDNA strand |
| 5’ GTAACGTCAATTAGCTGCGGTG 3’ | One base-pair mismatched ssDNA strand |

Table 4.1. (Continued)

| | |
|---|---|
| 5’<br>TAGGGAACGATCGGTCACATCGG<br>3’ | Unrelated ssDNA strand |

Micro Raman spectroscopy was conducted on the CNT electrode with a *Renishaw* 1000 Raman spectrometer using an argon laser (514.5 nm) at a laser power of 24.8 mW and a spot size of 1 μm. The laser was introduced to the sample through a 50X objective lens. The Raman scattering was collected with an exposure time of 10 s to the sample.

Cyclic voltammetry (CV) and electrochemical impedance spectroscopy (EIS) were performed with a Radiometer Analytical Voltalab 40 potentiostat and the data was analyzed with the corresponding Voltmaster4 software. The standard three-electrode system consisted of a modified glassy carbon electrode with a surface area of 7.07 $mm^2$, an Ag/AgCl (3M KCl) reference electrode, and a platinum wire (CH Instruments) as the counter electrode. The electrochemical measurements were carried out in a 10-mL cell at room temperature. The cyclic voltammetry experiments had a potential scan rate of 100 mV $s^{-1}$, step height of 1.0 mV and applied a potential from +1 V to -0.5 V. The electrochemical impedance experiments applied a frequency range of 50 kHz – 100 mHz with an AC sine wave amplitude of 10 mV.

### 4.2.2. Discussion

Raman scattering is one of the most useful and powerful techniques available to characterize carbon nanotube samples. For carbon nanotubes, the G mode corresponds to

the stretching mode in the graphite plane and is centered around 1580 $cm^{-1}$. As seen in Figure 4.3., the modified electrode shows the G mode at about 1590 $cm^{-1}$. The D mode (the disorder band) is located between 1330 – 1360 $cm^{-1}$. While this band is expected to appear in multi-wall carbon nanotubes, it is usually attributed to defects in the tubes when observed in single-wall tube samples. Figure 4.3. shows that this band appears at 1351 $cm^{-1}$ for the modified sample and the poor intensity of this peak can be interpreted as an indication of the high purity of the functionalized SWNTs. The radial breathing mode is unique to single walled carbon nanotubes and is directly related to the diameter of the tube. This mode usually appears around 200 $cm^{-1}$. The Raman peaks centered at 174 $cm^{-1}$ and 1590 $cm^{-1}$ on the treated sample indicates that surface condensation of carboxylated carbon nanotubes.

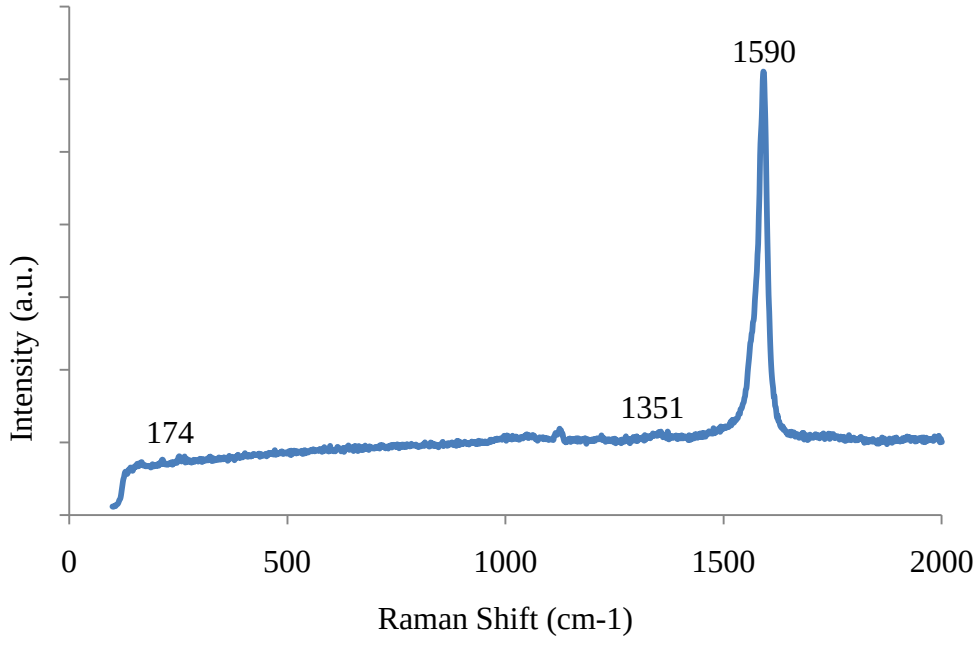


Figure 4.3. Raman spectra of CNT electrode

Electrochemical characterization relating to the performance of the modified glassy carbon electrode was evaluated. The effect of the amount of SWNTs placed on the bare, polished glassy carbon electrode was studied in a solution of 0.5 mM $K_3Fe(CN)_6$ in a supporting electrolyte of 0.5 M KCl. Cyclic voltammograms were recorded with the systematic addition of more SWNTs to the electrode surface and a definite increase in the reduction and oxidation peaks appeared at approximately 0.3 and 0.2 V, respectively. In comparison to the performance of the bare glassy carbon electrode, the modified SWNTs – COOH/GC electrode with a higher concentration of nanotubes displayed a significant increase in current density. This phenomenon verifies that the SWNTs – COOH not only enhance the electrode response, but also serve as an active binding site of the oligonucleotide probes by providing a larger effective electrode surface area. Therefore, it can be concluded that the carbon nanotubes extend outwards on the glassy carbon electrode, providing a rich matrix of active area for the ssDNA to bind to and assist in direct electron transfer. The important role that the modified nanotubes play can be seen by the increase in the oxidation peak with respect to the gradual increase of nanotubes on the glassy carbon surface. Figure 4.4. shows the results of increasing the amount of SWNTs – COOH in the DMF solution onto the bare, polished glassy carbon surface. There is a nearly linear increase in current density while increasing the amount of SWNT – COOH/DMF solution from 5 µL to 15 µL on the glassy carbon surface. It is noted that Figure 4.5. demonstrates that the current density levels off with either extremely low levels of SWNTs (1 µL) and extremely high levels of SWNTS (20 µL).

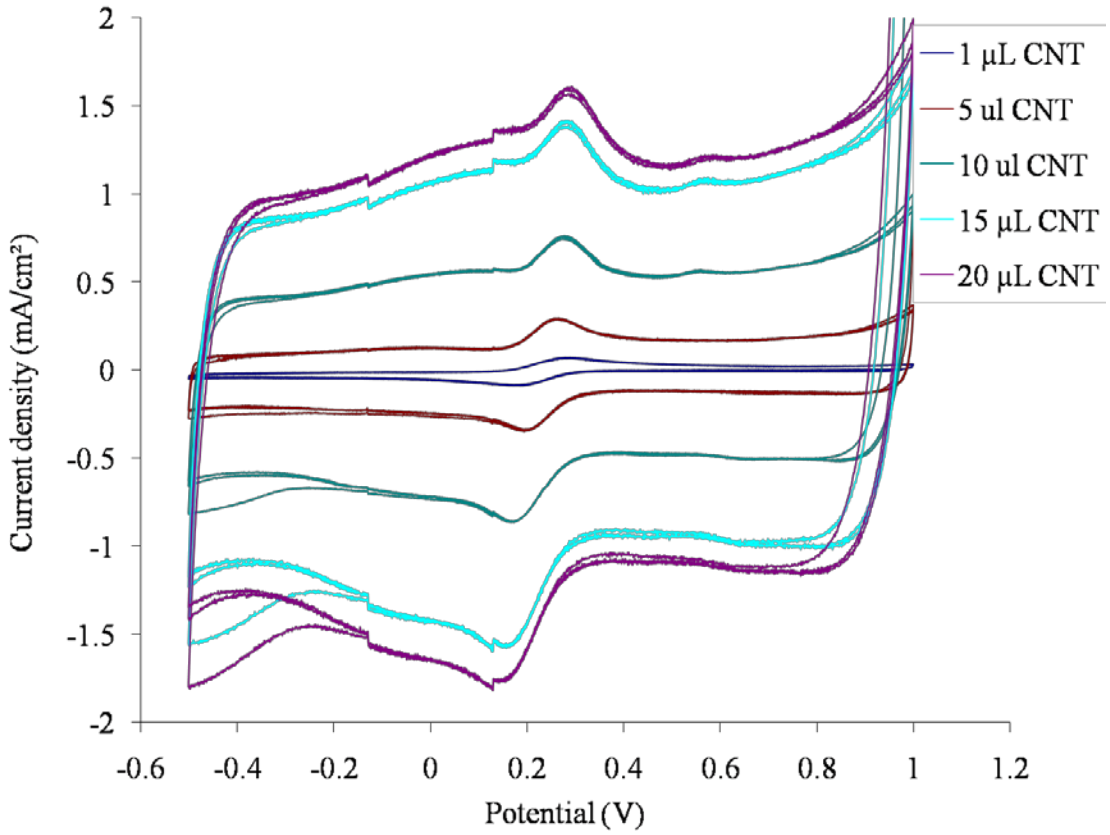


Figure 4.4. Cyclic voltammograms in 0.5 mM $K_3Fe(CN)_6$ in 0.5 M KCl aqueous solution vs. Ag/AgCl for 1.0 µL, 5.0 µL, 10 µL, 15 µL and 20 µL SWNT – COOH deposited on a polished glassy carbon electrode with a scan rate of 100 mV $s^{-1}$ applied from 1.0 to -0.5 V.

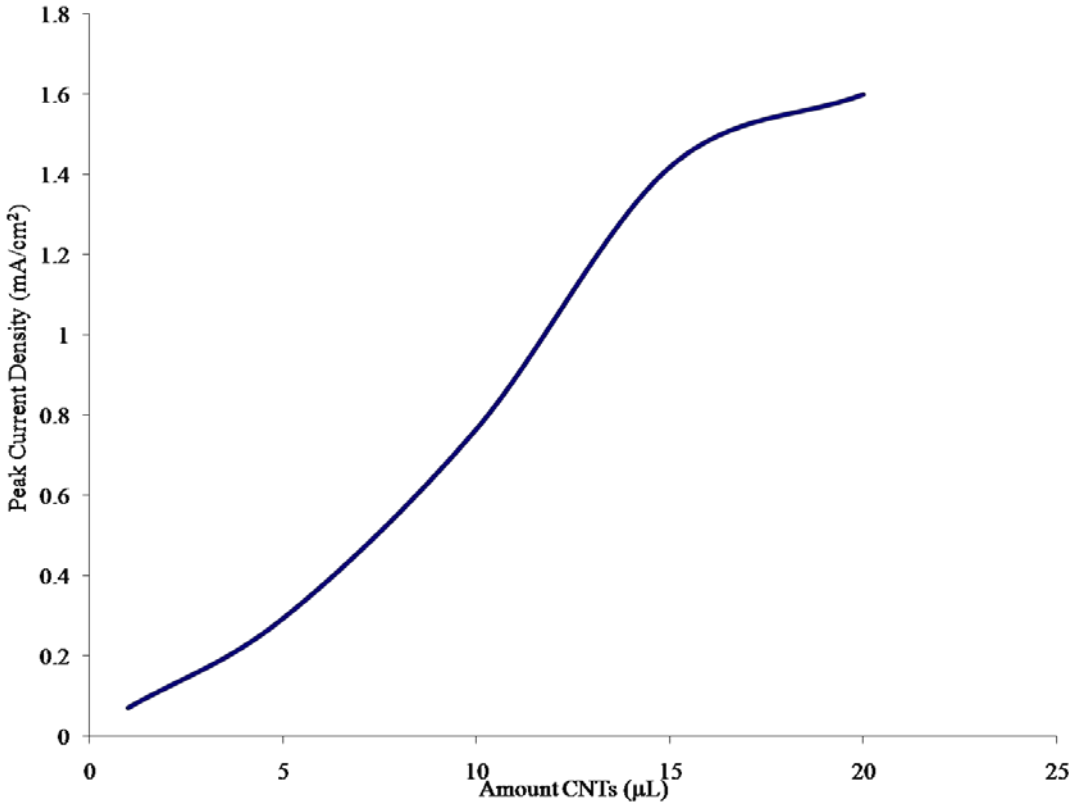


Figure 4.5. Current density profile with an increase in CNTs to electrode surface

Figure 4.6. displays typical cyclic voltammograms of the (a) bare, polished glassy carbon, (b) SWNTs – COOH/GC, and (c) ssDNA – SWNTs – COOH/GC electrodes. All voltammograms were cycled three times in order to verify the stability of the signal. The anodic to cathodic peak current ratio approaches unity for both bare GC and SWNT – COOH/GC electrodes, indicating a reversible reaction for $Fe(CN)_6^{3-}$. There is an increase in oxidation peaks from the bare electrode to the nanotube electrode, as discussed above, and then an oxidation peak decrease is visible with the binding of the ssDNA probe to the functionalized carbon nanotubes. The decreased current response can be attributed to the negatively charged ssDNA molecules, which will dampen the redox reaction.

A Randles equivalent circuit may be modeled for the modified CNT electrode in contact with the redox compound. This circuit contains the solution resistance $R_s$, the charge transfer resistance $R_{ct}$, the double layer capacitance $C_{dl}$ and the Warburg impedance *W*. However, for analytical purposes the Warburg impedance can be neglected in the overall equivalent circuit by choosing a frequency range where no 45° line is observed in the Nyquist plot. The determination of the $R_{ct}$ was used as the impedimetric detection method of analyte binding. This approach was chosen because it is of particular interest when the conductivity of the recognition layer changes due to a binding event such as DNA hybridization.

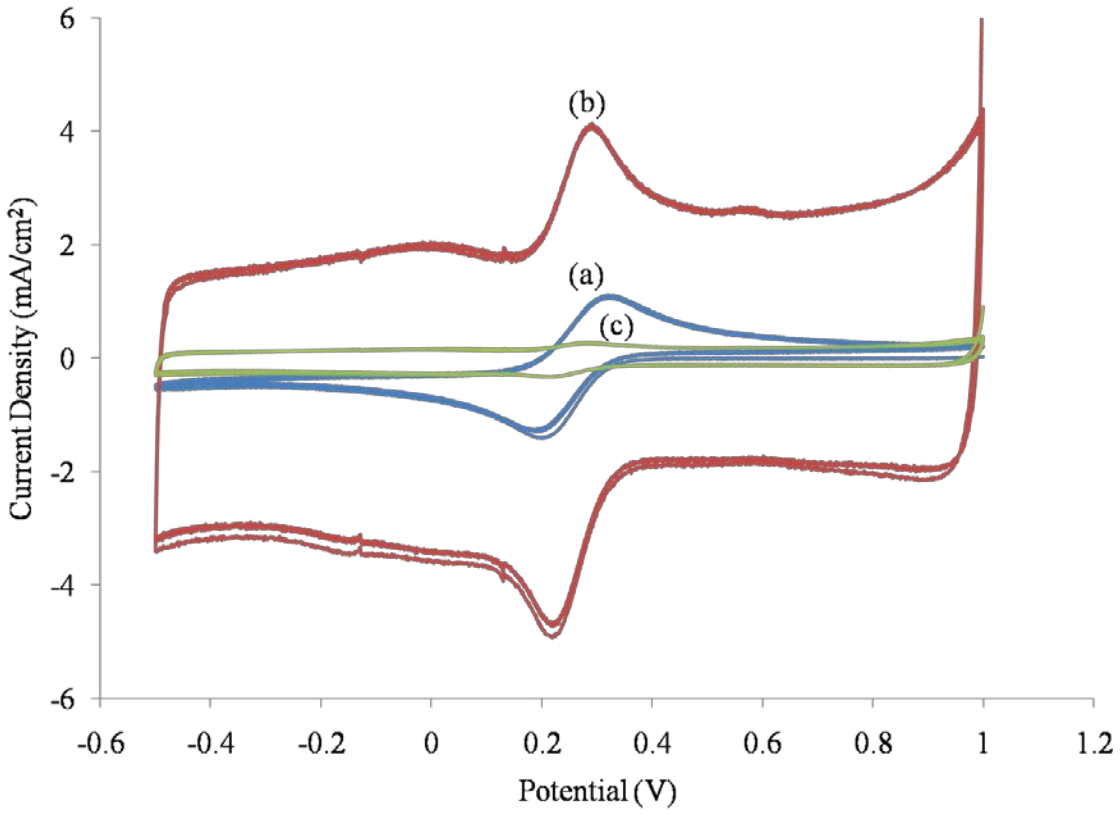


Figure 4.6. Cyclic voltammograms in 0.5 mM $K_3Fe(CN)_6$ in 0.5 M KCl aqueous solution vs. Ag/AgCl for (a) polished, bare glassy carbon electrode (GCE), (b) SWNT – COOH modified GCE and (c) $NH_2$-ssDNA probe bound to SWNT – COOH modified GCE with a scan rate of 100 mV $s^{-1}$ applied from 1.0 to -0.5 V

The electrochemical impedance of the functionalized electrode was studied in order to determine the suitability of such an electrode for DNA sensing applications. The Nyquist plots (Figure 4.7) were obtained prior to binding of the $NH_2$-ssDNA probe onto the CNT matrix of the glassy carbon electrode for use as reference. It is clearly visible that the bare polished glassy carbon electrode exhibits a large charge transfer resistance of about 95.4 $\Omega \cdot cm^2$. Upon the addition of the functionalized SWNTs – COOH on the glassy carbon surface, the diameter of the Nyquist plot's semicircle drastically reduced, which equates to a reduction in the $R_{ct.}$ Next, the $NH_2$-ssDNA probe was attached to the

CNT matrix. The addition of the ssDNA shows an increase in $R_{ct}$ due to the fact that ssDNA has negative charges repelling the $Fe(CN)_6^{-3/-4}$, which is represented in the Nyquist semicircle diameter becoming larger than that of the nanotube modified electrode. After hybridization in different concentrations of complimentary DNA, the semicircle diameter decreased in small increments. However, the charge transfer resistance never decreased to the same amount as the SWNT – COOH/GC electrode. It appears that the double-stranded DNA (dsDNA) has the ability to transfer electrons better than ssDNA. This method of detection is very sensitive and is able to sense complementary target DNA concentration at $10 \times 10^{-10}$ mol $L^{-1}$.

The modified CNT – COOH glassy carbon electrode was tested for efficiently specificity to the target DNA sequence as well as genosensor sensitivity. The electrode was prepared by attaching the ssDNA probe onto the modified electrode surface as before and exposing it to different strands of DNA, each with a concentration of $1 \times 10^{-6}$ mol $L^{-1}$. The signals of a completely unmatched sequence and a one-base mismatched sequence were compared to that of the hybridized complimentary sequence. The Bode plot shown in Figure 4.8 shows that an appreciable change in *Z* was only observed with the hybridized complementary target DNA sequence. In fact, the change in impedance for the complementary target DNA is similar to that of the impedance of the CNT – COOH/GC electrode. Very little change is shown in the signals of the ssDNA probe with the unmatched and one-base mismatched DNA. Therefore, it can be concluded from the data that this type of modified carbon nanotube/glassy carbon electrode is capable of detecting target DNA strands with acceptable sensitivity and selectivity.

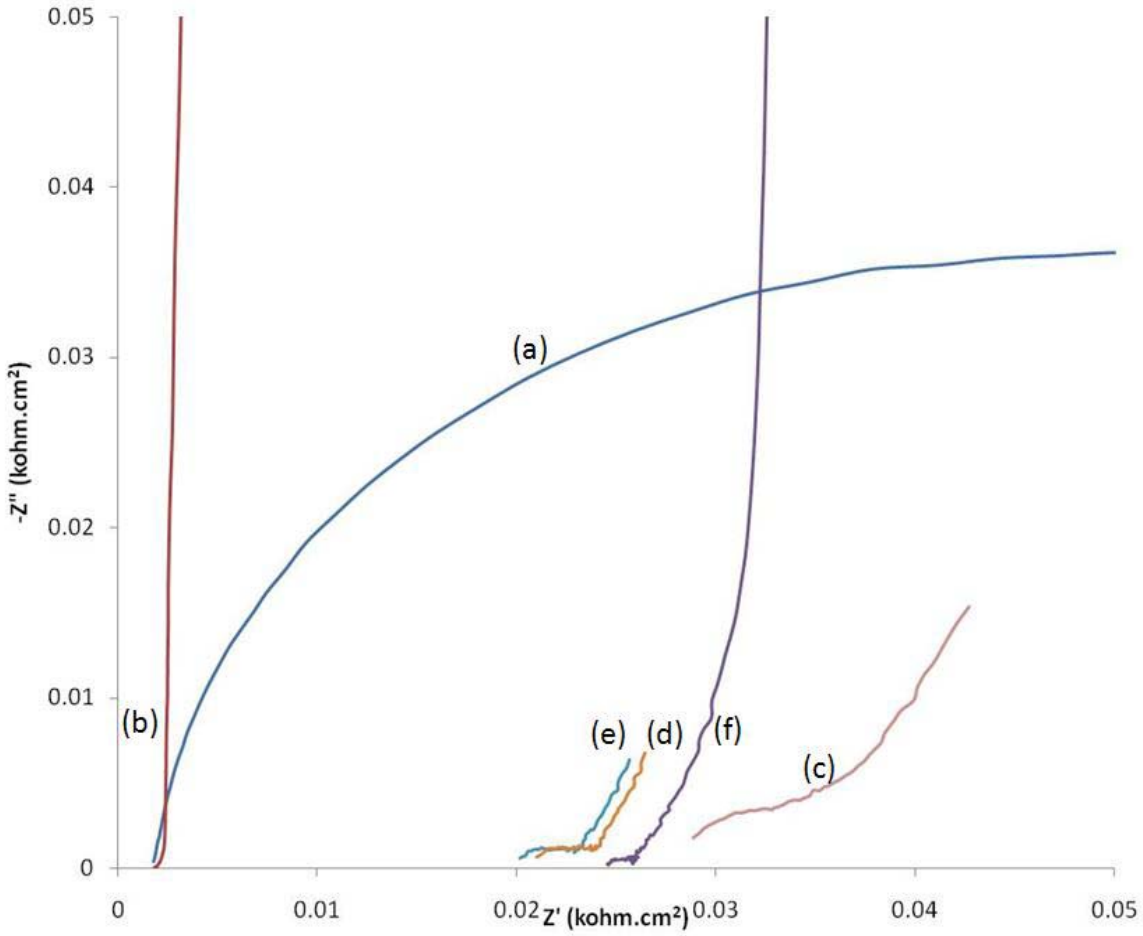


Figure 4.7. Nyquist plot of (a) GCE, (b) SWNT – COOH modified GCE, (c) ssDNA/SWNT – COOH GCE, and (d –f) increasing concentrations of complementary DNA

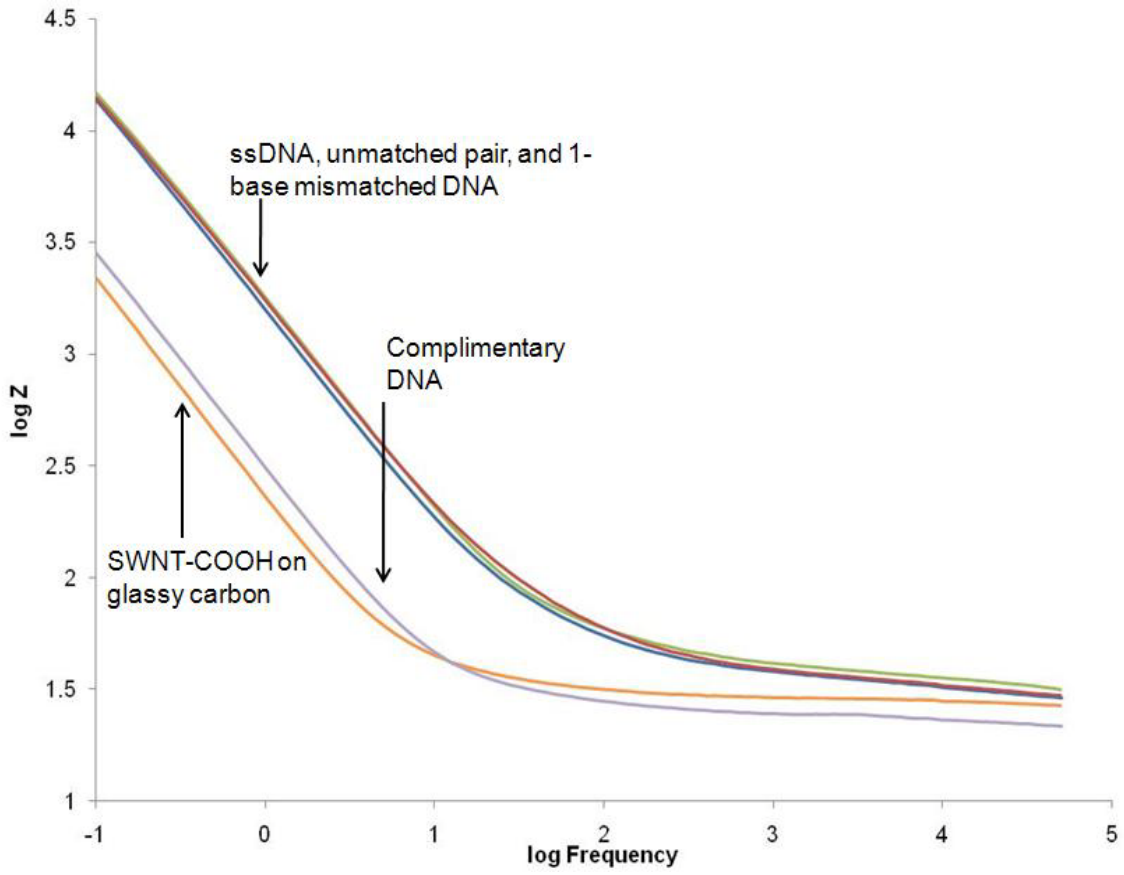


Figure 4.8. Bode plot of SWNT – COOH/GC electrode after ssDNA probe attachment and exposure to complementary DNA sequence as well as unmatched and mismatched DNA sequences

### 4.3. Nanocrystalline Diamond Electrodes

Conductive diamond films possess several unique properties such as a large electrochemical potential window, chemical robustness, high hardness, high corrosion resistance as well as excellent biocompatibility[115], which make it an ideal platform as a biosensing electrode. However, nanocrystalline diamond (NCD) biosensor applications require precise control over the film's surface properties, such as wettability and proper

surface chemistry. There are several practical benefits of using nanocrystalline rather than microcrystalline diamond thin-films in electrochemistry, including the ability to deposit continuous films at nanometer range, easier coating of substrates with irregular geometries and the unique electrochemical behavior which results from the NCD film's different morphology and electronic properties compared to the microcrystalline films. Several methods have been studied to control the biological and chemical functionalization of NCD, such as photochemical modification[116], covalent functionalization of proteins on hydrogenated diamond surfaces[117], as well as electrochemical reduction[118].

### 4.3.1. Growth of Boron Doped Nanocrystalline Diamond

Boron doped diamond films on silicon are deposited with a hot filament CVD deposition reactor ($sp^3$ Diamond Technologies, Inc. Model 650); capable of depositing on one 300mm or nine 100 mm wafers in the large industrial chamber with wafer film thickness uniformity better than ± 5% and wafer-to-wafer uniformity of typically ± 3% for a 9 wafers run. The silicon wafers are seeded prior to deposition in an ultrasonically agitated solution containing 4-50 nm ultra dispersed diamond (UDD) detonation-synthesized nanopowder. The high seed density ($>5x10^{10}/cm^2$) allows these films to be characterized as pinhole free with uniform grain morphology. The grain size of the diamond is varied from large grain microcrystalline to small grain nanocrystalline by controlling the $CH_4$ and pressure set points to the required process window. Boron is introduced into the system as the trimethylborate (TMB) gas to produce p-type doping. Increasing the TMB flow during deposition allows more boron to be incorporated into the

diamond film to reduce the sheet resistance. Tungsten wires were heated to ~2200 °C to activate the reaction gas- a mixture of hydrogen and methane. Film parameters with growth conditions of the boron-doped NCD is shown in Table 4.2. and a typical image of the film is shown in Figure 4.9 with the atomic force microscopy surface analysis shown in Figure 4.10.

Table 4.2. Growth conditions for boron-doped NCD films

| PROPERTY | nm BDD |
|---|---|
| Sheet Resistance | 1.0 KOhm/sq" |
| Resistivity | 0.32 Ohm.cm |
| Watt Density | 9.6 $W/cm^2$ |
| $\%CH_4$ | 2.2% |
| %TMB | 0.007% |
| Wire temp | $2255^0C$ |

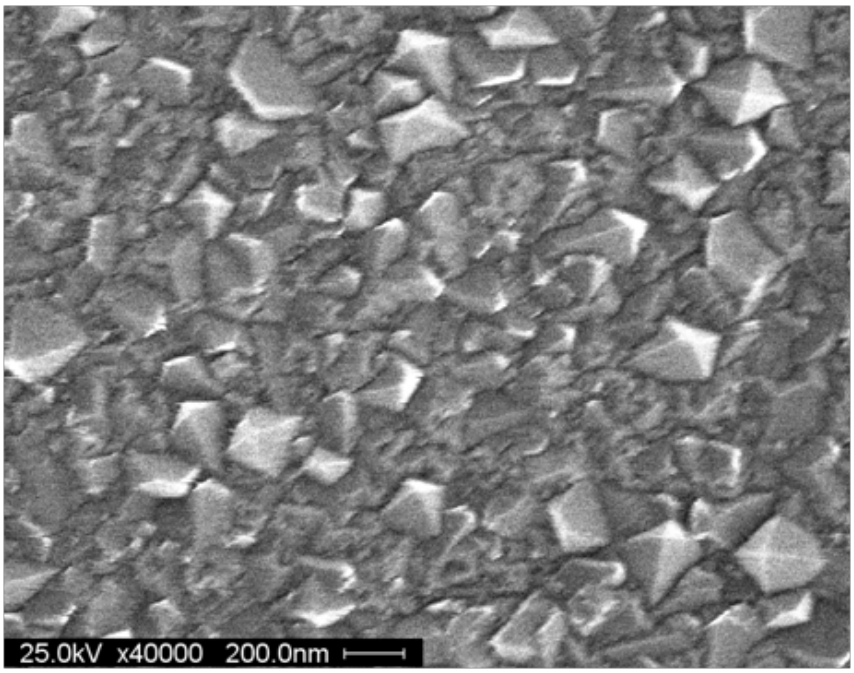


Figure 4.9. SEM image of nanocrystalline BDD

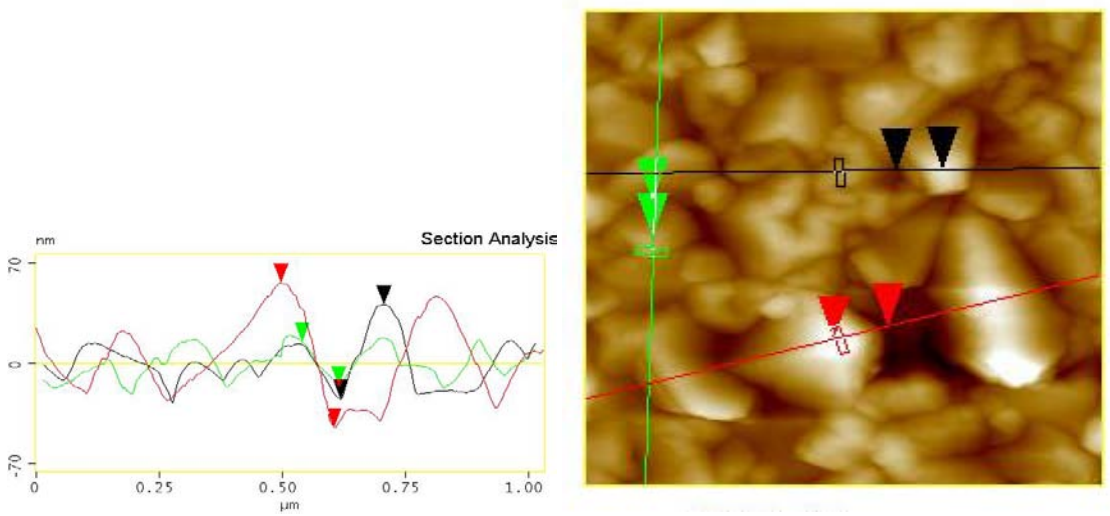


Figure 4.10. AFM section analysis of nanocrystalline BDD

### 4.3.2. Growth of Nitrogen Incorporated Nanocrystalline Diamond

Figure 4.11. shows the CVD reactor used for growth of nitrogen incorporated NCD. It has a 6 kW microwave head that can produce plasma up to 100 mm on wafers. The substrate holder can heat samples up to 800 °C. For incorporation with nitrogen, the process recipes are changed to make the films conductive. The grain size of the diamond films can be drastically decreased by changing the gas chemistry during growth. Also, when nitrogen is introduced, the growth rate increases which in turn affects the growth morphology of the conductive NCD films. Before the deposition, 0 to 0.5 µm diamond powders were used to polish the sample surface to increase the nucleation rate and the samples were ultrasonically cleaned in methanol for 10 min. The nitrogen – incorporated NCD films were grown using $CH_4/Ar/N_2$ gas chemistry for 3 hr. Table 4.3. summarizes the growth conditions for these films. Figure 4.12. shows a typical nitrogen – incorporated NCD sample with "cauliflower" – like grains. From Figure 4.13., surface roughness information about the samples were obtained. The mean roughness was about 14.5 nm for a 10 µm ×10 µm scan size. The conductivity of the diamond films measured by four-point-probe method at room temperature was found to be ~ 100 $ohm.cm^{-1}$.

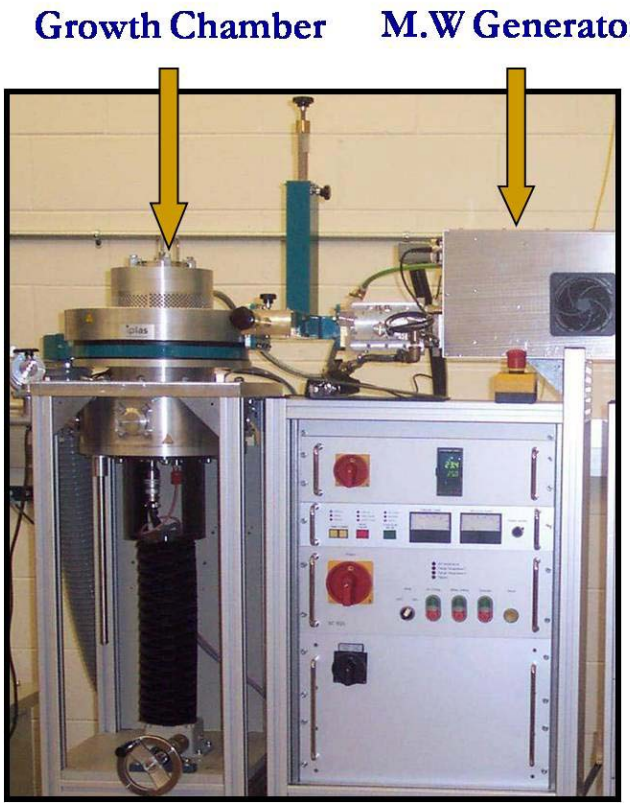


Figure 4.11. *Cyrannus I Iplas* MPCVD system for NCD growth

Table 4.3. Growth conditions for nitrogen – incorporated NCD films

| PROPERTY | nm NCD |
|---|---|
| Gas Flow | 200 sccm |
| Power | 800 W |
| Pressure | 100 Torr |
| $\%CH_4$ | 1% |

Table 4.3. (Continued)

| | |
|---|---|
| %Ar | 79% |
| $\%N_2$ | 20% |
| Substrate Temp. | 750 °C |

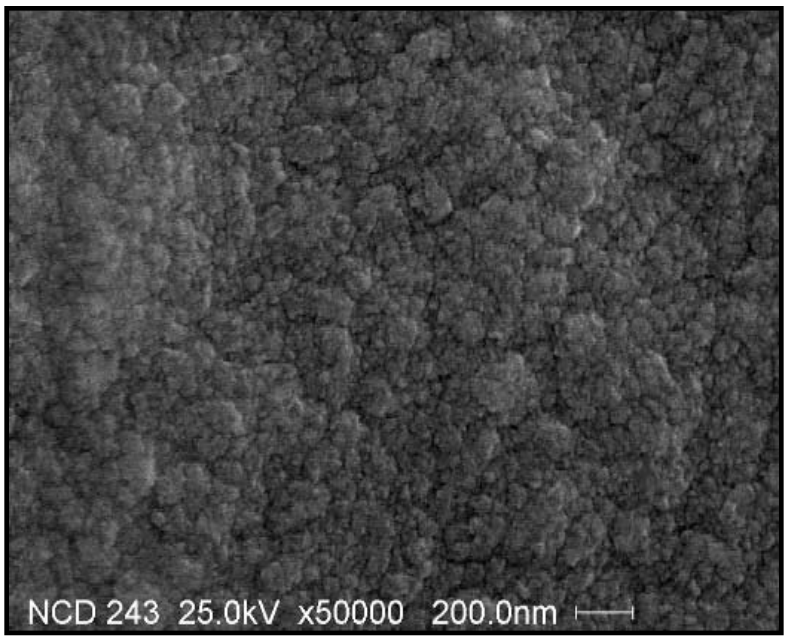


Figure 4.12. SEM of nitrogen – incorporated NCD

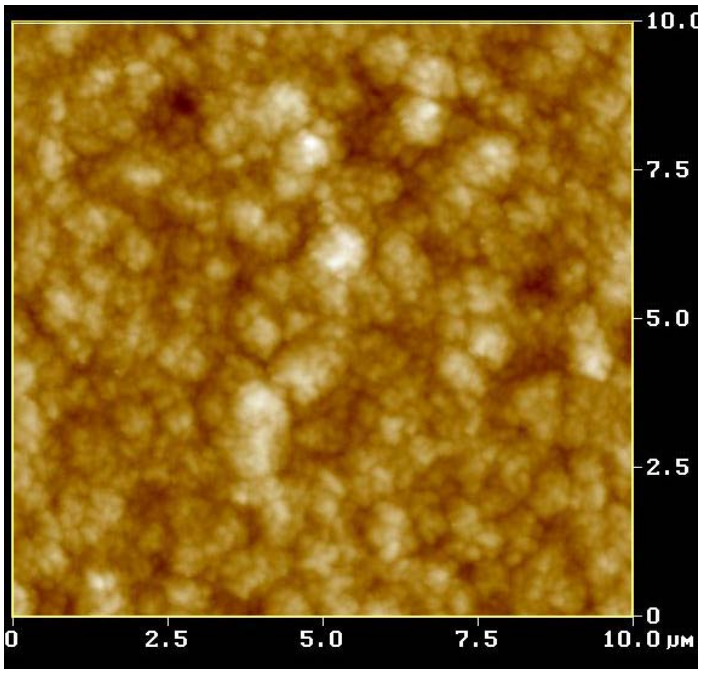


Figure 4.13. AFM roughness analysis of nitrogen – incorporated NCD

### 4.3.3. Hydrogenation of Nanocrystalline Diamond

Diamond hydrogenation was included as a step in the surface modification of all samples, regardless of the target analyte. Hydrogenation serves as a platform for carboxylic functionalization and eventually, enzyme or DNA attachment. For all samples, diamond hydrogenation took place in a hot filament chemical vapor deposition (HFCVD) system with a flow rate of 90 sccm hydrogen gas at a temperature of about 1200 °C, as shown in Figure 4.14. The Raman spectra shown for BDD exposure to hydrogen plasma at different times is shown in Figure 4.15. After hydrogenation, the sp2 peak decreases because hydrogen etches the sp2 graphite bonds on the surface, resulting in a film that is highly conductive and hydrophobic. The most desirable surface is the one that has a low sp2 graphite peak while the sp3 peak has high intensity and these

conditions are met when the hydrogen treatment is performed for 30 minutes on the BDD.

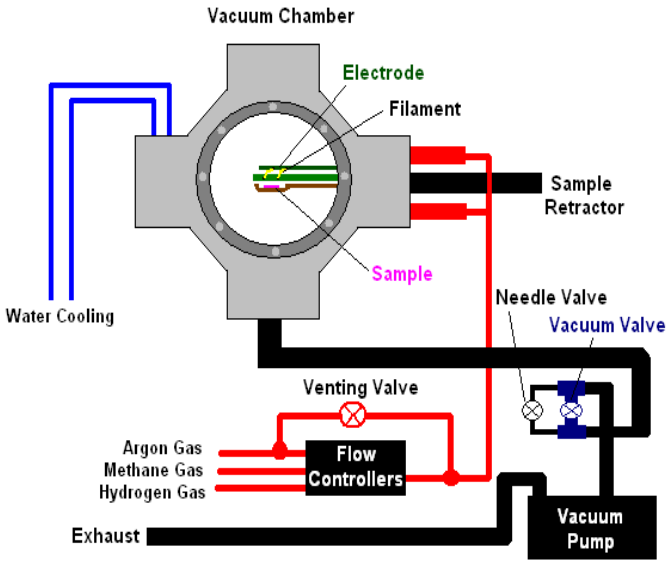


Figure 4.14. Schematic of HFCVD used for hydrogen plasma treatment of nanocrystalline diamond samples

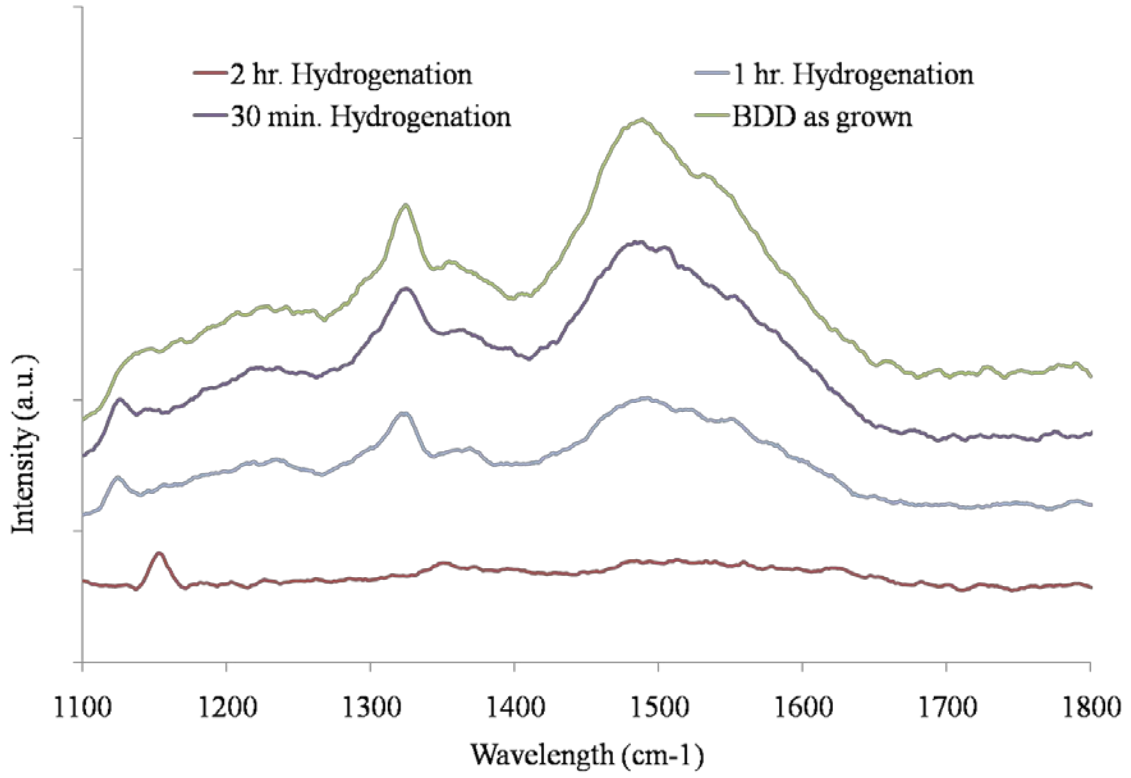


Figure 4.15. Raman spectra after hydrogen treatment of BDD films

The nanocrystalline NCD shows a broad G band centered around 1500 $cm^{-1}$. The G bands are usually associated with disordered $sp^2$ carbon[119]. The diamond band occurs at about 1330 $cm^{-1}$.

### 4.3.4. Materials and Methods for DNA Sensing

Carboxylic acid dimers (-COOH) had to be attached to the hydrogenated BDD in order to transition the film from hydrophobic back to hydrophilic as well as to use as a platform for ssDNA attachment. The electrodes were immersed in a 0.3 M acetic acid solution and 25 cycles of cyclic voltammetry were conducted under the potential range of -200 to 800 mV. The newly modified electrodes were then subjected to $NH_2$-ssDNA. A

mixture of acetate buffer (0.3 M sodium acetate and 0.3 M acetic acid), EDAC and $NH_2$-ssDNA was deposited on top of the nano BDD and was left to dry in a refrigerator at a temperature of less than 20 °C for two days. The EDAC aids in the chemical reaction between the carboxyl group on the diamond surface and the $NH_2$-ssDNA. After the ssDNA deposition, a mixture of phosphate buffer solution and FITC-labeled complementary *Salmonella* DNA (compDNA) was deposited on the surface. The electrode was left in the refrigerator for two days for the compDNA to bind to the $NH_2$-ssDNA attached to the diamond surface. Figure 4.16. shows a schematic of the electrode modification process.

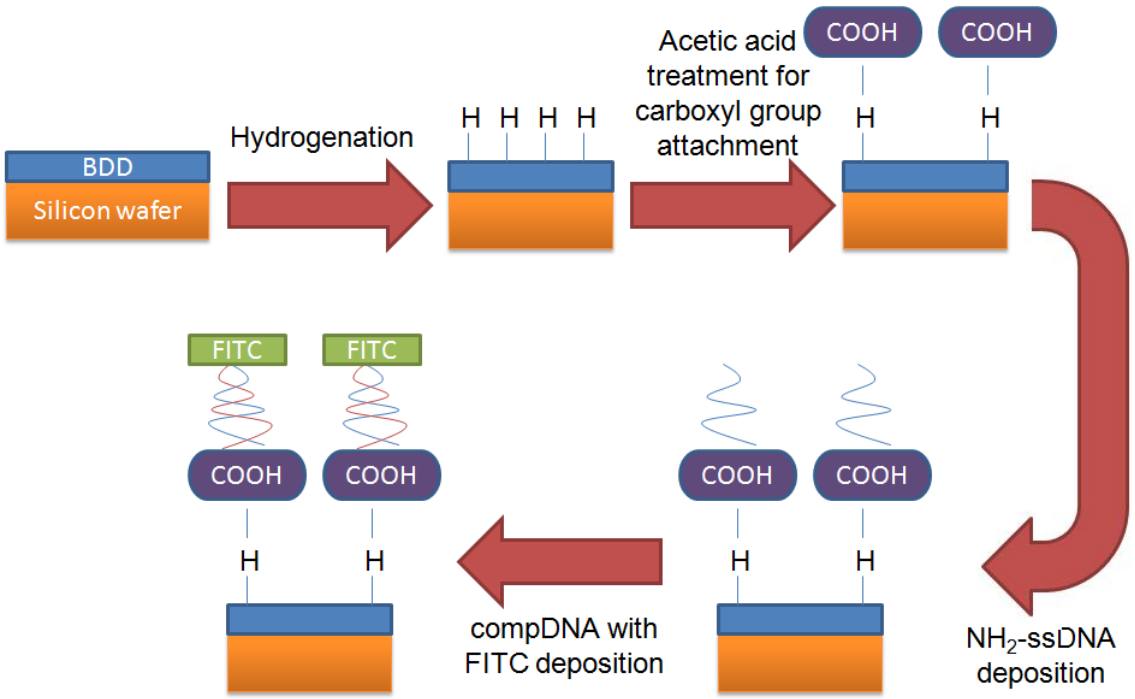


Figure 4.16. Schematic of modification of boron – doped NCD films for DNA detection

Electrochemical measurements, were performed using a Radiometer Analytical Voltalab 40 potentiostat. All electrochemistry was performed in a standard three-

electrode system. The modified boron-doped NCD acted as the working electrode, an Ag/AgCl (3M KCl) acted as the reference electrode, and a Pt mesh acted as the auxiliary electrode. The impedance spectra were taken over a wide frequency range from 1 MHz to 50 mHz, with a 10 mV excitation signal superimposed onto the electrochemical system.

### 4.3.5. DNA Sensor Discussion

Cyclic voltammograms were taken in between surface modifications of the boron – doped NCD electrodes to analyze electrochemical activity at the diamond surface. Interestingly, while hydrogen treatment of NCD increases the conductivity of the diamond, the electrochemical activity actually decreases. Surface hydrogen applied from hydrogen plasma, in which the hydrogen atoms bond to terminal carbon atoms, do not desorb quickly. The physiochemical properties of boron – doped NCD are very influential over the electrode kinetics. Figure 4.17. shows CVs with and without surface hydrogenation in a phosphate buffer solution. Clearly, the background current for the as-grown, oxygen – terminated BDD electrode is much higher than the hydrogen – terminated electrode. The oxygen termination increases the hydrophilic characteristics of the surface and it is this characteristic that causes an increase in current density by an order of magnitude.

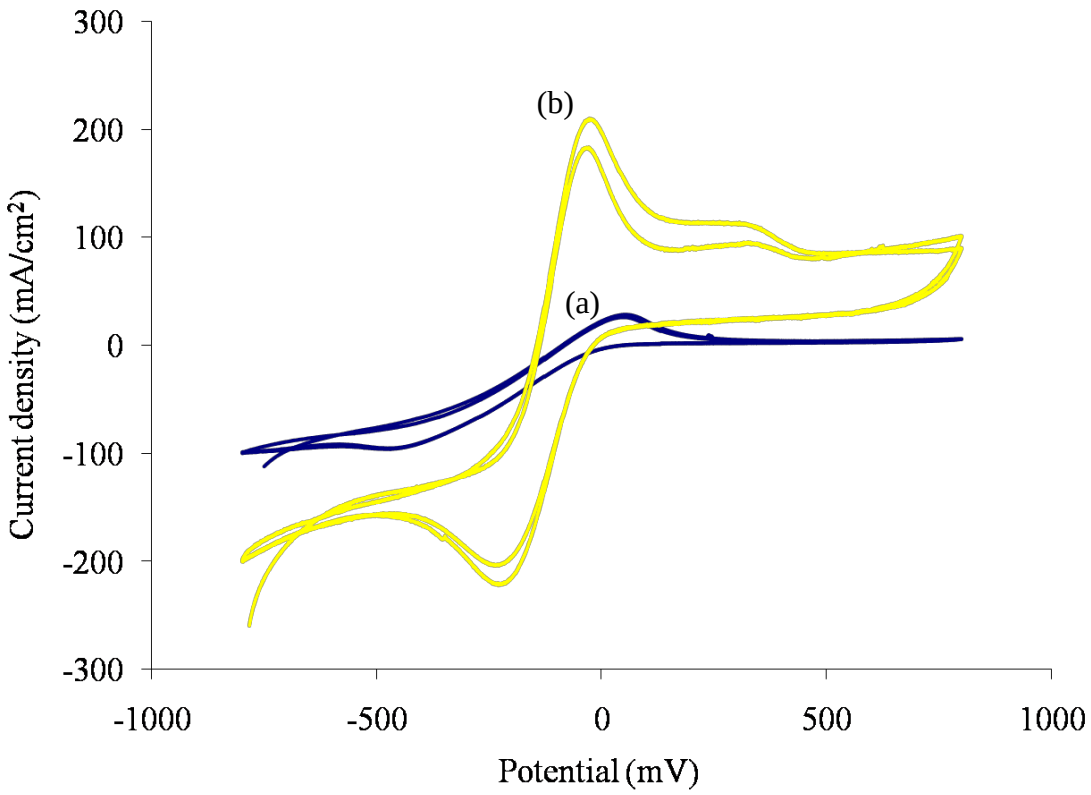


Figure 4.17. CVs of BDD surface (a) with hydrogen and (b) without hydrogen treatment

Mass transport issues need to be taken into account when using electrochemical techniques to characterize the boron – doped NCD sample with ssDNA attachment. As mentioned above, the transfer of electrons to and from the diamond surface is highly dependent on the termination of atoms at the surface. Figure 4.18. shows cyclic voltammograms of the prepared modified BDD electrode prior to deposition of $NH_2$-ssDNA and immediately after at different scan rates in $Fe(CN)_6^{-3/-4}$. Note that the higher scan rates produce highly asymmetric, disordered CVs, while the lower scan rates show the CV becoming more stable and reversible. The addition of the ssDNA shows a decrease in total current density, as expected, due to the fact that ssDNA has negative

charges repelling the $Fe(CN)_6^{-3/-4}$. Upon addition of the ssDNA, the reaction is diffusion – limited at the electrode/electrolyte interface.

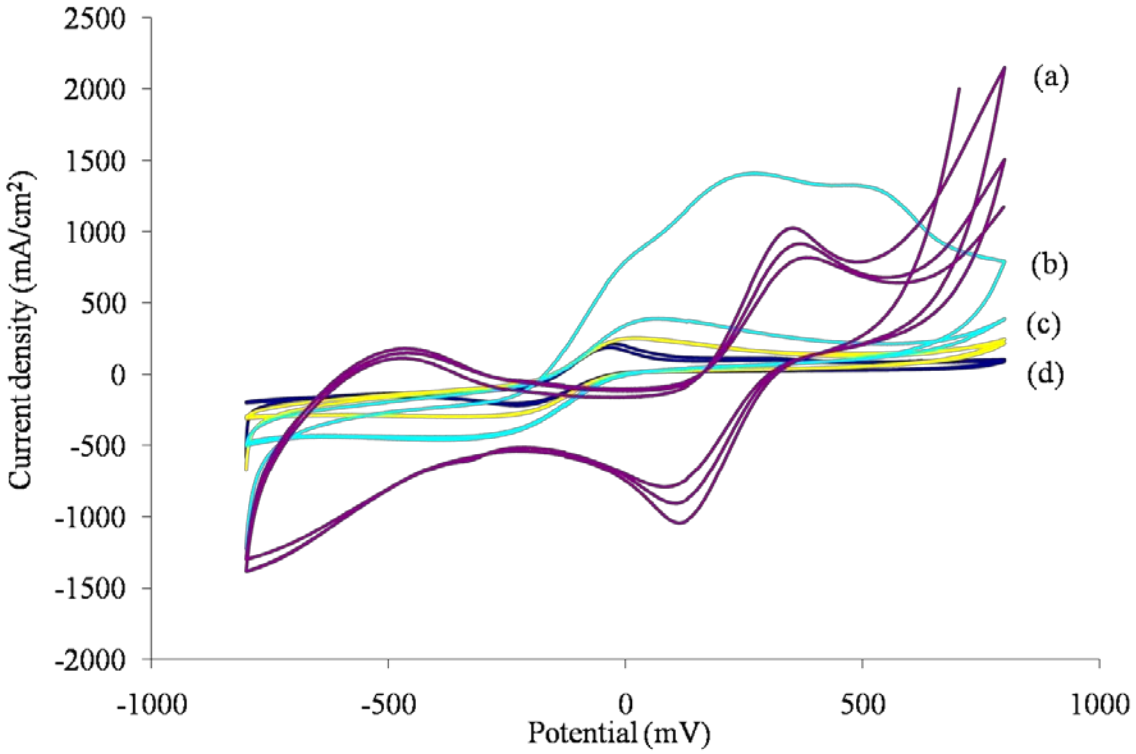


Figure 4.18. CVs of (a) BDD-COOH and BDD-COOH-ssDNA with a scan rate of (b) 50, (c) 20 and (d) 5 mV/sec.

Similar to the CNT – modified electrode for *Salmonella* DNA detection, electrochemical impedance spectroscopy was also used on the nanocrystalline BDD-modified electrode as a method of detection. Upon addition of the ssDNA to the BDD electrode surface, the charge transfer resistance increased to about twice the charge transfer resistance of just the electrode without any presence of DNA. As before, this is expected. In Figure 4.19. (c), the effect of the complementary DNA binding to the ssDNA can be observed. The complementary DNA once again causes a decrease in the

diameter of the semicircle of the Nyquist plot, indicating that more electrons are allowed to get shuttled through to the conductive surface. This can be viewed as a positive detection method of DNA.

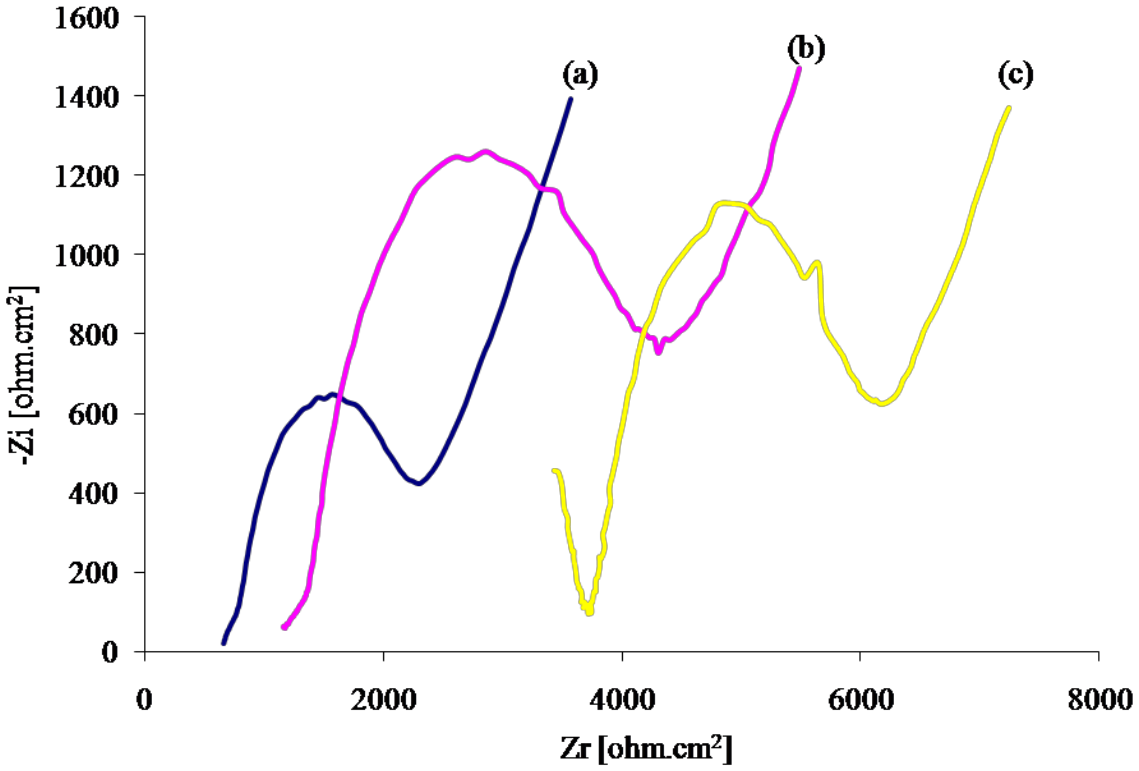


Figure 4.19. Nyquist plots of BDD (a) without DNA, (b) with ssDNA and (c) with complementary DNA attachment

As a secondary method of complementary DNA detection, fluorescence spectroscopy was used. The complementary DNA strand was labeled with a fluorescein isothiocyanate (FITC) tag. FITC has excitation and emission spectrum peak wavelengths of about 495 nm and 521 nm, respectively. When this molecule is placed under a fluorescence microscope and excited at the correct frequency, it will glow green. Several boron – doped diamond electrode samples were analyzed in this manner. It appears as

though the complementary DNA binds mostly uniformly over the entire functionalized diamond surface. It is seen in Figure 4.20. that the complementary DNA seems to follow the surface characteristics and does not bind where there is a crack or an area that was possibly over – etched during hydrogen treatment. Figure 4.20. verifies the results shown in the Nyquist plots that the complementary DNA does bind to the modified diamond surface and shows a high extent of hybridization with the ssDNA.

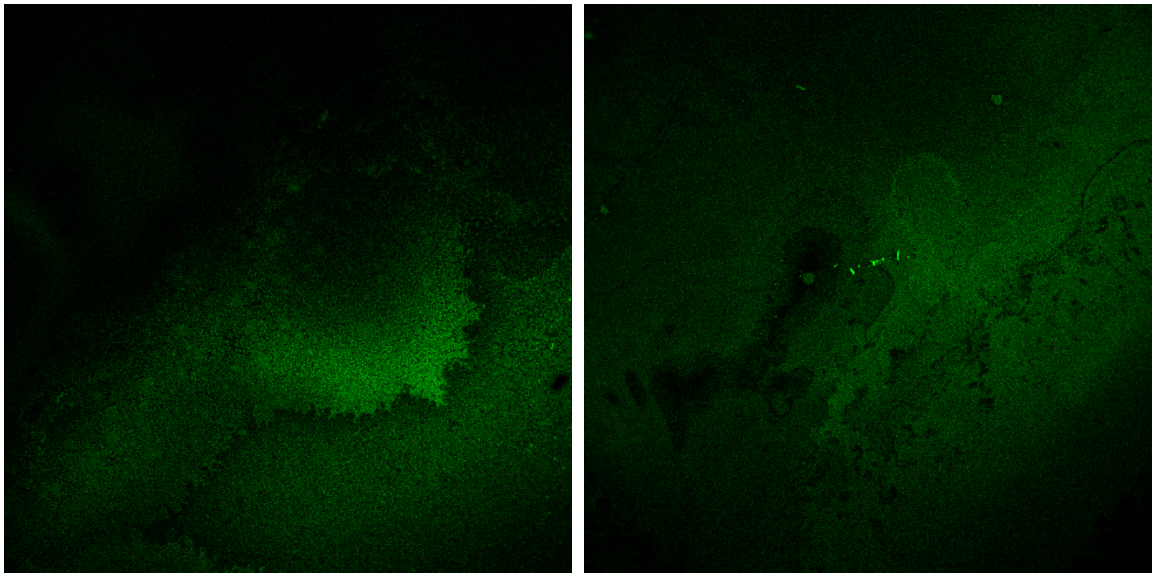

Figure 4.20. Fluorescent microscopy images at 400X of BDD with complementary DNA, two different locations on the same sample

### 4.3.6. Materials and Methods for Lactic Acid Sensing

The method of covalent immobilization of enzymes on diamond surfaces has been established elsewhere and was followed[120]. Both boron-doped and nitrogen – incorporated NCD was first electrochemically modified with nitrophenyl groups by performing cyclic voltammograms in a solution of 0.1 M tetrabutylammonium

tetrafluroborate and 1 mM 4-nitrophenyl diazonium tetrafluroborate. These surface groups were then reduced to aminophenyl groups in a 0.1 M KCl solution of 10% methanol at -1.0 V vs. Ag/AgCl. The electrode was then placed in a solution of 0.1 M succinic anhydride in dimethylformamide (DMF) for a few hours. Once dried, the samples were immersed wtih constant stirring in 0.1 M 2-morpholinoethanesulfonic acid containing 1-ethyl-3-[3-dimethylaminopropyl] carbodiimide hydrochloride and N-hydroxysulfosuccinimide for 1 hr. About 10 IU of the enzyme lactate oxidase (LOX, E.C. 1.12.12.4 from *Pediococcus* species, 49 U/mg, Sigma-Aldrich) was dissolved in 0.1 M acetate buffer. A certain amount (about 50 µl) of the enzyme-buffer solution was pipetted onto the modified NCD films and refrigerated overnight. The electrodes were rinsed with deionized water to remove any unbound enzyme and subsequently dried in a nitrogen stream prior to use.

The exposed surface area of the electrode was about 0.8 $cm^2$ and the data has been normalized to this surface area. Fourier transform infrared spectroscopy (FTIR) analysis was performed on a Perkin-Elmer Spectrum One Spectrometer. UV-Vis spectroscopy was performed on the samples immediately prior to cyclic voltammetry sensing using a Jasco UV-Vis Spectroscope.

### 4.3.7. Lactic Acid Sensor Discussion

Boron – doped and nitrogen – incorporated nanocrystalline films were studied for electrochemical activity towards lactic acid. Based on the following reaction, electrochemical detection occurs:

$$\text{LOX} + \text{lactate} \rightarrow \text{LOX} + \text{pyruvate} \quad (24)$$

$$LOX + O_2 \rightarrow LOX + H_2O_2 \quad (25)$$

$$H_2O_2 - 2e^- \rightarrow O_2 \quad (26)$$

Functionalized electrodes were constructed with both types of NCD to determine which doping method provided a more sensitive electrode. To understand the effect of the dopant on the NCD, the Mott-Schottky plot was evaluated for both types of films. It is a well-known fact that boron is introduced uniformly within the diamond lattice, while nitrogen incorporation takes place mainly at the grain boundaries. The Mott-Schottky plot (Figure 4.21.) shows a drastic change in the slope of the left – hand side of the curve for the nitrogen – incorporated NCD. This change in slope represents non – uniform donor distribution within the film. On the other hand, the slope on the left – hand side of the curve for the boron – doped NCD is nearly linear. Due to the uniform arrangement of boron in the NCD, it is predicted that this type of film will be better for the electrochemical detection of lactic acid.

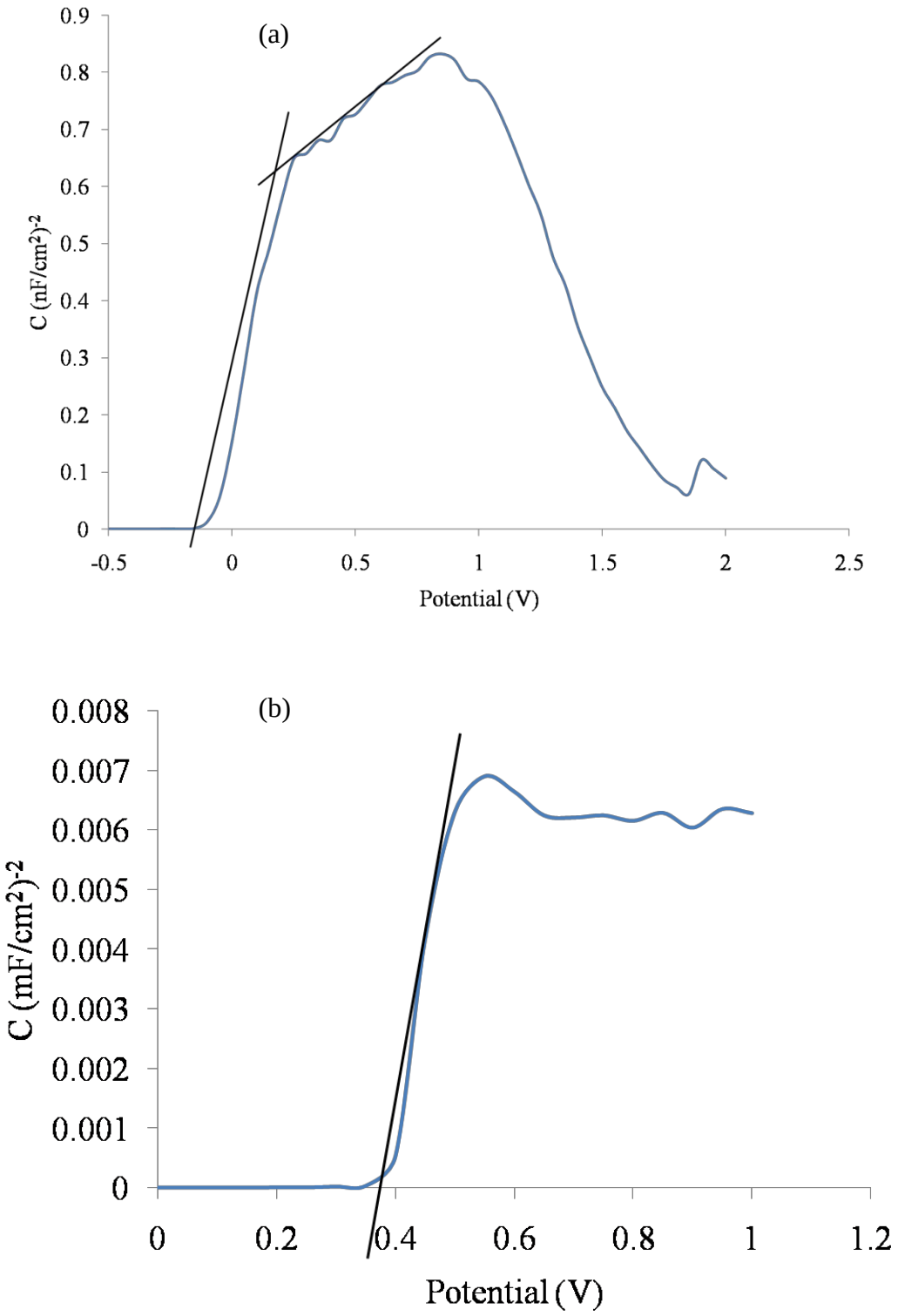


Figure 4.21. Mott-Schottky graph of (a) nitrogen – incorporated and (b) boron – doped NCD

FTIR analysis was performed on all samples. First, a baseline for intrinsic diamond was established. Then, FTIR spectra were taken for boron – doped, nitrogen – incorporated and samples with lactate oxidase immobilized on the surface (Figure 4.22). There is little difference between intrinsic diamond and n-doped diamond, as to be expected. However, for b-doped diamond we see the presence of a peak at about 3700 $cm^{-1}$. The NCD with LOX shows an amino group at about 3500 $cm^{-1}$ and peak widening at 1250 $cm^{-1}$, which correspond to the enzyme lactate oxidase.

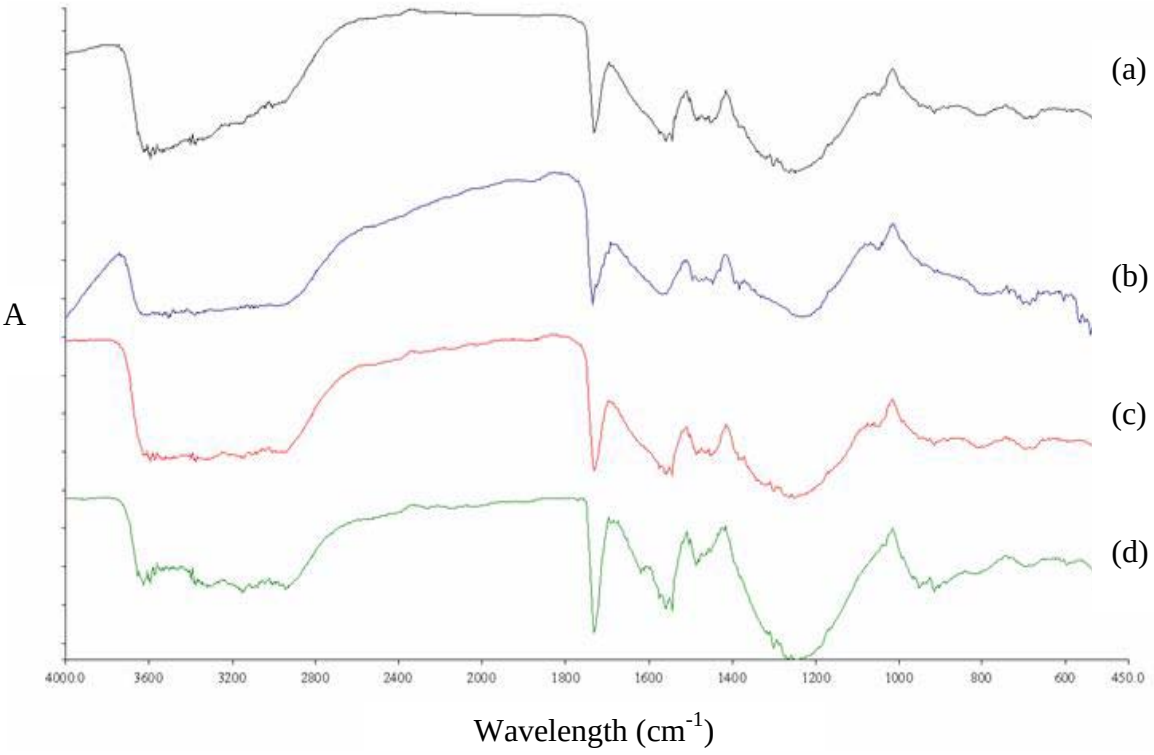


Figure 4.22. FTIR spectra of NCD electrodes : (a) intrinsic, (b) boron – doped, (c) n – incorporated, (d) nitrogen – incorporated with LOX

UV-Vis was performed on the NCD electrode immediately before detection to determine the stability of the sensor. A 10 minute time-study was performed to determine the activity level of the electrode prior to use. The activity of the enzyme was measured even minute for 10 minutes at the wavelength of 585 nm. It was found that the activity of LOX continued to increase from 1.0109 units/mg for about six minutes to 0.0192 units/mg. After six minutes, the activity peaked and then became stable. UV-Vis was performed before every experiment to also gauge the shelf – life of the electrode. It was found that after 3 months, the activity of the electrode decreased to about 60% of its original measurement.

Cyclic voltammetry was measured on both types of NCD electrodes in PBS buffer solutions with increasing concentrations of lactic acid. The scan rate for all CVs was 50 mV/s. As shown in Figure 4.23, the CV for the nitrogen – doped NCD electrode has poor sensitivity to lactic acid. A slight reduction peak is noted at around 200 mV; however, there is no noticeable oxidation peak. Due to the asymmetry of the voltammogram, the electrochemical reaction is not reversible. It is believed that this poor response is due to the properties of the nanocrystalline diamond when it is doped with 20% nitrogen. The nitrogen tends to be incorporated at the grain boundaries, resulting in a non – uniform conductive film. As a result, the entire surface area is not completely utilized for lactic acid detection and the response that it does provide is not as stable as desired for enzymatic biosensor applications.

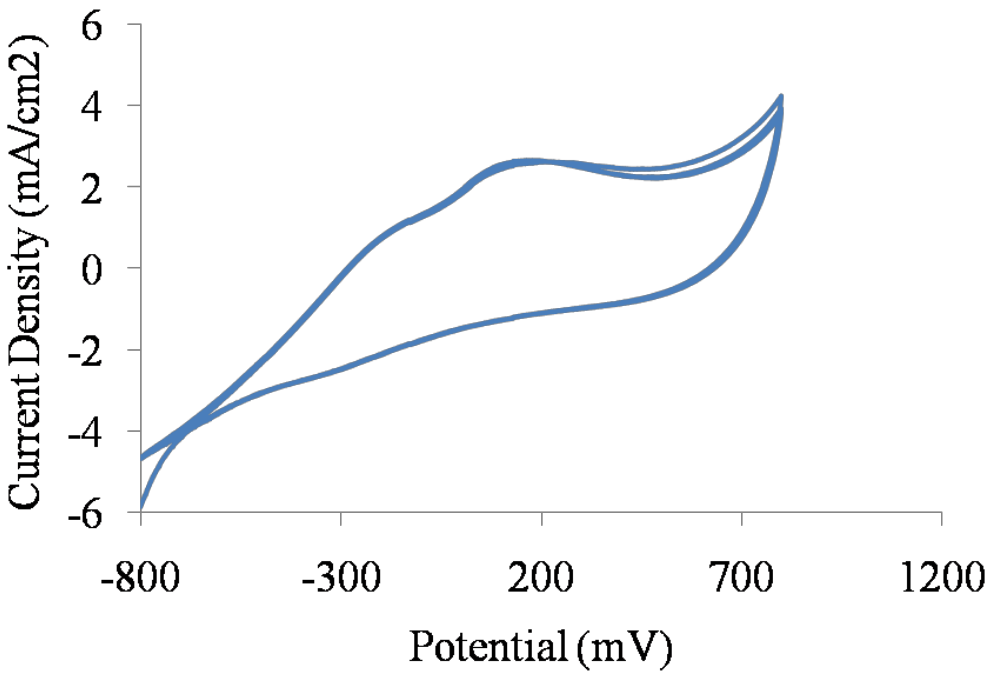


Figure 4.23. CV of nitrogen – incorporated NCD in 5 mM lactic acid

The modified boron – doped nanocrystalline diamond electrode provided a much better response to lactic acid. Figure 4.24. shows the CVs for this electrode immersed in lactic acid concentrations ranging from 5 mM to 20 mM. Note that the higher concentrations of lactic acid give a higher current density, which is typical of amperometric detection. Even at 5 mM, the sensor still provided a current density of about 1.5 mA/cm$^2$. The voltammograms also appear to be much more symmetrical, indicating that the redox reaction is reversible at the electrode surface. The peak current density was plotted against the lactic acid concentration in Figure 4.25. A nearly linear relationship is observed; as the concentration of lactic acid increases, the current density increases as well. Due to the uniformity of the boron concentration in the NCD, this

electrode is much more responsive and sensitive to varying lactic acid concentrations in a phosphate buffer solution.

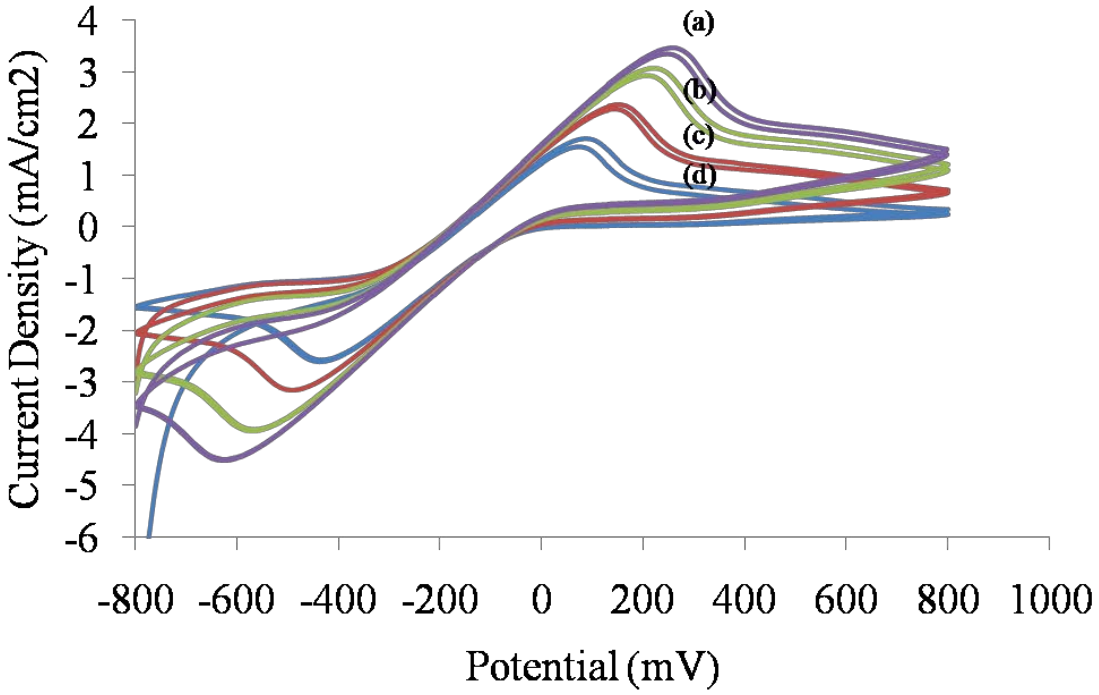


Figure 4.24. CV of boron – doped NCD in increasing concentrations of lactic acid: (a) 20 mM, (b) 15 mM, (c) 10 mM, and (d) 5 mM

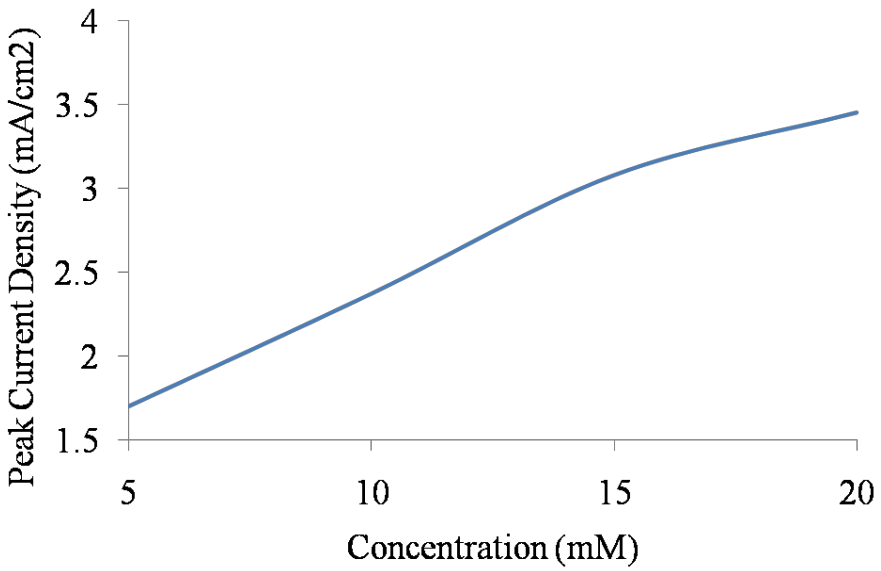


Figure 4.25. Peak current density as a function of lactic acid concentration

**4.4. Summary**

In summary, modified carbon based electrodes were developed for the detection of different biological species. Carbon nanotube and boron – doped nanocrystalline diamond have been prepared for detection of DNA from *Salmonella enterica* serovar Typhimurium using impedimetric sensing techniques. While both nano – carbon materials proved to be excellent electrodes for detection of DNA hybridization, the carbon nanotube electrode showed more sensitivity. Most likely, this is due to the fact that the functionalized SWNTs deposited on the glassy carbon provided a rich, active, high surface area matrix for the binding of the aminated ssDNA probe and consequentially allowing for more target hybridization sites on the electrode surface. It was found that simply by increasing the concentration on carbon nanotubes on a glass carbon surface, the current density response increases very nicely. Target DNA sensing

was accomplished by measuring the change in the overall impedance of the system as well as measuring the charge transfer resistance. Fluorescent microscopy was also performed on the BDD electrode. While fluorescence is a good method to verify DNA attachment, it only provides qualitative and not quantitative results. These images show that the ssDNA and complementary strand DNA bonded fairly uniformly over the diamond surface. Finally, the electrochemical properties of boron – doped and nitrogen – incorporated NCD thin films was examined using Mott-Schottky and their response to lactic acid was measured. Due to the non – uniform donor concentration of nitrogen in the diamond, these electrodes are not as ideal for sensing in an aquous solution. The boron – doped NCD displayed a linear response to lactic acid in the range of 5 mM to 20 mM.

# CHAPTER 5: BISMUTH ANTIMONY NANOWIRE RESULTS AND DISCUSSION

## 5.1. Introduction

The thermoelectric effect is traditionally divided into the Seebeck effect, the Peltier effect and the Thomson effect. The Seebeck effect was the first of the three thermoelectric phenomenon discovered in 1821, when Thomas Johann Seebeck realized that a junction of dissimilar metals produces an electric current when exposed to a temperature gradient. In 1834, Jean-Charles Peltier discovered the opposite of the Seebeck effect; an electric current at the junction of two different metals will either heat or cool depending on the direction of the applied current. Finally, the Thomson effect, named for William Thomson, describes that a conductor will either absorb or emit heat depending on the material. Combining these effects, the thermoelectric effect describes the conversion of temperature differences to an electric potential and vice versa. Peltier devices, as called thermoelectric coolers (TECs), operate by applying a voltage to one side of a thermocouple, which will cause one side to warm while the other side cools. A schematic of a typical thermoelectric cooler is shown in Figure 5.1. The goal of this research was to replace the bulk materials used for *p*–type and *n*–type legs with oriented arrays of nanowires. In particular, the following work focuses on replacing the *p*–type leg of the device with ordered $Bi_{(1-x)}Sb_{(x)}$ nanowires of a particular length and diameter.

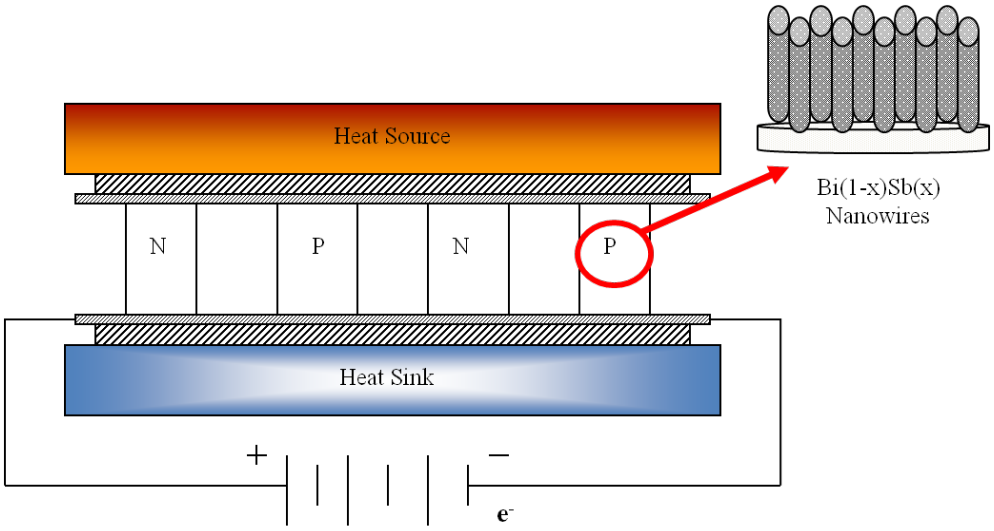


Figure 5.1. Schematic of thermoelectric cooler with $Bi_{(1-x)}Sb_{(x)}$ nanowires as the *p*-type leg

## 5.2. Material Selection

The unique characteristic defining an efficient thermoelectric material is that it must be highly electrically conductive while at the same time not being thermally conductive. These characteristics govern the dimensionless thermoelectric figure of merit, *ZT* (see Section 1.2.). Identifying materials with high *ZT* values is a challenge, based on the conflicting interrelated characteristics that are required. One long – standing approach to achieve a high *ZT* is to reduce the lattice thermal conductivity by scattering phonons within the unit cell by creating rattling structures or point defects such as interstitials, vacancies or by alloying[22]. The second strategy is to use complex crystal structures to separate the electron-crystal from the phonon-glass[121]. The region responsible for electron transport would be an electron – crystal of a high-mobility semiconductor, while the phonon – glass would be ideal to house disordered structures

and dopants without disrupting the electron-crystal. A third strategy is to scatter phonons at interfaces, leading to the use of multiphase composites mixed on the nanometer scale[122]. High thermoelectric power semiconductor alloys of Bi, Sb, and Te are used since they have poor thermal conductivity and can be doped to improve electrical conductivity.

Based on theoretical studies, bismuth nanowires doped with antimony were chosen for this project. It has been calculated that $Bi_{(1-x)}Sb_{(x)}$ nanowires can produce a *ZT* of about 1.2 at 77 K with a wire diameter of about 40 nm. The enhancement in *ZT* is attributed to the coalescence in energy of the subband edges of the ten hole pockets of this system and the resulting high density of states[123]. In order to replace the semiconductor legs of a standard thermoelectric device the nanowires need to be manufactured in high density ($>10^{10}/cm^2$ over ~ $0.2cm^2$), oriented, high aspect ratio arrays (40 nm diameter by 100 mm length). In order to be useful in miniaturized devices, the fabrication process needs to be compatible with on-chip processing. In this section, these manufacturing and growth issues are addressed, as well as data on the thermoelectric efficiency of produced nanowires is presented.

### 5.3. Template Fabrication

The fabrication of well aligned nanowire arrays is a vital project for the realization of thermoelectric coolers for novel microelectronic and nano electrical mechanical systems (NEMS). The chosen approach used for nanowire growth in this project was to develop an anodized aluminum oxide (AAO) template. Anodization is a process of producing a film of $Al_2O_3$ on aluminum when a voltage is applied through an acidic electrolyte. During this process, the aluminum is the anode and a suitable material

such as a titanium or platinum mesh is the cathode. Under precise control of parameters such as acid concentration and applied voltage, ordered pores will be produced. The AAO is usually composed of a thick porous oxide layer on top of a smaller, yet distinct barrier oxide layer. The pores typically have diameters of 10 – 100 nm with varying wall thickness and depth. For electrochemical nanowire deposition inside such a porous array, complete removal of the barrier oxide layer is vital in order to expose the underlying seed metal. Electrochemical impedance spectroscopy (EIS) is a non-destructive technique used to characterize the anodization and etching process. EIS was measured on several samples of anodized alumina films as a method for describing the growth and dissolution of the barrier oxide layers.

### 5.3.1. Materials and Methods

This project has two modules: first, to anodize aluminum samples and second to perform EIS on the as-prepared coupons. Anodization of the aluminum films was carried out in a 3 wt % solution of oxalic acid (pH 2) at 2 °C with a platinum mesh counter electrode. A DC voltage was applied between the Al film and the counter electrode. Figure 5.2. shows a schematic representation of the anodization setup.

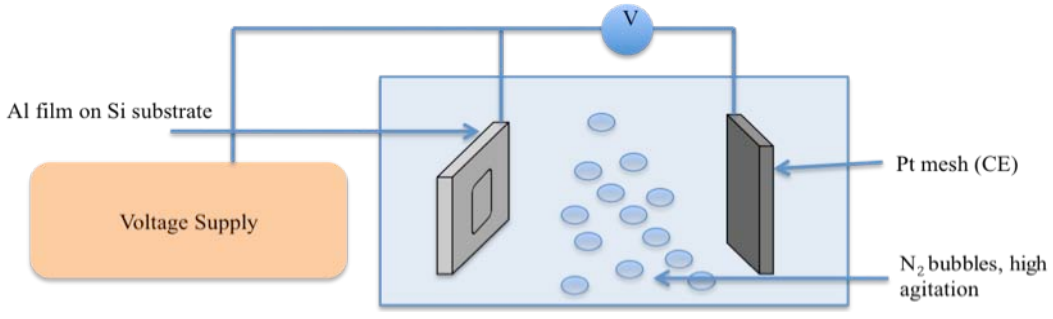


Figure 5.2. Schematic of anodization setup

The anodization area of each sample was approximately 1.5 $cm^2$. Smooth Nd-doped Al films were grown on a Si substrate on top of a stress-free Pt layer, which bonds to the Si substrate via a W adhesion layer. All metal films were deposited by sputtering and the Al films were 570 nm thick with an underlying layer of 50 nm platinum. A two-step anodization process was used to obtain the porous templates. The initial anodization was at 50 V for less than 1 minute. This quick anodization step provided the rough template. Immediately following the first anodization, the films were etched in a 5% $H_3PO_4$, $CrO_3$ bath at room temperature. The time of this etch varied from 10 min. to 30 sec in order to achieve an optimal etch of the oxide layer. The second anodization step began at 50 V, 2 °C with a systematic potential reduction in order to more efficiently etch the barrier oxide layer. Because the anodization and etch rates were initially unknown, samples were anodized systematically at several voltage and time combinations until the films appeared to become visibly iridescent (this is a common characteristic of AAO films). As a quick check to verify anodization, the films were tested for conductivity with an ohmmeter. If the anodized section of the sampled showed an infinite resistance, the film was considered anodized and set aside for further investigation with EIS. If the anodized sample still displayed conductivity, it was discarded and a fresh sample was again anodized at the same voltage but for a longer time period until the film completely displayed no conductivity (which indicates that the Al had converted to $Al_2O_3$) and possessed an iridescent shine.

The current density was monitored during the anodization process. Two current contributions can be distinguished: a current density associated with formation of an initial aluminum oxide barrier layer at the interface with the aluminum metal, and a

current density responsible for the subsequent nucleation of pores. When the alumina barrier layer is completely formed, the current density is known to decrease abruptly. Current density increases during pore development until the latter becomes stable. The combined effect of these two contributions leads to the overall current behavior shown in Figure 5.3.

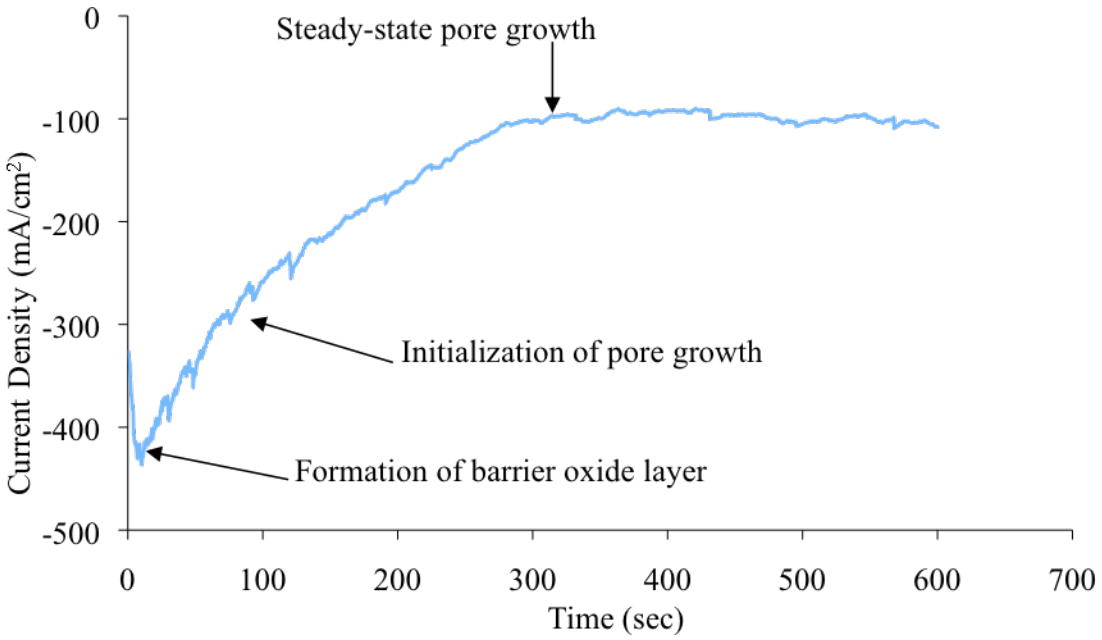


Figure 5.3. Typical current – time anodization profile

Following anodization, EIS was used as a diagnostic technique to characterize the anodized films, including the thickness of the barrier oxide layer in order to determine the appropriate barrier oxide layer etch time. EIS was performed in a three-electrode cell with the anodized sample as the working electrode with a Ti wire counter electrode plus a Ti wire reference electrode. A photo of this setup is shown in Figures 5.4., 5.5. EIS experiments were carried out in an aqueous solution of 1 M sodium sulfate at room temperature over a frequency range of 100 kHz to 10 mHz with a Solartron Impedance

Analyzer. EIS was first performed on an aluminum sample that had not been anodized, and then on the other samples anodized at 15 and 20 V. After a good representation of measurements was conducted, EIS was used to characterize the post-anodization etching process. In order to etch away the barrier oxide layer, samples were placed in a bath consisting of 0.4 M phosphoric acid and 0.2 M chromic acid at room temperature for a measured amount of time. The samples were then transferred back into the electrochemical cell and for EIS testing. After each test, the samples again went through a timed etch and impedance measurements were taken after each etch.

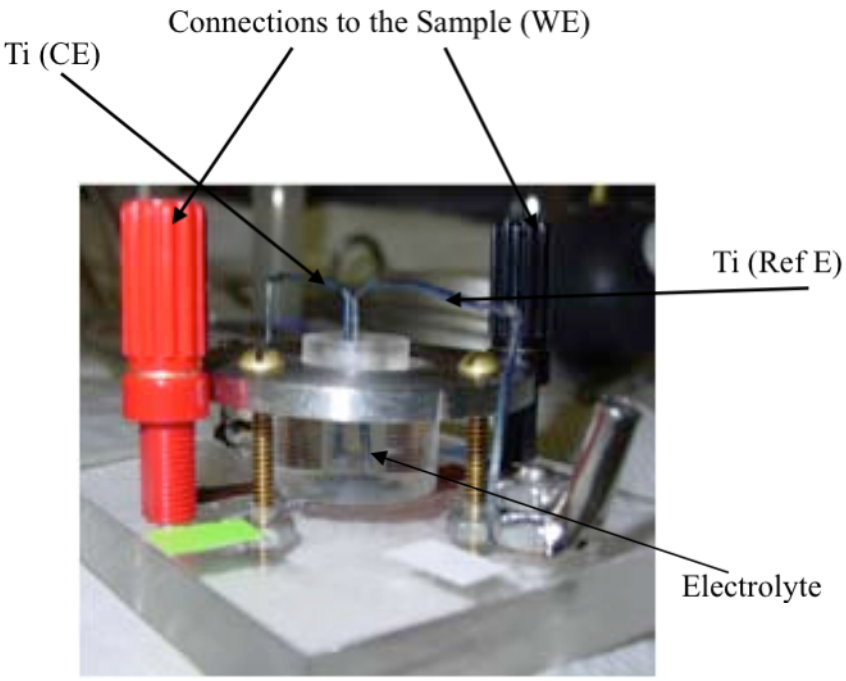


Figure 5.4. Side view of EIS setup

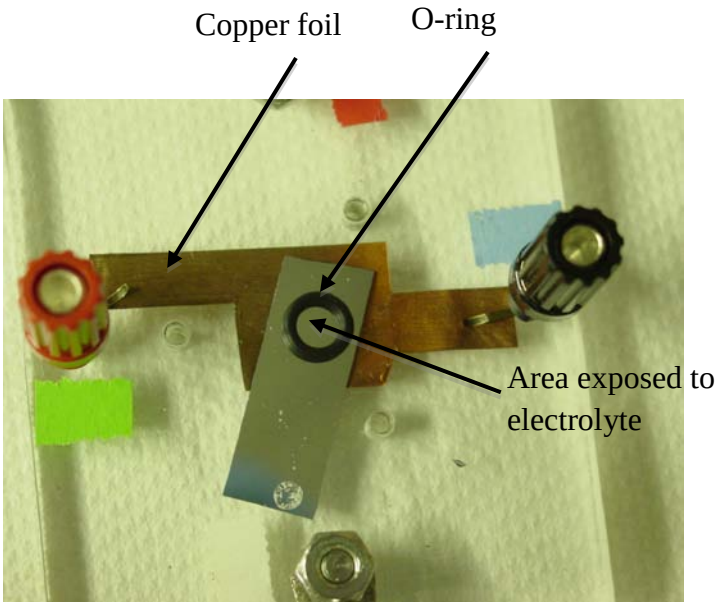


Figure 5.5. Disassembled top view of EIS setup

### 5.3.2. Discussion

A top view of a typical AAO sample is shown in Figure 5.6 and a corresponding cross – sectional view is shown in Figure 5.7. It is evident in the cross – sectional view that a barrier oxide layer exists on top of the platinum layer. In order for nanowires to grow in this template, this barrier oxide layer must be etched away as much as possible to expose the underlying platinum. The equivalent circuit for a typical anodized aluminum oxide sample can be modeled as the electrochemical cell solution resistance connected in series with two parallel combinations of a constant phase angle (CPE) and a resistor (Figure 5.8.). The admittance of the CPEs in the equivalent circuit can be calculated from equation 20. The first parallel resistor/CPE combination can be used to describe the barrier oxide layer, where the capacitance of it is approximately equal to $Y_0$. Hence, the

EIS data was fit to the equivalent circuit and the barrier oxide thickness of the samples was calculated using the following:

$$C_{bl} = \varepsilon\varepsilon_0 \frac{A}{d} \tag{24}$$

where $C_{bl}$ is the barrier layer capacitance (F), $A$ is the AAO surface area ($cm^2$), $d$ is the barrier layer thickness (cm), $\varepsilon_0$ is the permittivity of a vacuum ($8.85 \times 10^{-14}$ F/cm), and $\varepsilon$ is the dielectric constant of alumina, 9.5. This data is given in Table 5.1. Figures 5.9, 5.10 represent the Nyquist and Bode data sets collected prior to anodization and immediately after anodization for 10 min. at 15 and 20 V, respectively. It can be seen that the diameter of the semicircle gradually decreases with an increase in anodization voltage, holding the time of anodization constant. The high frequency arch also increases as anodization voltage increases. The magnitude of impedance also increases with anodization voltage. The ratio of thickness of the barrier oxide layer to anodizing dc voltage was found to be 1.015 nm $V^{-1}$, which is consistent with the accepted range in literature of 1.0 – 1.4[124].

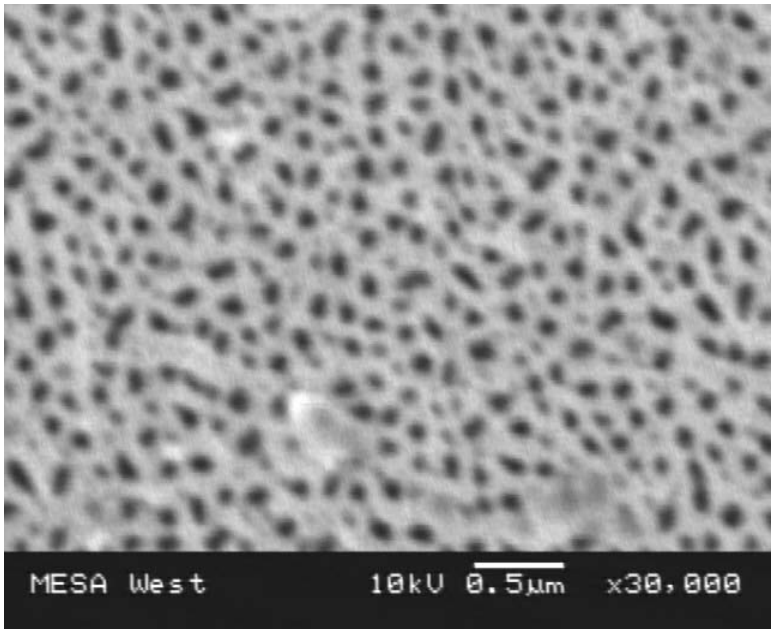


Figure 5.6. Top view of typical AAO sample

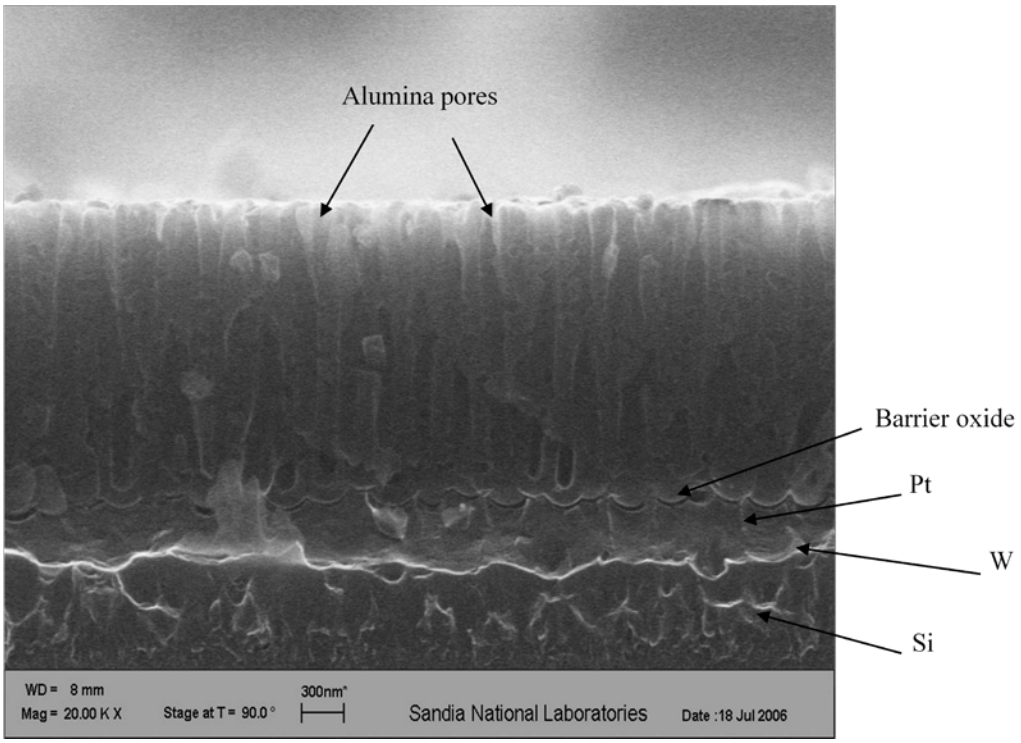


Figure 5.7. Cross – section of AAO template

Table 5.1. Data from equivalent circuit fit for sample anodized at 15 V for 10 min, n ~ 0.95.

| Etch Time (min) | Capacitance (F) | Barrier Oxide Thickness (nm) |
|---|---|---|
| 0 | $1.08 \times 10^{7}$ | 15.23 |
| 0.5 | $1.13 \times 10^{7}$ | 14.62 |
| 1.5 | $1.35 \times 10^{7}$ | 12.27 |
| 3.5 | $1.44 \times 10^{7}$ | 11.43 |

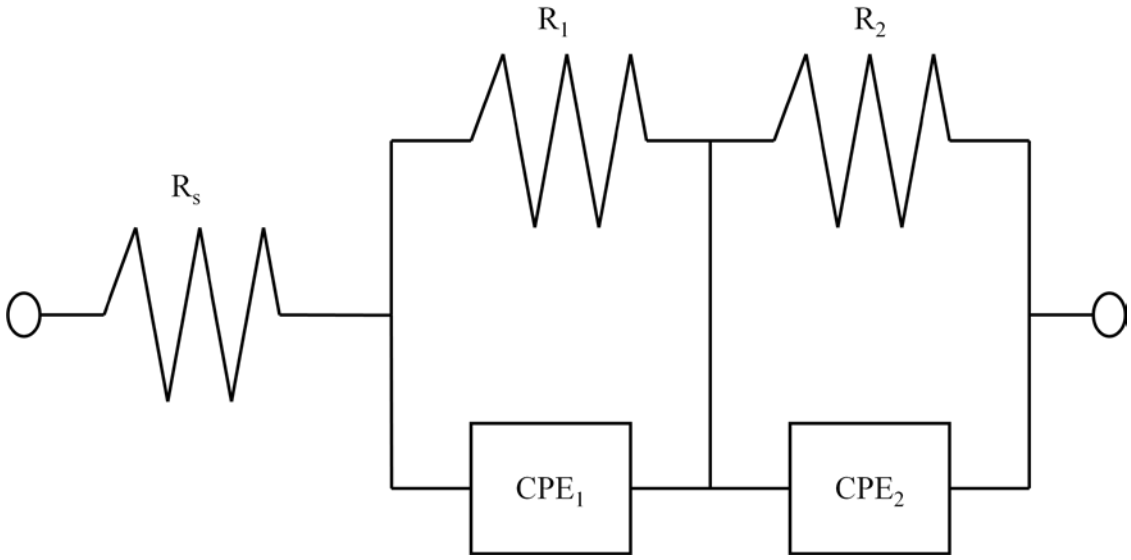


Figure 5.8. Equivalent circuit model of AAO sample

The behavior of the samples appears to be that of truncated transmission lines. Figures 5.9. and 5.10. show the impedance response of the AAO after sequential etching times. It is evident that at high frequencies the system acts as a transmission line; however, at lower frequencies $R_s << R_p$ it behaves as a discrete system. The thickness of the barrier oxide layers calculated in Equation 24 does verify dissolution. Figure 5.11.

represents the barrier oxide layer thickness at sequential etching times in the 0.4 M phosphoric acid and 0.2 M chromic acid. Dissolution is evident, although it does not appear to follow a linear rate. It is also important to note that while the barrier oxide layer is being etched, so is the alumina template as well. A slight change in the color of the sample was noticed from prior to etching and once the etching was complete. Although the template and the barrier layer etch at different rates, it would be complimentary to know the thickness of the template after each etching process. The author notes that it may be better to begin with a thicker film of aluminum, such as 1 - 5 microns, sputtered onto the sample for future tests. The thicker film will compensate for any undesired etching of the template during the dissolution of the barrier oxide layer.

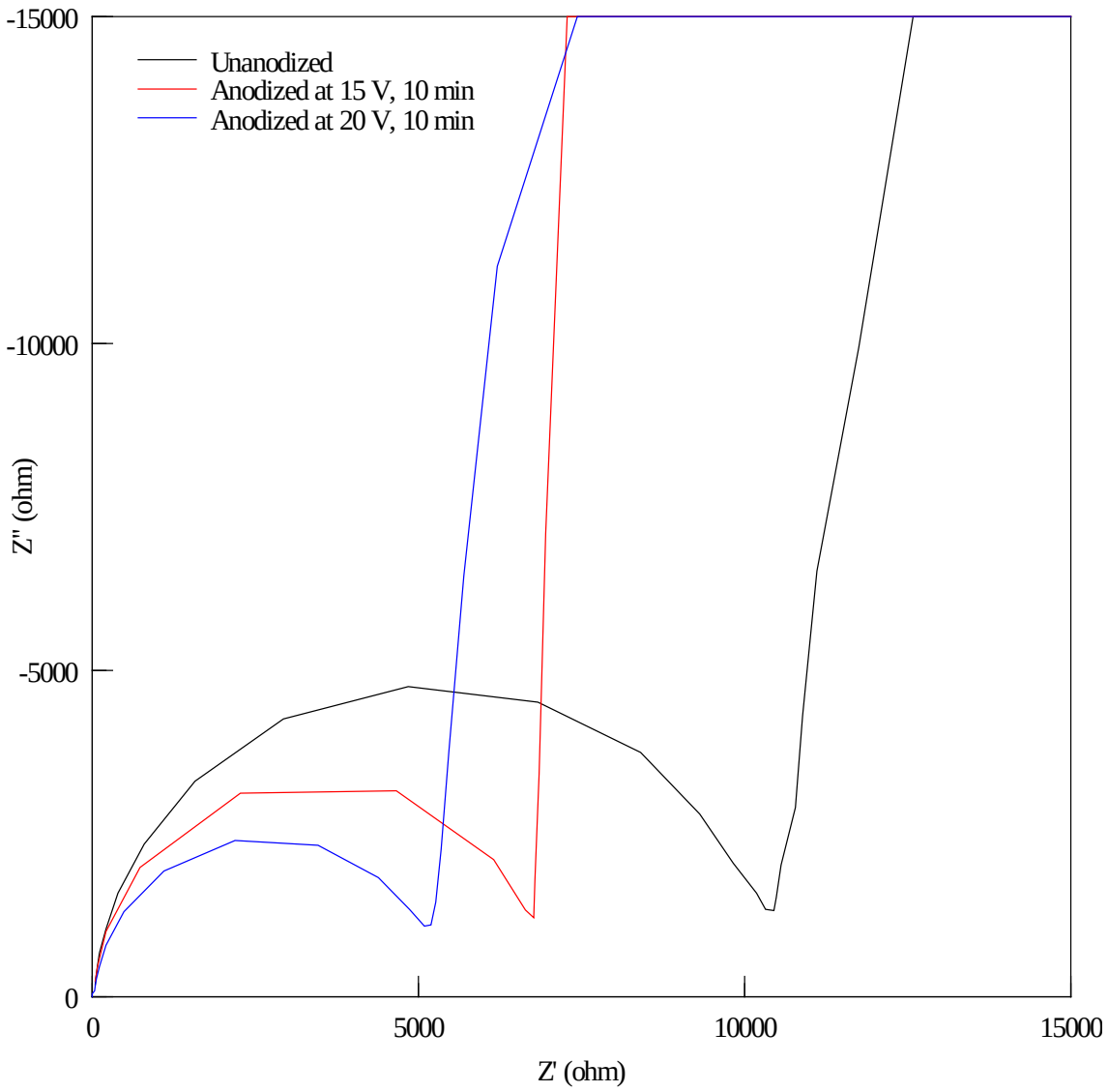


Figure 5.9. High frequency Nyquist data collected at OCP prior to anodization and after anodization at 15 V for 10 min. and at 20 V for 10 min.

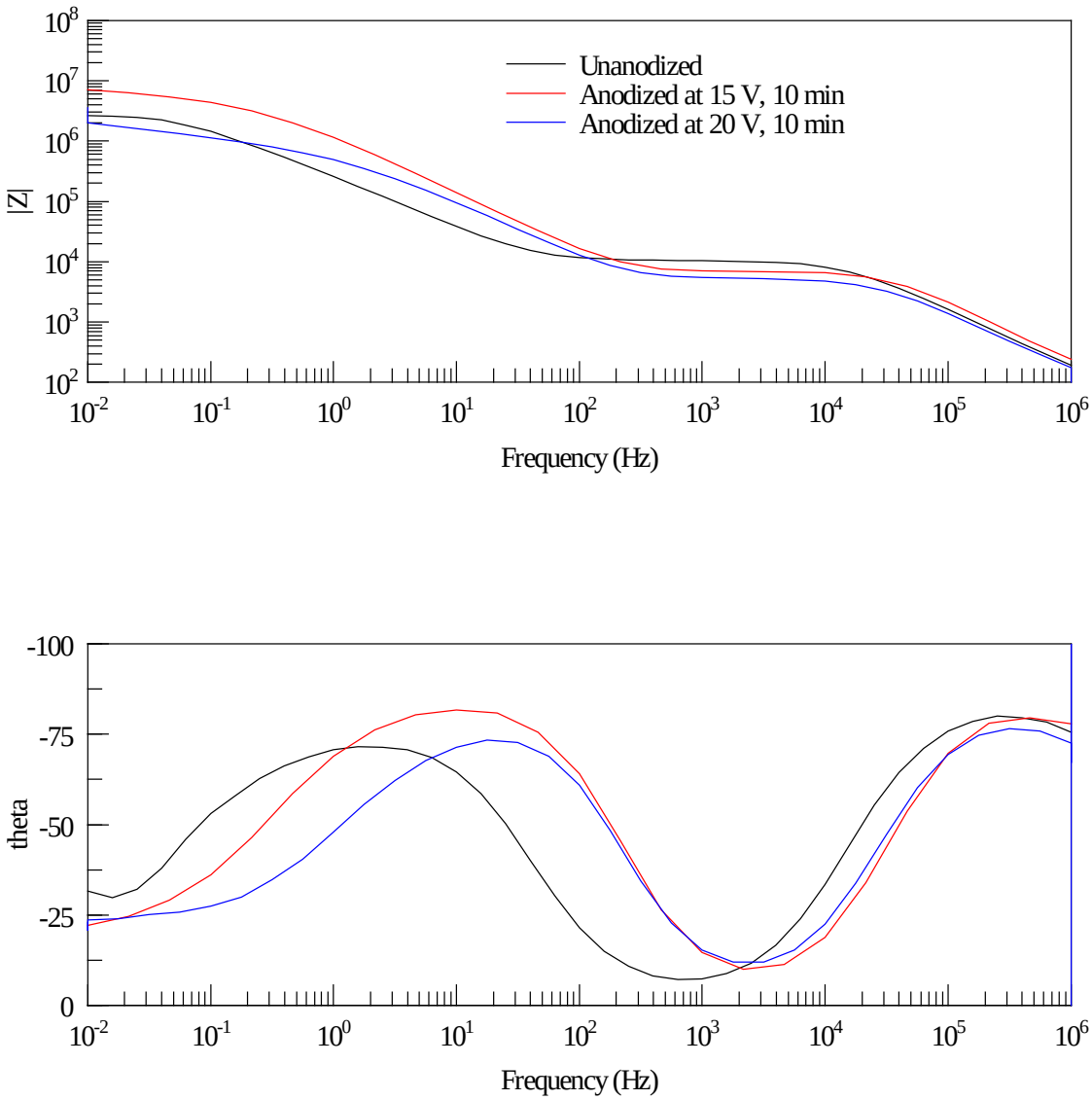


Figure 5.10. Bode data (magnitude and phase) collected at OCP prior to anodization and after anodization at 15 V for 10 min and at 20 V for 10 min.

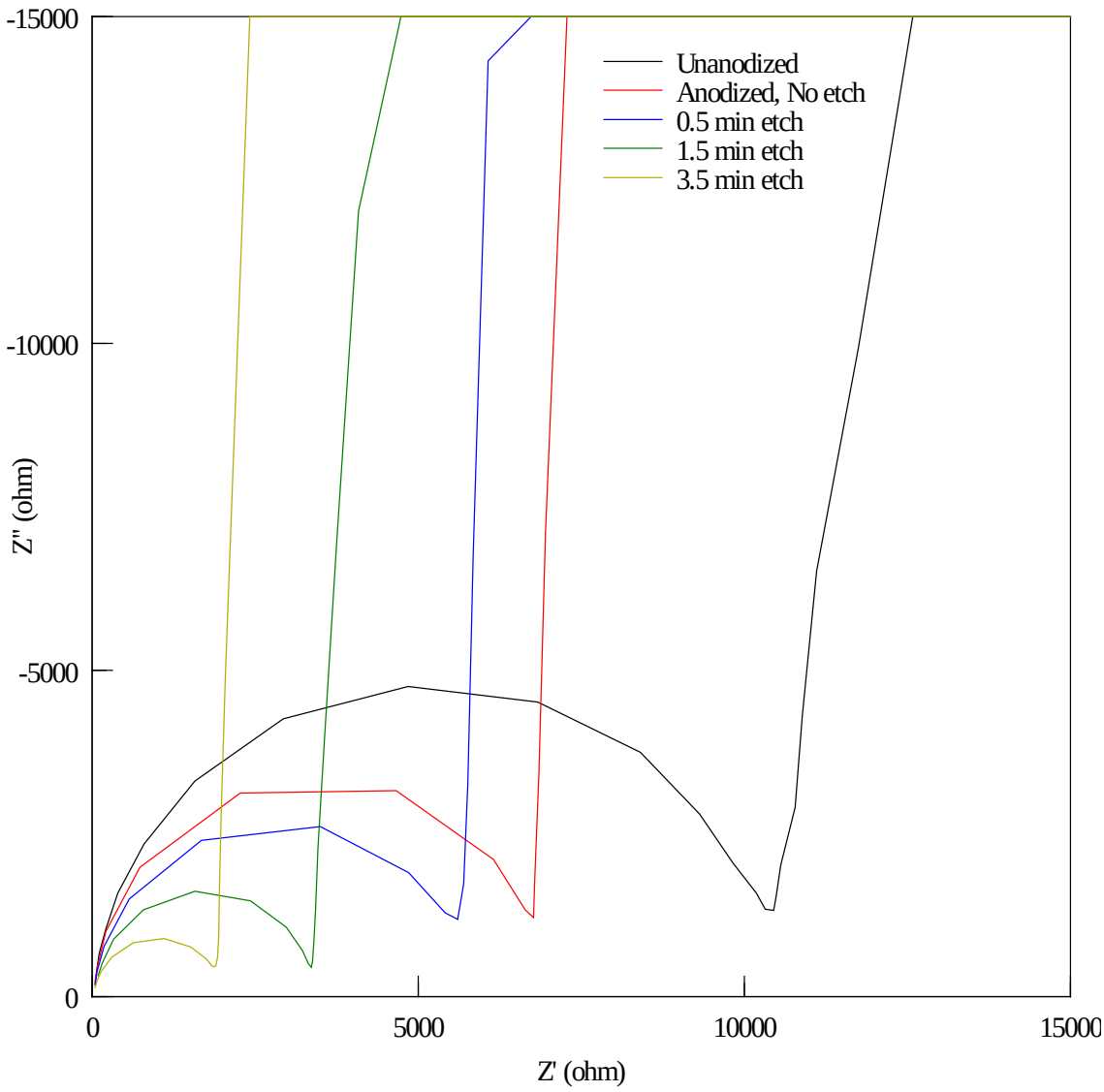


Figure 5.11. High frequency Nyquist data collected at OCP after anodization with no post-etch, 0.5 min, 1.5 min, and 3.5 min post-etch

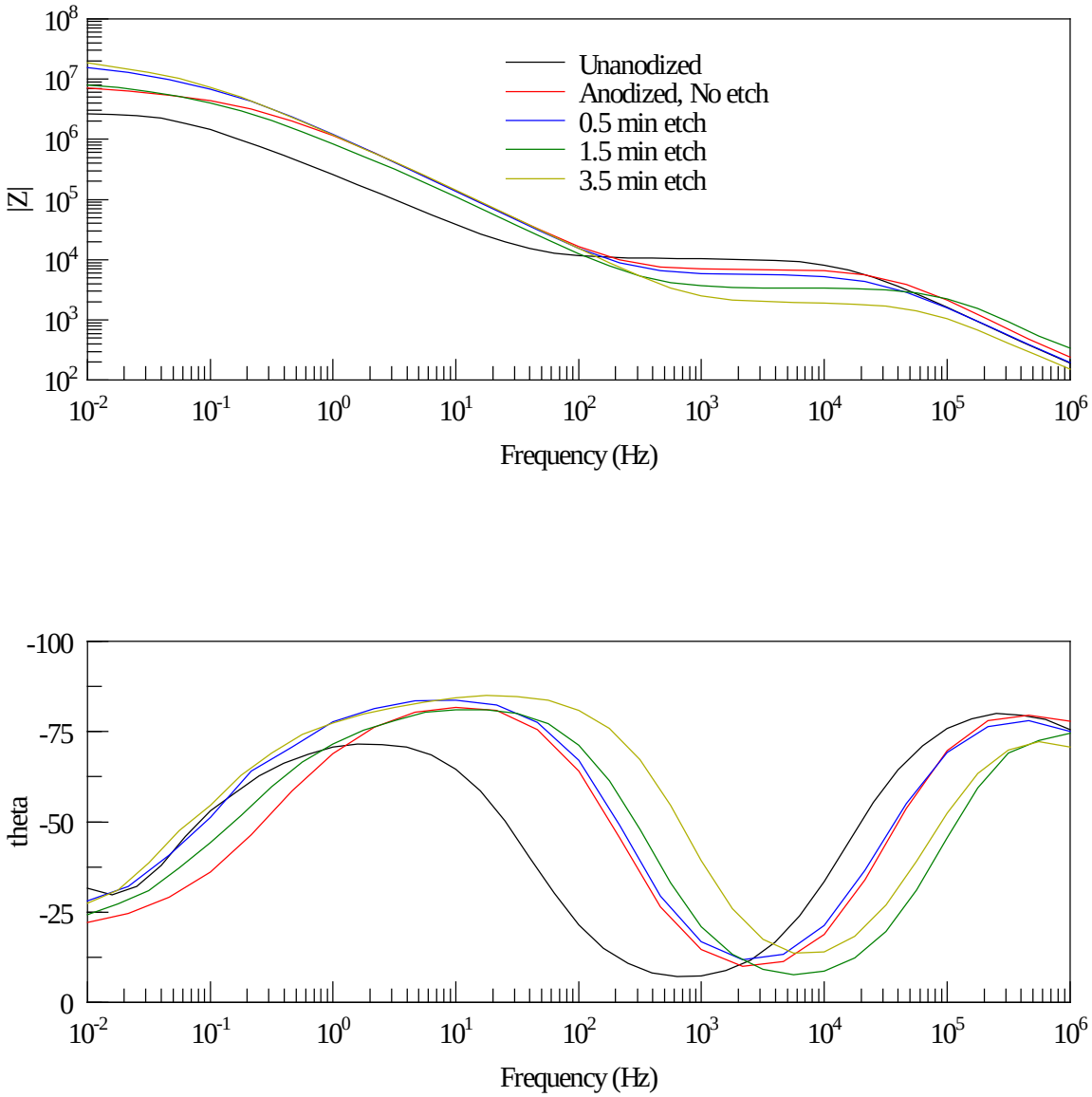


Figure 5.12. Bode data (magnitude and phase) collected at OCP after anodization with no post-etch, 0.5 min, 1.5 min, and 3.5 min post-etch

## 5.4. Nanowire Growth

### 5.4.1. Materials and Methods

Electrochemical experiments were performed using a Radiometer Analytical Voltalab 40 electrochemical analyzer. All electrochemical measurements were executed in a standard three electrode system with the AAO substrate serving as the working electrode, a platinum mesh as the auxiliary electrode, and an Ag/AgCl reference electrode at room temperature. The supporting electrolyte for all nanowire electrodeposition was a solution of dimethylsulfoxide (DMSO) for two reasons: first, antimony salt has a high solubility in DMSO and second, DMSO does not aggressively attack the anodized alumina template in which deposition occurs. Several electrochemical measurements, utilizing cyclic voltammetry, impedance spectroscopy, and chronopotentiometry were used to characterize the kinetic limitations of plating $Bi^{3+}$ $Sb^{3+}$ into nanoscale pores.

### 5.4.2. Fundamentals of Nanowire Electrodeposition

When using electrodeposition as the method of nanowire growth, the nanowire dimensions (length and diameter) are controlled by the nanopore dimensions of the template. It is important to address any mass transport concerns when plating into small pores. As mentioned in Chapter 3, the three modes that act resistively to the current flow used to deposit material in the pores are diffusion, convection and ionic migration. Resistance due to ionic migration can be easily overcome if a supporting background electrolyte is used. Resistance based on convection is highly limited by the fact that agitation in micro and nanoscale pores is limited. Therefore, the primary mass transport

concern for electrodeposition of nanowires is diffusion. A rotating disk electrode (RDE) was employed to study the effects of diffusion. A schematic of the experimental setup is shown in Figure 5.13. The rotating disk, or working electrode is platinum since the nanowires will be plated on a platinum seed layer. A platinum mesh acts as the counter electrode with an Ag/AgCl reference electrode. The disks's rotation is described in terms of angular velocity. As the disk turns, some of the solution described as the hydrodynamic boundary layer is dragged by the spinning disk and the resulting centrifugal force flings the solution away from the center of the electrode. Solution flows up, perpendicular to the electrode, from the bulk to replace the boundary layer. The sum result is a laminar flow of solution towards and across the electrode. The rate of the solution flow can be controlled by the electrodes angular velocity and modeled mathematically. This flow can quickly achieve conditions in which the steady-state current is controlled by the solution flow rather than diffusion.

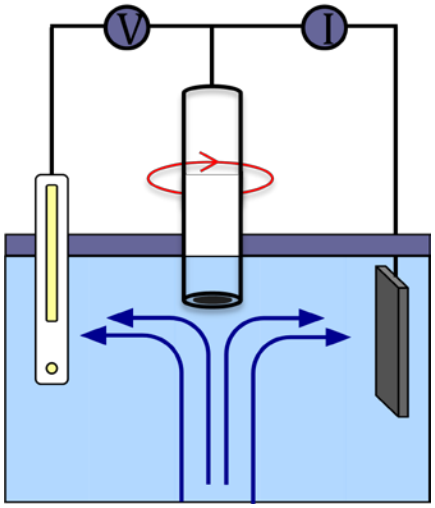


Figure 5.13. Schematic of rotating disk electrode study

Linear potential voltammograms were plotted from 00 to -500 mV at both low and high convection agitation (Figures 5.14. and 5.15.). The measurements were made in the plating solution of 50 mM Bi + 30 mM Sb in dimethylsulfoxide (DMSO) at room temperature. Non – faradic surface charging of the double layer takes place at lower potentials and transitions to faradaic reduction of bismuth antimony species at higher potentials. The higher agitation reduces the Nernst diffusion layer at the electrode surface, yet very little current is increased by increasing the electrode RPMs. Furthermore, at the highest electrode RPMs, the main difference in the current density is the change from double layer charging to activation controlled current. Note that at the highest RPM's the electrical double layer in the area above the working electrode is greatly disturbed. Overall, the rotating disk electrode study showed that the deposition of bismuth antimony is not limited by mass transport difficulties. The ability to maintain the correct bismuth antimony concentrations should not be a problem in nanowire growth.

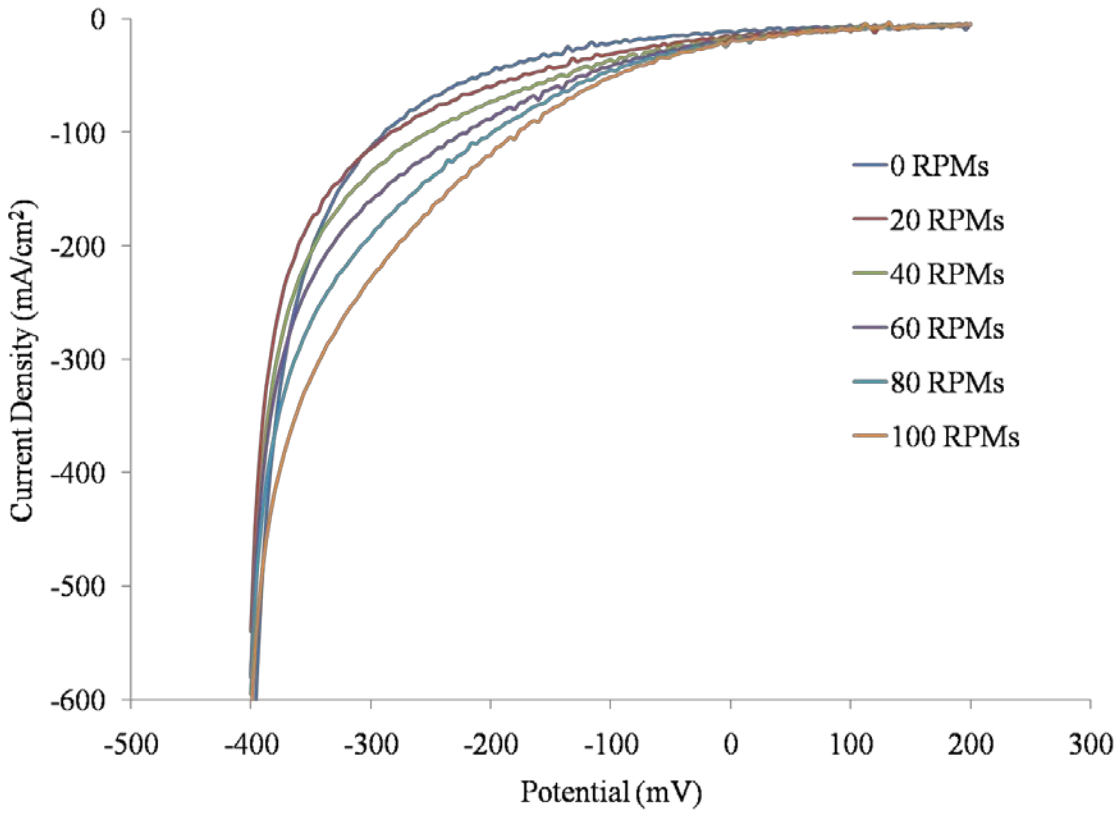


Figure 5.14. Linear voltammograms with RDE at low agitation

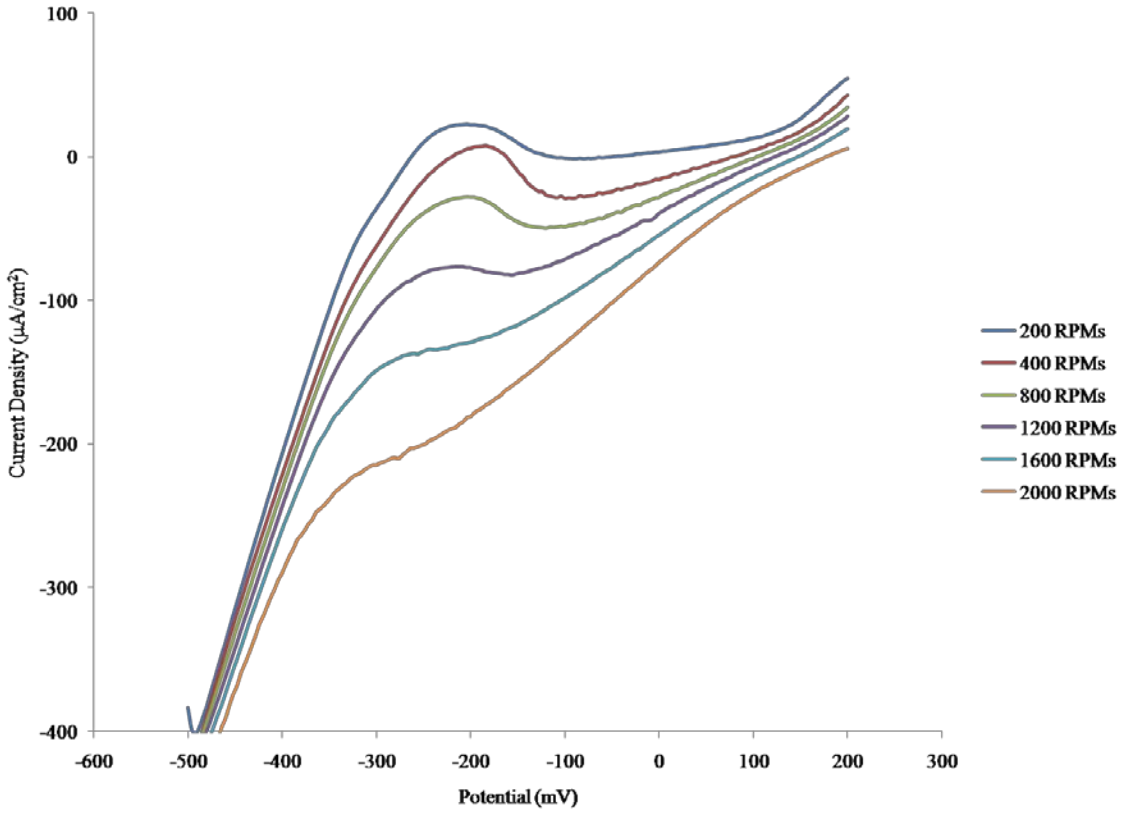


Figure 5.15. Linear voltammograms with RDE at high agitation

Cyclic voltammetry was used to help characterize where current is a function of potential in the electrodeposition setup. Figure 5.16 show overlays of three independent cyclic voltammograms. These graphs show the electroactive ions of 30 mM $Sb^{3+}$, 50 mM $Bi^{3+}$, and both $Sb^{3+}$ + $Bi^{3+}$ in DMSO at room temperature. From the CV, it is evident that bismuth has a very large reduction potential (3 mA/cm$^2$ at -500 mV) when compared to the reduction potential of antimony (-0.5 mA/cm$^2$ at -500 mV). When both $Bi^{3+}$ and $Sb^{3+}$ ions are reduced, $Bi^{3+}$ ions dominate the kinetic reaction, depositing at a greater rate than the sluggish $Sb^{3+}$ ion. In other words, as the potential increases from the open circuit potential, the total cathodic current increases linearly for both bismuth and

antimony with bismuth depositing at a greater rate than antimony. This phenomenon is actually favorable for nanowire growth. $Bi_{(1-x)}Sb_{(x)}$ nanowires need to possess an Sb content of about 15 percent in order to achieve the highest thermoelectric figure of merit, $ZT$ = 1.2. Since the ionic solution controls the final composition of the nanowires, achieving the proper Bi:Sb ratio was not found to be an issue.

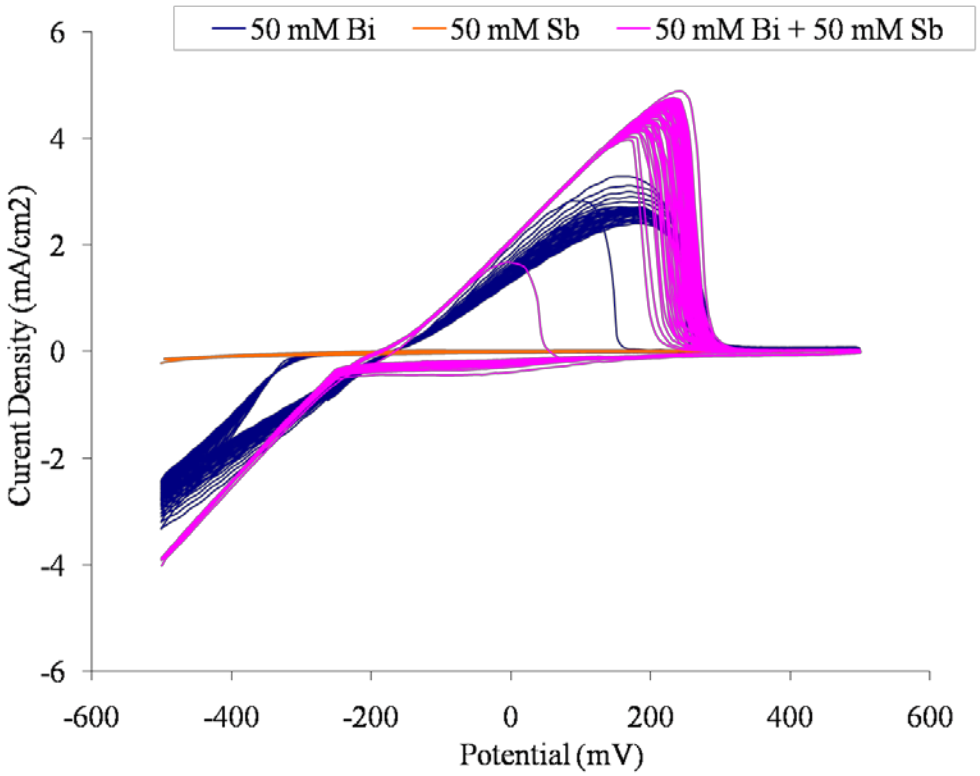


Figure 5.16. Cyclic voltammogram overlays of bismuth and antimony in DMSO

Electrochemical impedance spectroscopy (EIS) was used to determine the ideal pulse parameters for nanowire growth. This technique was utilized to help explore the electron transfer rate from the electrode (AAO template on Si substrate) to the ion ($Bi^{3+}$ or $Sb^{3+}$). EIS was taken with DC signals starting at OCP, then ramping the potential, in –100 mV steps, for each spectrum. Before each scan, the electrochemical system was

polarized at the new potential, and the cell was allowed to stabilize for 120 seconds. Coupled to the each DC potential was a small AC sine wave perturbation with amplitude of ± 5 mV. The range of the AC frequency scans was initiated at 100 KHz and finalized at 100 mHz with 10 frequency per decade. The most prominent features in this graph are the decreasing semi-circles. This is a sign of the decreasing double-layer capacitance and decreasing faradaic resistance as the polarizing potentials are driven more reducing. These semicircles are characteristic of kinetic control by an electrochemical charge transfer step at the electrode-electrolyte interface. The Nyquist plot (Figure 5.17.) was used to determine the electrodeposition pulse parameters for nanowire growth. In this case, the charge transfer resistance is the resistance to transfer electrons from the ionic species to the electrode and back again. Activation current is the minimum current needed to get the reaction to start and for plating to begin. In order to start nanowire growth, the minimum activation current and minimum time constant must be overcome. The double layer capacitance is formed in front of the working electrode surface. The surface must charge up high enough in order for electrons to pass through the electrical double layer and to the surface for electron transfer to take place. A large electrical double layer requires a lot of charge, so the pulse needs to be slower to account for this. A short pulse on a large double layer with just charge and discharge the capacitor and no electrons will be able to get to the plating surface.

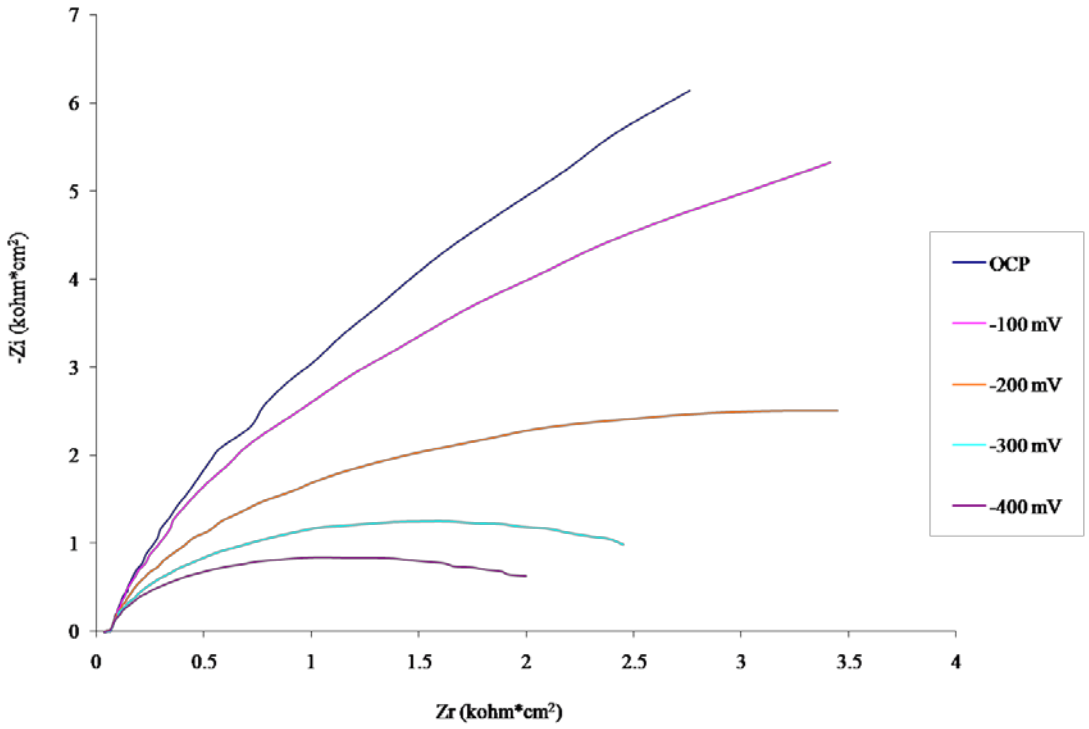


Figure 5.17. Nyquist plot for 50 mM $Bi^{3+}$ and 50 mM $Sb^{3+}$ in DMSO

The above Nyquist plot was used to determine the diffusion coefficient of $Bi^{3+}$ $Sb^{3+}$ using the following equation:

$$\sigma = \left[\frac{RT}{(nF)^2}\right]\left[\frac{1}{2^{1/2}}\right]\left[\frac{1}{C_{ox}^{\circ} D_{ox}^{1/2}} + \frac{1}{C_{red}^{\circ} D_{red}^{\circ}}\right] \qquad (25)$$

assume to be equal

$$\text{so that, } \sigma = \left[\frac{RT}{(nF)^2}\right]\left[\frac{2^{1/2}}{D^{1/2} C^{\circ}}\right] \qquad (26)$$

The diffusion coefficient was determined to be $2.4 \times 10^7$ cm/s$^2$. The time constant was also extrapolated to be 159 ms and the activation current was 419.2 µA. To

summarize, a pulse of at least 419.2 μA for the duration of 159 ms was needed in order to begin the nanowire deposition process.

A schematic of the electrochemical cell used for $Bi_{(1-x)}Sb_{(x)}$ nanowire growth is shown in Figure 5.18. The nanowires were deposited via chronopotentiometry. Chronopotentiometry is a controlled current electrochemical method in which a current flows between two electrodes and the potential of the working electrode is monitored as a function of time with respect to the reference electrode. The nanowire application pulse was at -1.5 mA for 250 ms. A small etching pulse of 0.25 mA for 2 s. was also used as shown in Figure 5.20.

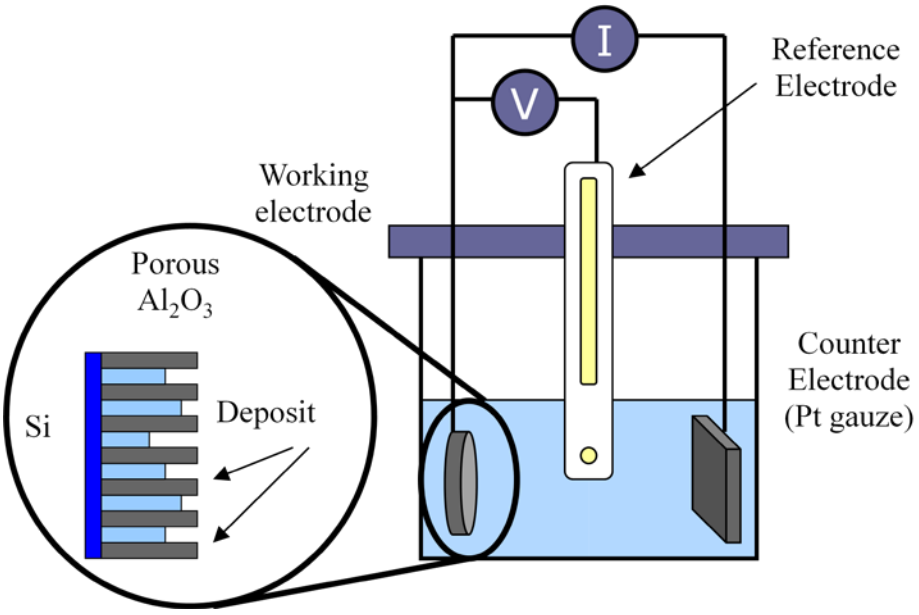


Figure 5.18. Schematic of nanowire electrodeposition setup

Chronopotentiometry was utilized to pulse the deposition potential in order to avoid a large Nernst diffusion layer and create more crystalline nanowires. The short on-pulse helped emulate nanoscale features during the growth process. It was found that by

including a small etch pulse a better array of nanowires were produced. The reason for this was two-fold. First, the 2 sec etch allowed the concentration of ions at the interface to return to the concentration of the bulk solution. This step helped maintain the correct Sb concentration in the nanowires. The 0.25 mA on-pulse also aided in the etch of any nanowires that have grown up and out of the porous channels. This additional step kept the surface smooth and the current uniformly distributed in the pores during deposition. Higher deposition pulses create blossoming of $Bi_{(1-x)}Sb_{(x)}$ over the AAO surface. Once a nanowire reaches the surface of the template the current does not experience any more resistance at that particular pore and increases, while robbing current from the other pores that have not yet completely filled with material. Figure 5.20. shows $Bi_{(1-x)}Sb_{(x)}$ nanowires grown in an AAO for 3000 cycles.

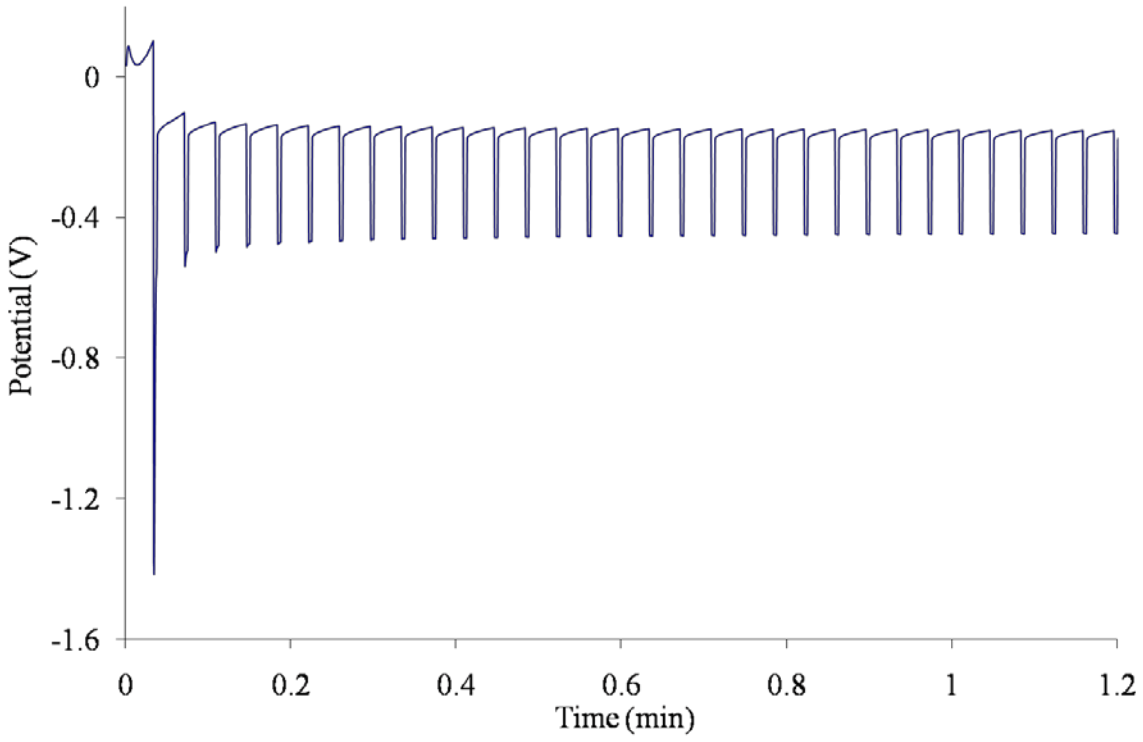


Figure 5.19. Chronopotentiometric pulse for $Bi_{(1-x)}Sb_{(x)}$ nanowires in AAO template in 50 mM $Bi^{3+}$ and 50 mM $Sb^{3+}$ in DMSO at room temp.

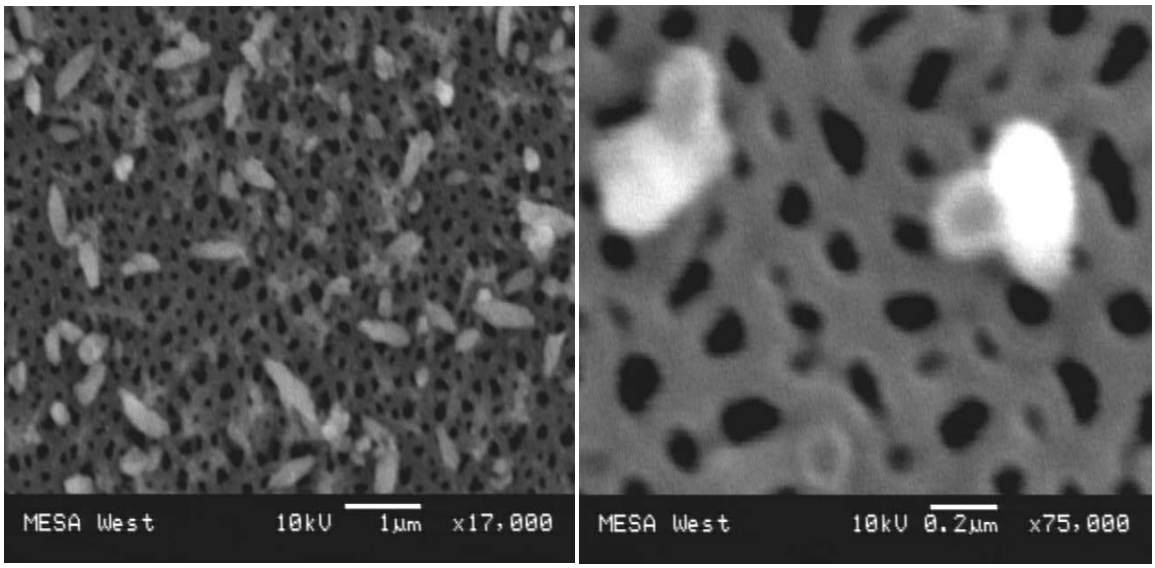


Figure 5.20. Top-view SEM of $Bi_{(1-x)}Sb_{(x)}$ nanowires grown out of AAO template at low resolution and same sample at high resolution

### 5.4.3. Thermoelectric Measurements

In order to complete the thermoelectric couple, a hybrid nanowire-bulk couple was assembled to measure the properties, as shown in Figure 5.21. Nanowire lengths determine the magnitude of the thermal gradient. The Sb-rich nanowire array described above for *ZT* measurement produced $\Delta T = 7$ K for only 50 μm long samples. This gradient should be greater using optimized nanowires by increasing *ZT* and length, perhaps leading to $\Delta T \geq 100$ K. Since the concept is still new, such performance has never been measured. Finally, while typical thermoelectric cooling devices have a $\Delta T \sim 45\ ^{\circ}C$, those measurements are performed at ~ 130 K with bulk legs of the correct compositions. At room temperature, the *ZT* of 0.18 is within the modeled range and would likely increase under completely optimized conditions.

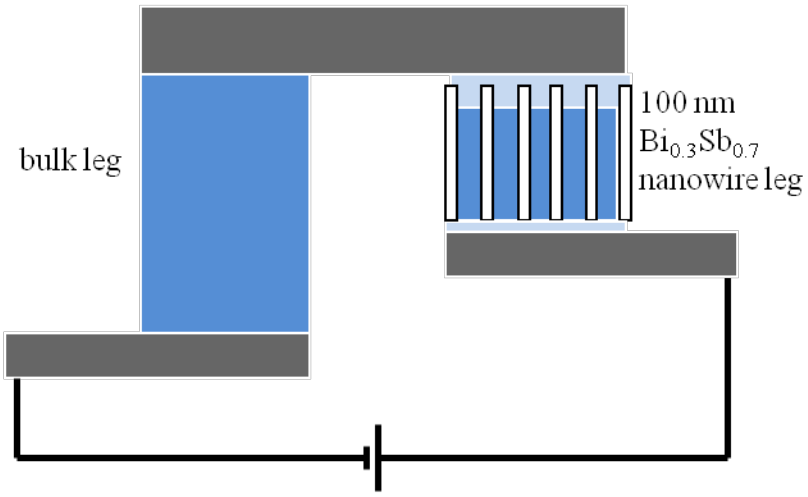


Figure 5.21. Schematic of bulk – nanowire thermoelectric device

## 5.5. Summary

Anodized alumina templates were grown directly on silicon substrates. These templates possessed high – density pores which allowed for the nucleation of $Bi_{(1-x)}Sb_x$ nanowires. To conclude, fundamental electrochemical studies were carried out on $Bi^{3+}$, $Sb^{3+}$, and both cations in order to determine any mass transport issues that may arise during nanowire plating. EIS was used to determine the ideal electrodeposition parameters and the $Bi_{(1-x)}Sb_{(x)}$ were successfully fabricated in an anodic aluminum oxide (AAO) template. Bismuth antimony nanowires were deposited using the chronopotentiometry method, where a short etching pulse was used to help maintain nanoscale features of the wires while etching away any overgrowth through the template. The nanowires demonstrated experimental thermoelectric cooling capabilities when fabricated as the p-type leg of a thermoelectric device.

# CHAPTER 6: CONCLUSIONS

A systematic electrochemical – based study has been carried out on one – dimensional nanostructures. Nano – carbon and bismuth antimony were chosen to represent two examples of the versatility of electrochemical analysis of functional materials at the nanoscale. Nano – carbon was chosen as an electrode material for biosensing applications while bismuth antimony nanowires were chosen for the fabrication of a thermoelectric device.

A modified carbon nanotube electrode was prepared for detection of DNA from *Salmonella enterica* serovar Typhimurium using impedimetric sensing techniques. The SWNTs – COOH deposited on the glassy carbon provided a rich, active, high surface area matrix for the binding of the aminated ssDNA probe. Target DNA sensing was accomplished by measuring the change in the overall impedance of the system as well as measuring the charge transfer resistance. Due to both ssDNA probes and complimentary DNA binding directly onto the electrode surface, the change in charge transfer resistance was a reliable, sensitive activity used to monitor the performance of the biosensor. The specificity of the functionalized electrode was also investigated by introducing it to both unmatched and one-base mismatched sequences. Overall, the impedimetric detection method using a modified carbon nanotube electrode provides a quick, facile label-free biosensor which exhibits high sensitivity and selectivity. This electrode was found to be able to detect DNA at $10^{-10}$ M concentrations.

Boron – doped nanocrystalline diamond films were also evaluated for their sensitivity to *Salmonella* DNA hybridization. They were functionalized in a similar way to SWNTs. First, the BDD was exposed to hydrogen plasma in order to create a surface for carboxyl groups to attach. Once the $NH_2$-ssDNA attached to the –COOH groups, the electrode was prepared for complementary DNA hybridization. It was found that the modified BDD could detect DNA at $10^{-6}$ M concentrations. This value is not as sensitive as the CNT – based electrode because it is believed that the CNTs provide a larger surface area for the ssDNA to attach. Nonetheless, the BDD still proved to be a reliable DNA sensor. In order to qualitatively observe the complementary strand hybridization on the BDD electrode, fluorescent microscopy was employed. The resulting images show that the DNA does not uniformly bond onto cracks or abnormalities in the film, which may be another reason for the less sensitive detection limit of the electrode.

Both boron – doped and nitrogen – incorporated nanocrystalline diamond films were examined for suitability as enzymatic biosensors. Lactic acid was chosen as an appropriate analyte due to its function in many physiobiological processes. The enzyme lactate oxidase was immobilized onto the functionalized diamond surfaces and amperometric detection was carried out in a phosphate buffer solution. While nitrogen – incorporated electrodes did not display a good response, the boron – doped electrodes performed very uniformly for lactic acid concentrations of 5 mM to 20 mM. This range is appropriate for lactic acid detection in human blood.

Details of the fabrication of anodized aluminum oxide templates and nanowire growth in these templates were demonstrated. Aluminum films on silicon substrates

were successfully anodized and fully characterized using the non – destructive method of electrochemical impedance spectroscopy. Equivalent circuit modeling of the EIS data provided useful information about the thickness of the barrier oxide layer of the AAO templates. This information is vital in applying the correct acid concentrations for removal of the barrier layer and could not be obtained without compromising the sample by other microscopy methods. Fundamental electrochemistry experiments on $Bi^{3+}$, $Sb^{3+}$, and both cations in dimethyl sulfoxide were carried out to characterize the ideal chronopotential pulse and to determine the thermodynamic, diffusion and mass transport issues when plating $Bi_{(1-x)}Sb_{(x)}$ into nano dimension pore structures. Such chronopotentiometry resulted in uniform nanowire growth within porous channels of the AAO template. Finally, the thermoelectric efficiency was measured on the wires to be 0.18, which agrees with the theoretical computational results found in literature.

## REFERENCES


1. R. F. Davis, *Diamond films and coatings: development, properties, and applications*. (Noyes Pub., Park Ridge, N.J., 1993).

2. S. Iijima, Nature 354, 56-58 (1991).

3. E. W. Wong, P. E. Sheehan and C. M. Lieber, Science 277 (5334), 1971-1975 (1997).

4. J. Hone, M. Whitney, C. Piskoti and A. Zettl, Physical Review B 59 (4), 2514-2516 (1999).

5. A. Thess, R. Lee, P. Nikolaev, H. Dai, P. Petit, J. Robert, C. Xu, Y. H. Lee, S. G. Kim, A. G. Rinzler, D. T. Colbert, G. E. Scuseria, D. Tomanek, J. E. Fischer and R. E. Smalley, Science 273 (5274), 483-487 (1996).

6. L. S. Pan and D. R. Kania, in *Diamond: Electronic Properties and Applications The Kluwer international series in engineering and computer science* (Kluwer Academic, Boston, 1995).

7. R. Saito, M. Fujita, G. Dresselhaus and M. S. Dresselhaus, Applied Physics Letters 60 (18), 2204-2206 (1992).

8. R. D. Beck, P. S. John, M. M. Alvarez, F. Diederich and R. L. Whetten, J. Phys. Chem. 95, 8402-8409 (1991).

9. M. M. J. Treacy, T. W. Ebbesen and J. M. Gibson, Nature 381 (6584), 678-680 (1996).

10. S. B. Sinnott, Journal of Nanoscience and Nanotechnology 2, 113-123 (2002).

11. X. Yu, D. Chattopadhyay, I. Galeska, F. Papadimitrakopoulos and J. F. Rusling, Electrochemistry Communications 5 (5), 408-411 (2003).

12. J. Liu, A. G. Rinzler, H. Dai, J. H. Hafner, R. K. Bradley, P. J. Boul, A. Lu, T. Iverson, K. Shelimov, C. B. Huffman, F. Rodriguez-Macias, Y.-S. Shon, T. R. Lee, D. T. Colbert and R. E. Smalley, Science 280 (5367), 1253-1256 (1998).

13. J. J. Gooding, R. Wibowo, Liu, W. Yang, D. Losic, S. Orbons, F. J. Mearns, J. G. Shapter and D. B. Hibbert, Journal of the American Chemical Society 125 (30), 9006-9007 (2003).

14. J. Weber, A. Kumar and S. Bhansali, Sensors and Actuators B: Chemical 117 (1), 308-313 (2006).

15. R. N. Hegde, R. R. Hosamani and S. T. Nandibewoor, Colloids and Surfaces B: Biointerfaces 72 (2), 259-265 (2009).

16. C. Lynam, N. Gilmartin, A. I. Minett, R. O'Kennedy and G. Wallace, Carbon 47 (10), 2337-2343 (2009).

17. C. Batchelor-McAuley, G. G. Wildgoose and R. G. Compton, Biosensors and Bioelectronics 24 (11), 3183-3190 (2009).

18. G. Pastor-Moreno and D. J. Riley, Electrochimica Acta 47 (16), 2589-2595 (2002).

19. G.M. Swain, A.B. Anderson and J. C. Angus, MRS Bulletin 23 (9), 56-60 (1998).

20. X. Sun, Z. Zhang and M. S. Dresselhaus, Applied Physics Letters 74 (26), 4005-4007 (1999).

21. Y.-M. Lin, X. Sun and M. S. Dresselhaus, Physical Review B 62 (7), 4610 (2000).

22. D. M. Rowe, *CRC Handbook of Thermoelectrics*. (CRC Press, New York, 1995).

23. A. L. Jain, Physical Review 114 (6), 1518 (1959).

24. O. Rabina, Y.-M. Lin and M. S. Dresselhaus, Appl. Phys. Lett. 79 (1), 81-83 (2001).

25. J. P. O'Sullivan and G. C. Wood, Proc. R. Soc. London A 317, 511-543 (1970).

26. O. Jessensky, F. Muller and U. Gosele, Applied Physics Letters 72 (10), 1173-1175 (1998).

27. H. Masuda, H. Yamada, M. Satoh, H. Asoh, M. Nakao and T. Tamamura, Applied Physics Letters 71 (19), 2770-2772 (1997).

28. H. Masuda and K. Fukuda, Science 268, 1466-1468 (1995).

29. F. Li, L. Zhang and R. M. Metzger, Chem. Mater. 10 (9), 2470-2480 (1998).

30. A. D. Berry, R. J. Tonucci and M. Fatemi, Applied Physics Letters 69 (19), 2846-2848 (1996).

31. W. J. Yeh, B. Cheng and B. L. Justus, Physica C: Superconductivity 388-389, 433-434 (2003).

32. R. J. Tonucci, D. H. Pearson, D. S. Katzer, A. Rosenberg and H. B. Dietrich, Superlattices and Microstructures 20 (4), 627-632 (1996).

33. A. Ursache, J. T. Goldbach, T. P. Russell and M. T. Tuominen, presented at the 49th Annual Conference on Magnetism and Magnetic Materials, Jacksonville, Florida (USA), 2005 (unpublished).

34. T. Thurn-Albrecht, J. Schotter, G. A. Kastle, N. Emley, T. Shibauchi, L. Krusin-Elbaum, K. Guarini, C. T. Black, M. T. Tuominen and T. P. Russell, Science 290 (5499), 2126-2129 (2000).

35. T. W. Cornelius, J. Brötz, N. Chtanko, D. Dobrev, G. Miehe, R. Neumann and M. E. T. Molares, Nanotechnology 16, S246-S249 (2005).

36. Z. a. Hu, T. Xu, R. j. Liu and H. l. Li, Materials Science and Engineering A 371, 236-240 (2004).

37. C. Liu, J. A. Zapien, Y. Yao, X. Meng, C. S. Lee, S. Fan, Y. Lifshitz and S. T. Lee, Advanced Materials 15 (10), 838-841 (2003).

38. D. Zhou, E. V. Anoshkina, L. Chow and G. Chai, Carbon 44 (5), 1013-1016 (2006).

39. N. Li, X. Li, X. Yin, W. Wang and S. Qiu, Solid State Communications 132 (12), 841-844 (2004)

.

40. M. V. Rastei, R. Meckenstock, J. P. Bucher, E. Devaux and T. Ebbesen, Applied Physics Letters 85 (11), 2050-2052 (2004).

41. M. A. Ghanem, P. N. Bartlett, P. de Groot and A. Zhukov, Electrochemistry Communications 6 (5), 447-453 (2004).

42. Y. Luo, Z. Hou, D. Jin, J. Gao and X. Zheng, Materials Letters 60, 393-395 (2006).

43. X. Xu, L. Chen, C. Wang, Q. Yao and C. Feng, Journal of Solid State Chemistry 178 (6), 2163-2166 (2005).

44. P. D. McGary and B. J. H. Stadler, presented at the 49th Annual Conference on Magnetism and Magnetic Materials, Jacksonville, Florida (USA), 2005 (unpublished).

45. M. Tian, J. Wang, J. Snyder, J. Kurtz, Y. Liu, P. Schiffer, T. E. Mallouk and M. H. W. Chan, Applied Physics Letters 83 (8), 1620-1622 (2003).

46. D. Routkevitch, T. Bigioni, M. Moskovits and J. M. Xu, J. Phys. Chem. 100 (33), 14037-14047 (1996).

47. T. E. Huber, O. Onakoya and M. H. Ervin, Journal of Applied Physics 92 (3), 1337-1343 (2002).

48. E. W. Washburn, Physical Review 17, 273-283 (1921).

49. Y. Zhou, C. Shen and H. Li, Solid State Ionics 146 (1-2), 81-86 (2002).

50. Y. K. Zhou, J. Huang and H. L. Li, Applied Physics A: Materials Science & Processing 76 (1), 53-57 (2003).

51. Z. Yang, Y. Huang, B. Dong and H.-L. Li, Journal of Solid State Chemistry 178 (4), 1157-1164 (2005).

52. Y. Lin, G. S. Wu, X. Y. Yuan, T. Xie and L. D. Zhang, Journal of Physics: Condensed Matter 15, 2917-2922 (2003).

53. B. Cheng and E. T. Samulski, Journal of Materials Chemistry 11 (12), 2901-2902 (2001).

54. H. Xu, D.-H. Qin, Z. Yang and H.-L. Li, Materials Chemistry and Physics 80 (2), 524-528 (2003).

55. R. S. Wagner and W. C. Ellis, Applied Physics Letters 4 (5), 89-90 (1964).

56. Y. Wu and P. Yang, J. Am. Chem. Soc. 123 (13), 3165-3166 (2001).

57. M. S. Gudiksen and C. M. Lieber, J. Am. Chem. Soc. 122 (36), 8801-8802 (2000).

58. M. Wei, D. Zhi and J. L. MacManus-Driscoll, Nanotechnology 16 (8), 1364-1368 (2005).

59. D. Calestani, M. Zha, G. Salviati, L. Lazzarini, L. Zanotti, E. Comini and G. Sberveglieri, Journal of Crystal Growth 275 (1-2), e2083-e2087 (2005).

60. Y. Q. Chen, J. Jiang, B. Wang and J. G. Hou, Journal of Physics D: Applied Physics 37 (23), 3319-3322 (2004).

61. Y. Yin, G. Zhang and Y. Xia, Advanced Functional Materials 12 (4), 293-298 (2002).

62. H. Shin, D. B. Thomson, R. Schlesser, R. F. Davis and Z. Sitar, Journal of Crystal Growth 241 (4), 404-415 (2002).

63. B. A. Wacaser, K. Deppert, L. S. Karlsson, L. Samuelson and W. Seifert, Journal of Crystal Growth 287 (2), 504-508 (2006).

64. H. D. Park, S. M. Prokes and R. C. Cammarata, Applied Physics Letters 87 (6), 063110-063113 (2005).

65. S. Bhunia, T. Kawamura, Y. Watanabe, S. Fujikawa and K. Tokushima, Applied Physics Letters 83 (16), 3371-3373 (2003).

66. H.-Y. Lu, S.-Y. Chu and C.-C. Chang, Journal of Crystal Growth 280 (1-2), 173-178 (2005).

67. S. K. Chan, Y. Cai, I. K. Sou and N. Wang, Journal of Crystal Growth 278 (1-4), 146-150 (2005).

68. T. Gao and T. Wang, J. Phys. Chem. B 108 (52), 20045-20049 (2004).

69. C. X. Shan, Z. Liu and S. K. Hark, Nanotechnology 16 (12), 3133-3136 (2005).

70. X. L. Fu, L. H. Li and W. H. Tang, Solid State Communications 138 (3), 139-142 (2006).

71. Y. Wu, Y. Cui, L. Huynh, C. J. Barrelet, D. C. Bell and C. M. Lieber, Nano Lett. 4 (3), 433-436 (2004).

72. A. M. Morales and C. M. Lieber, Science 279 (5348), 208-211 (1998).

73. Y.-J. Zeng, Z.-Z. Ye, W.-Z. Xu, L.-P. Zhu and B.-H. Zhao, Applied Surface Science 250 (1-4), 280-283 (2005).

74. W. Xu, Z. Ye, L. Zhu, Y. Zeng, L. Jiang and B. Zhao, Journal of Crystal Growth 277 (1-4), 490-495 (2005).

75. X. C. Wu and Y. R. Tao, Journal of Crystal Growth 242 (3-4), 309-312 (2002).

76. K. Balasubramanian and M. Burghard, Small 1 (2), 180-192 (2005).

77. G. Gautam, F. L. Deepak, A. Govindaraj and C. N. R. Rao, Topics in Catalysis 24 (1), 137-146 (2003).

78. Y.-C. Lin and W.-T. Lin, Nanotechnology 16 (9), 1648-1654 (2005).

79. K.-H. Lee, S.-W. Lee, R. R. Vanfleet and W. Sigmund, Chemical Physics Letters 376 (3-4), 498-503 (2003).

80. T. J. Trentler, K. M. Hickman, S. C. Goel, A. M. Viano, P. C. Gibbons and W. E. Buhro, Science 270 (5243), 1791-1794 (1995).

81. T. J. Trentler, S. C. Goel, K. M. Hickman, A. M. Viano, M. Y. Chiang, A. M. Beatty, P. C. Gibbons and W. E. Buhro, J. Am. Chem. Soc. 119 (9), 2172-2181 (1997).

82. J. D. Holmes, K. P. Johnston, R. C. Doty and B. A. Korgel, Science 287 (5457), 1471-1473 (2000).

83. L. Vayssieres, Advanced Materials 15 (5), 464-466 (2003).

84. Y. Sun, N. George Ndifor-Angwafor, D. Jason Riley and M. N. R. Ashfold, Chemical Physics Letters In Press, Corrected Proof.

85. Y. Gao, Z. Wang, J. Wan, G. Zou and Y. Qian, Journal of Crystal Growth 279 (3-4), 415-419 (2005).

86. G. H. Yue, P. X. Yan, D. Yan, X. Y. Fan, M. X. Wang, D. M. Qu and J. Z. Liu, Applied Physics A: Materials Science & Processing V84 (4), 409-412 (2006).

87. Y. X. Zhang, G. H. Li, Y. X. Jin, Y. Zhang, J. Zhang and L. D. Zhang, Chemical Physics Letters 365 (3-4), 300-304 (2002).

88. J. R. Heath and F. K. LeGoues, Chemical Physics Letters 208 (3-4), 263-268 (1993).

89. W. Qingqing, X. Gang and H. Gaorong, Journal of Solid State Chemistry 178 (9), 2680-2685 (2005).

90. Y. Xie, Y. Qian, W. Wang, S. Zhang and Y. Zhang, Science 272 (5270), 1926-1927 (1996).

91. Y. Xie, Y. Qian, W. Wang and G. Zhou, Chin. J. Chem. Phys. 1, 39 (1997).

92. Y. D. Li, X. F. Duan, Y. T. Qian, L. Yang, M. R. Ji and C. W. Li, J. Am. Chem. Soc. 119 (33), 7869-7870 (1997).

93. Q. Wang, D. Pan, S. Jiang, X. Ji, L. An and B. Jiang, Journal of Crystal Growth 286 (1), 83-90 (2006).

94. X. Peng, L. Manna, W. Yang, J. Wickham, E. Scher, A. Kadavanich and A. P. Alivisatos, Nature 404 (6773), 59-61 (2000).

95. B. Gates, B. Mayers, B. Cattle and Y. Xia, Advanced Functional Materials 12 (3), 219-227 (2002).

96. B. Gates, Y. Yin and Y. Xia, J. Am. Chem. Soc. 122 (50), 12582-12583 (2000).

97. E. Braun, Y. Eichen, U. Sivan and G. Ben-Yoseph, Nature 391 (6669), 775-778 (1998).

98. J. Richter, M. Mertig, W. Pompe, I. Monch and H. K. Schackert, Applied Physics Letters 78 (4), 536-538 (2001).

99. H.-Q. Wu, X.-W. Wei, M.-W. Shao, J.-S. Gu and M.-Z. Qu, Journal of Materials Chemistry 12 (6), 1919-1921 (2002).

100. C. H. Kiang, J. S. Choi, T. T. Tran and A. D. Bacher, J. Phys. Chem. B 103 (35), 7449-7451 (1999).

101. Y. Zhang, J. Liu, R. He, Q. Zhang, X. Zhang and J. Zhu, Chemical Physics Letters 360 (5-6), 579-584 (2002).

102. Y. Zhang, J. Zhu, Q. Zhang, Y. Yan, N. Wang and X. Zhang, Chemical Physics Letters 317 (3-5), 504-509 (2000).

103. W. Han, S. Fan, Q. Li, B. Gu, X. Zhang and D. Yu, Applied Physics Letters 71 (16), 2271-2273 (1997).

104. C. Tang, S. Fan, M. L. d. l. Chapelle, H. Dang and P. Li, Advanced Materials 12 (18), 1346-1348 (2000).

105. H. Dai, E. W. Wong, Y. Z. Lu, S. Fan and C. M. Lieber, Nature 375 (6534), 769-772 (1995).

106. H.-Q. Wu, X.-W. Wei, M.-W. Shao and J.-S. Gu, Journal of Crystal Growth 265 (1-2), 184-189 (2004).

107. G. Xie, Z. Wang, G. Li, Y. Shi, Z. Cui and Z. Zhang, Materials Letters In Press, Uncorrected Proof.

108. C. Mao, D. J. Solis, B. D. Reiss, S. T. Kottmann, R. Y. Sweeney, A. Hayhurst, G. Georgiou, B. Iverson and A. M. Belcher, Science 303 (5655), 213-217 (2004).

109. K. Besteman, J. O. Lee, F. G. M. Wiertz, H. A. Heering and C. Dekker, Nano Lett. 3 (6), 727-730 (2003).

110. Y. Cui and C. M. Lieber, Science 291 (5505), 851-853 (2001).

111. N. Fellmann, R. Fabry and J. Coudert, Am. J. Physiol. Heart Circ Physiol. 257, 395-398 (1989).

112. F. Lisdat and D. Schäfer, Analytical and Bioanalytical Chemistry 391 (5), 1555-1567 (2008).

113. S. Jain, S. A. Bidol, J. L. Austin, E. Berl, F. Elson, M. Lemaile-Williams, M. D. 3rd, M. E. Moll, V. Rea, J. D. Vojdani, P. A. Yu, R. M. Hoekstra, C. R. Braden and M. F. Lynch, Clinical Infectious Disease 48, 1065 (2009).

114. C. Maynard, F. Berthiaume, K. Lemarcharnd, J. Harel, P. Payment, P. Bayardelle, L. Mason and R. Brousseau, Applied and Environmental Microbiology 71, 8548 (2005).

115. L. Tang, C. Tsai, W. W. Gerberich, L. Kruckeberg and D. R. Kania, Biomaterials 16 (6), 483-488 (1995).

116. W. Yang, O. Auciello, J. E. Butler, W. Cai, J. A. Carlisle, J. E. Gerbi, D. M. Gruen, T. Knickerbocker, T. L. Lasseter, J. N. Russell, L. M. Smith and R. J. Hamers, Nat Mater 1 (4), 253-257 (2002).

117. A. Hartl, E. Schmich, J. A. Garrido, J. Hernando, S. C. R. Catharino, S. Walter, P. Feulner, A. Kromka, D. Steinmuller and M. Stutzmann, Nat Mater 3 (10), 736-742 (2004).

118. J. Wang, M. A. Firestone, O. Auciello and J. A. Carlisle, Langmuir 20 (26), 11450-11456 (2004).

119. J. Schwan, S. Ulrich, V. Batori, H. Ehrhardt and S. R. P. Silva, Journal of Applied Physics 80 (1), 440-447 (1996).

120. J. Wang and J. A. Carlisle, Diamond and Related Materials 15 (2-3), 279-284 (2006).

121. R. J. Cava, Science 247 (4943), 656-662 (1990).

122. M. S. Dresselhaus, G. Chen, M. Y. Tang, R. G. Yang, H. Lee, D. Z. Wang, Z. F. Ren, J.-P. Fleurial and P. Gogna, Advanced Materials 19 (8), 1043-1053 (2007).

123. O. Rabin, Y.-M. Lin and M. S. Dresselhaus, Applied Physics Letters 79 (1), 81-83 (2001).

124. M. R. Kalantary, D. R. Gabe and D. H. Ross, Journal of Applied Electrochemistry V22 (3), 268-276 (1992).

## ABOUT THE AUTHOR

Jessica Eileen Weber received her BSME in 2003 and MSME in 2005 from the University of South Florida. In 2005, she began her doctoral research in the synthesis and characterization of functionalized nanomaterials for energy and chemical/biological sensing applications. In particular, she is interested in impedimetric analysis of nanomaterials. In 2006, Jessica obtained a prestigious internship at Sandia National Laboratories in Albuquerque, NM to study the electrochemical growth of $Bi_{(1-x)}Sb_{(x)}$ nanowires for thermoelectric applications. She has been the recipient of two National Science Foundation awards: an IGERT Fellowship (2004 – 2006) and a GK-12 Fellowship (2006 – 2010). Jessica has also published numerous papers in peer reviewed journals. Upon completion of her doctoral degree, Jessica would like to obtain a position as a postdoctoral scholar and eventually become a Professor of mechanical engineering.